Transport Properties of the Gas Diffusion Layer of PEM Fuel Cells

by

Nada Zamel

A thesis
presented to the University of Waterloo
in fulfillment of the
thesis requirement for the degree of
Doctor of Philosophy
in
Mechanical Engineering

Waterloo, Ontario, Canada, 2011

I hereby declare that I am the sole author of this thesis. This is a true copy of the thesis, including any required final revisions, as accepted by my examiners.

I understand that my thesis may be made electronically available to the public.

Abstract

Non-woven carbon paper is a porous material composed of carbon composite and is the preferred material for use as the gas diffusion layer (GDL) of polymer electrolyte membrane (PEM) fuel cells. This material is both chemically and mechanically stable and provides a free path for diffusion of reactants and removal of products and is electrically conductive for transport of electrons. The transport of species in the GDL has a direct effect on the overall reaction rate in the catalyst layer. Numerical simulation of these transport phenomena is dependent on the transport properties associated with each phenomenon. Most of the available correlations in literature for these properties have been formulated for spherical shell porous media, sand and rock, which are not representative of the structure of the GDL. Hence, the objective of this research work is to investigate the transport properties (diffusion coefficient, thermal conductivity, electrical conductivity, intrinsic and relative permeability and the capillary pressure) of the GDL using experimental and numerical techniques.

In this thesis, a three-dimensional reconstruction of the complex, anisotropic structure of the GDL based on stochastic models is used to estimate its transport properties. To establish the validity of the numerical results, an extensive comparison is carried out against published and measured experimental data. It was found that the existing theoretical models result in inaccurate estimation of the transport properties, especially in neglecting the anisotropic nature of the layer. Due to the structure of the carbon paper GDL, it was found that the value of the transport properties in the in-plane direction are much higher than that in the through-plane direction. In the in-plane direction, the fibers are aligned in a more structured manner; hence, the resistance to mass transport is reduced. Based on the numerical results presented in this thesis, correlations of the transport properties are developed.

Further, the structure of the carbon paper GDL is investigated using the method of standard porosimetry. The addition of Teflon was found have little effect on the overall pore volume at a pore radius of less than $3\mu m$. A transition region where the pore volume increased with the increase in pore radius was found to occur for a pore radius in the range $3\mu m \leq r \leq 5.5\mu m$ regardless of the PTFE content. Finally, the reduction of the overall pore volume was found to be proportional to the PTFE content.

The diffusion coefficient is also measured in this thesis using a Loschmidt cell. The effect of temperature and PTFE loading on the overall diffusibility is examined. It was found that the temperature does not have an effect on the overall diffusibility of the GDL. This implies that the structure of the GDL is the main contributor to the resistance to gas diffusion in the GDL. A comparison between the measured diffusibility and that predicted by the existing available models in literature indicate that these models overpredict the diffusion coefficient of the GDL significantly.

Finally, both the in-plane and through-plane thermal conductivity were measured using the method of monotonous heating. This method is a quasi-steady method; hence, it allows the measurement to be carried out for a wide range of temperatures. With this method, the phase transformation due to the presence of PTFE in the samples was investigated. Further, it was found that the through-plane thermal conductivity is much lower than its in-plane

counterpart and has a different dependency on the temperature. Detailed investigation of the dependency of the thermal conductivity on the temperature suggests that the thermal expansion in the through-plane direction is positive while it is negative in the in-plane direction. This is an important finding in that it assists in further understanding of the structure of the carbon paper GDL. Finally, the thermal resistance in the through-plane direction due to fiber stacking was investigated and was shown to be dependent on both the temperature and compression pressure.

Acknowledgements

I would like to express my deepest gratitude to my supervisor, Dr. Xianguo Li, for his invaluable guidance, steady encouragement, inspiration and support throughout my Ph.D. I would also like to thank my committee members, Dr. Nasser Ashgriz, Dr. Mike Collins, Dr. Eric Croiset, Dr. John Medley and Dr. Jun Shen for taking the time to scrutinize my thesis. Their comments are highly appreciated.

Thanks to Dr. Jun Shen and Dr. Nelson Astrath from NRC-IFCI for letting me use their laboratory space for the diffusion coefficient measurements. Also, thanks to Dr. Efim Litovsky and Dr. Jacob Kleiman from ITL for their help with the thermal conductivity measurements. I would also like to show gratitude to Dr. Jürgen Becker and Dr. Andreas Wiegmann from Fraunhofer ITWM for giving me access to the GeoDict code without which I would not have been able to simplify the numerical work of this research.

Financial support by Natural Sciences and Engineering Research Council of Canada (NSERC) through Discovery Grants and a Strategic Project Grant is gratefully acknowledged.

Further, I would like to thank all my group members, especially Dr. Hao Wu, Kui Jiao, Ibrahim Alaefour and Saher Al Shakhshir. Without their help, encouragement and fruitful discussions throughout the course of my Ph.D., I would not have been able to put together this important publication. I would also like to thank Aaron Pereira and Queenie So for my ever changing desktop background.

I am forever grateful for all the professors, technical and administrative staff and all the friendships I have made throughout the years at the University of Waterloo. Thanks to my UWaterloo friends Azad Qazi Zade, Kiumars Jalali, Ryan O'Connor, Bartosz Lomanowski and John Hymmen. I would also like to thank my none UWaterloo friends Ozgur Colpan, Anton Dabeet, Rovita Shivpal, Hala Abu El-Haj and Mark and Sylvie Thomas. I cannot also forget my gym friends, Le Lam, Chris Grassing and Nirala Sonder. I will miss the workouts and the laughs.

Thanks to Miljana Prelić and Christina Stavrou for being the best travel partners. We have been to and seen some amazing parts of the world together and I cannot wait for our future adventures. I enjoyed every moment we have spent together, all the laughter, crying, silliness and craziness. I know for sure our friendship will only grow with time.

Thanks to Taresh Mistry and Jane Liu who have been two of my best friends for the past eleven years. I am forever grateful for your encouragement throughout the course of my studies and for all the great memories we have shared together.

Last but not least, thanks to Ahmad El Sayed. Thanks for all the great memories and the laughter. Words fail to describe how much I appreciate our friendship. I am forever grateful for your words of encouragement during the last days before my defence. Here's to google translate, corner hobena in 1948, turkey hobena, poetry, pottery and so much more.

To my Family

To my parents Hidaya and Mahmoud Zamel - Words cannot describe how much I am grateful for all your support and love. Mom, I can only hope I will become a woman with half of your strength. Dad, I can only hope to become a woman with half of your humility. I am proud to be your daughter and will always strive to be the best representation of you.

To my sisters Rania and Rola - I am truly blessed to have two best friends who will always love me despite all my shortcomings.

To my brothers Waleed and Abdullah and my brother-in-law Yektami Akyol - I am lucky to have three great men as part of my life who love me unconditionally and look out for my best interest.

To my nephews Karam and Arsalan Akyol - Karam, your time with us has been short, but your memory lives on. Arsalan, thanks for bringing real happiness into our family. You are the greatest gift we have received.

Table of Contents

List of Tables

List of Figures

Nomenclature

A_c	cross sectional area
b	rate of heating
$B_{x,r}$	structuring element
C	concentration; Kozeny-Carman constant
c_p	heat capacity
D	diffusion coefficient
d_E	Euclid dimension
Df	area fractal dimension
f	volume fraction
H_c	capillary head
J	current density
k	thermal conductivity
K	intrinsic permeability
l	thickness
Q	diffusibility
P	phase pressure
P_{cb}	characteristic capillary pressure
R	reaction rate; radius of fibers; resistance
s	saturation
t	time
T	temperature
$\vec{u}$	velocity
x	spatial dimension; point x
X	pore space
y	spatial dimension
z	spatial dimension

Greek letters

α	empirical constant; thermal diffusivity
β	anisotropy parameter
$\Delta_{k,c}$	correction factor
ϵ	porosity

ϵ_p	percolation threshold porosity
θ	temperature drop; altitude function
θ_c	contact angle
ϑ	region (either solid or void)
κ	permeability (m^2)
λ	pore distribution
ξ	property
μ	viscosity ($Pa \cdot s$)
ρ	density (kg/m^3); variable
σ	electrical conductivity (S/m); surface tension (N/m)
τ	tortuosity
ϕ	phase potential (V)

Subscripts

bulk	bulk property
c	capillary
eff	effective
g	gas
i	i$^{\text{th}}$ species
k	phase
l	liquid
max	maximum
min	minimum
nw	non-wetting phase
r	relative
s	solid
w	wetting
wp	wetting phase
$v \leftrightarrow l$	vapor to liquid

Superscripts

b	bottom
eq	equivalent
m	fitting parameter
n	Kozney-Carman exponent; fitting parameter
wet	wet GDL

Acronyms

CV	coefficient of variation
GDL	gas diffusion layer
MEA	membrane electrode assembly
PEM	polymer electrolyte membrane
$PTFE$	Polytetrafluoroethylene
$wt.\%$	percentage based on weight

Chapter 1

Introduction

Increasing demand for energy, energy security and the need to minimize the impact on the environment related to energy are the major drivers for the research and development of alternative energy technologies. Due to their high efficiency and minimal to zero emissions, polymer electrolyte membrane (PEM) fuel cells are a promising technology. These cells are electrochemical devices, which convert the chemical energy of oxygen and hydrogen efficiently into electrical energy. Their applications span a wide spectrum from automotive applications, to stationary applications, to small devices, such as laptops and mobile phones. In fact, the use of hydrogen fuel cells in place of the internal combustion engine can result in the decrease of emissions by up to 50% [1, 2] depending on the method of hydrogen extraction. Thus, it is not surprising that much work is dedicated to further develop this technology.

In this chapter, background information on PEM fuel cells, the objectives and the outline of this thesis are put forward.

1.1 Polymer Electrolyte Membrane Fuel Cells - Operation Principles and Performance

The structure of a PEM fuel cell is similar to that of a battery (Figure 1.1). A PEM fuel cell is composed of an anode and a cathode. At the anode side, hydrogen is supplied as the fuel, while oxygen or air is supplied as the oxidant at the cathode. Due to the sensitivity of the platinum catalyst to the presence of impurities, the supplied fuel must be pure hydrogen to avoid the contamination of the anode catalyst layer [3-5].

At the cathode catalyst layer, the oxygen is said to be reduced since the byproduct of the electrochemical reaction is water. There is much debate around the actual mechanisms taking

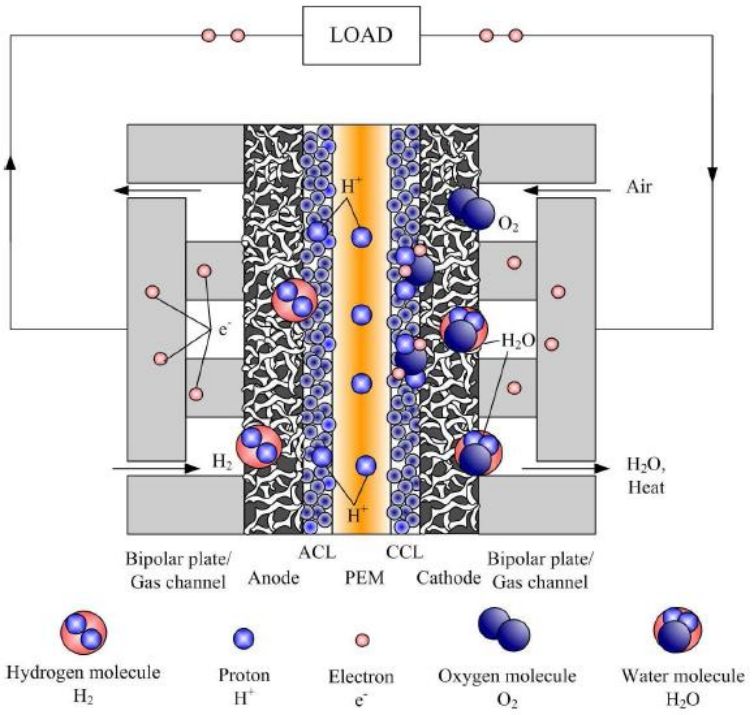

Figure 1.1: Schematic and operation principles of a PEM fuel cell [6]

place in the oxygen reduction reaction (ORR). Many mechanisms have been proposed based on respective theoretical and experimental investigations. Two models have been proposed for the ORR, the associative and dissociative models. In the associative model, the charge transfer to the adsorbed oxygen molecule, with or without simultaneous proton transfer is considered to be the rate determining step as has been suggested by Damjanovic et al. [7-9]:

$$M + O_2 \rightarrow M - O_2 \tag{1.1}$$

$$M - O_2 + H^+ + e^- \rightarrow M - O_2H \tag{1.2}$$

$$M - O_2H + 3H^+ + 3e^- \rightarrow 2H_2O + M \tag{1.3}$$

where M represents a metal such as Pt and Equation (1.2) is the rate determining step.

Norskøv et al. [10, 11] examined the thermodynamic properties of both the associative and dissociative mechanisms. Their results illustrated that both mechanisms are possible and are dependent on the electrode potential. At high electrode potential, the activation energy barrier for oxygen dissociation will increase; thus, the associative mechanism is dominant. Under typical reaction conditions, the O coverage was assumed to be appreciable. The

reaction rate was suggested to be controlled by one of the electron-proton transfer steps. They suggested that the dissociative mechanism follows three steps as given below:

$$\frac{1}{2}O_2 + {}^* \rightarrow O^* \tag{1.4}$$

$$O^* + H^+ + e^- \rightarrow HO^* \tag{1.5}$$

$$HO^* + H^+ + e^- \rightarrow H_2O + {}^* \tag{1.6}$$

where * denotes a site on the catalyst surface.

Although the intermediate reactions are different for the two models, the total reaction is the same. This reaction is the commonly used oxygen reduction reaction in the simulation of the oxygen transport in the electrode of PEM fuel cells and is written as:

$$O_2 + 4H^+ + 4e^- \rightarrow 2H_2O \tag{1.7}$$

At the anode catalyst layer, the hydrogen undergoes an oxidation process where its split into protons and electrons. The hydrogen electro-oxidation reaction occurs on the platinum site in three elementary reaction steps as given below:

$$H_2 + 2Pt \leftrightarrow 2H - Pt \text{ Tafel Reaction [12]} \tag{1.8}$$

$$Pt - H \leftrightarrow H^+ + e^- + Pt \text{ Volmer Reaction [13]} \tag{1.9}$$

$$H_2 + Pt \leftrightarrow H - Pt + e^- + H^+ \text{ Heyrovsky Reaction [14]} \tag{1.10}$$

$$H_2 \leftrightarrow 2H^+ + 2e^- \text{ Hydrogen Oxidation Reaction (HOR)} \tag{1.11}$$

In the Tafel-Volmer pathway, the dissociative adsorption of a hydrogen molecule is followed by two separate one electron oxidations of the H adatoms. In the Heyrovsky-Volmer pathway, a one electron oxidation occurs simultaneously with chemisorption, followed by another one electron oxidation of the H adatom.

The overall reaction of the cell is a combination of the ORR (Equation (1.7)) and HOR (Equation (1.11)) and is given by:

$$\frac{1}{2}O_2 + H_2 \rightarrow H_2O + \text{Heat} + \text{Electrical Energy} \tag{1.12}$$

the byproducts of the overall reaction are water, which is produced at the cathode, heat, which is produced due to joule heating, and electrical energy, which is produced due to the

transport of electrons in the external electric circuit.

The performance of the cell is directly dependent on the overall reaction rate and is usually expressed in terms of the polarization curve, which is the relation between the cell voltage versus its current density as given in Figure 1.2.

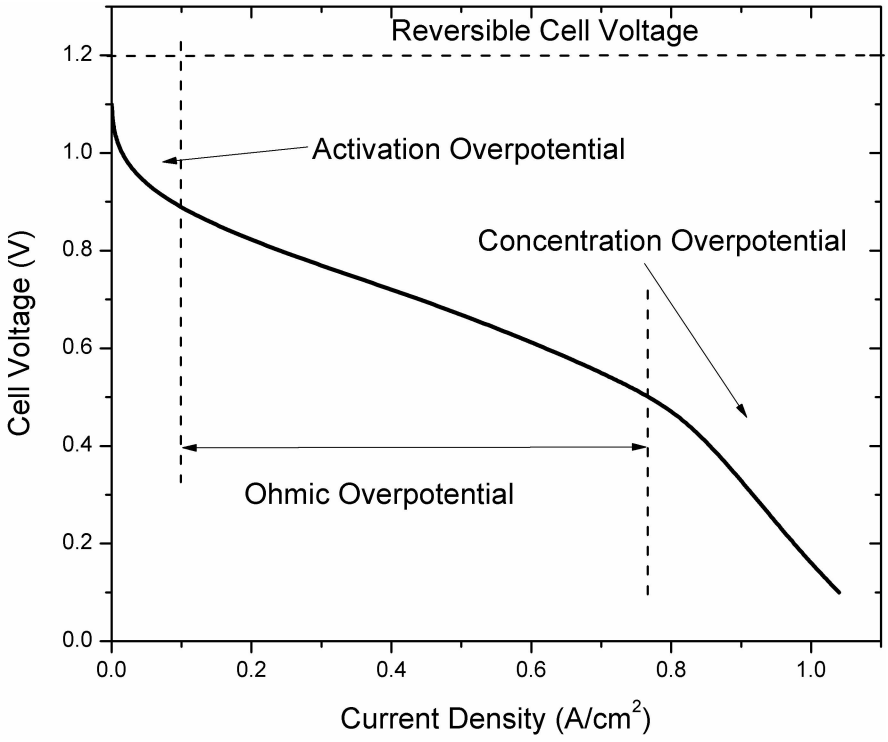

Figure 1.2: A polarization curve showing the three types of overpotential [15].

The performance of a PEM fuel cell is characterized by three different regions; activation polarization region, ohmic polarization region and concentration polarization region. The activation polarization region occurs due to sluggish electro-catalysis at high voltages. At this region, an activation energy is required to drive the reaction. Cell voltage is high, but current density is very low; hence, the power density is low and this region is not very useful for practical fuel cell operations. The second region is associated with ohmic losses across the membrane and the electrodes. The third region is associated with high current densities. At this region, transport limitations are very high and affect the overall performance of the cell. Further, when simulating transport phenomena in the cell, the distribution of species becomes very sensitive to the transport coefficients.

The trend of the polarization curve is very much dependent on the various components of the cell. Each component of the cell must fulfill specific tasks to ensure the cell is running at

its optimal capacity. The bipolar plates provide structural support to the cells and electrical connection between the cells in a stack. They comprise a series of grooves that are used to distribute the reactants and to remove the products. Some bipolar plates also incorporate cooling channels to control the stack temperature. A membrane electrode assembly (MEA) is sandwiched between those bipolar plates. The MEA is composed of two electrodes (cathode and anode) and an electrolyte membrane. The typical material used as the electrolyte membrane of PEM fuel cells is Nafion, which is made of sulfonic acid polymer. The electrolyte membrane acts as an ion conductor, so that ions can migrate from the anode catalyst layer to the cathode catalyst layer, completing the cycle of mass transfer and electric circuit. In order to conduct protons efficiently, the electrolyte membrane must be well hydrated without risking the flooding of the porous electrodes. It is an electron insulator, so that electrons are forced to migrate through the external circuit; thus, providing electric power output. Finally, it must act as a barrier in order to prevent crossover of reactants from the anode to the cathode and vice versa; thus, controlling the electrochemical reaction to proceed as expected. The electrodes compose of two components, the gas diffusion layer and the catalyst layer. The gas diffusion layer provides a flow path for reactant supply and product removal. The gas and liquid species are transported through the void region of the layer, while the electrons travel through the solid region of the layer. The transport of these species directly affects the electrochemical reaction in the catalyst layer. The catalyst layer is made up of electrolyte, solid and void region with the reaction occurring at the interface connecting these phases. The electrolyte is needed for the transport of protons, while the solid is used for transporting electrons and the void region is used by the gaseous reactant.

Since the focus of the research presented in this thesis is on understanding the transport phenomena in the gas diffusion layer, the structure of the gas diffusion layer will be discussed in more detail in the next section.

1.2 Characterization of the Gas Diffusion Layer

The use of a porous material in the design of the gas diffusion layer is essential. The void region is needed to provide a place for the free diffusion of gaseous species and the removal of the reactant products, while the solid is used as an electrical and thermal conductor. The design of the GDL highly affects the performance of the overall cell since it governs much of the transport phenomena beyond the catalyst layer. In order to fulfill the many tasks required of the GDL, two types of GDL materials are commonly used; carbon paper and carbon cloth. These two materials are commercially available and are carbon fiber based

porous materials, which are made hydrophobic by adding PTFE to facilitate liquid water removal. Carbon paper is a non-woven carbon composite, while carbon cloth is woven fabric. There are two major quantifiable structural differences between the two materials; carbon cloth is more porous and less tortuous than carbon paper and liquid water coverage on carbon cloth is less than that on carbon paper [16]. Due to the ease of applying a micro-porous layer to carbon paper, carbon paper is usually used as the GDL of PEM fuel cells. In this thesis research, the study is based on carbon paper material; thus, from now on the term GDL refers to a carbon paper sample.

Carbon paper is best described as a carbon-carbon composite since after heat treatment it consists of carbon fibers (of around 7 (μm) diameter) held together by a carbon matrix [17]. The carbon matrix, which holds the fibers together is usually referred to as a binder and it makes up to 5-15% of the total weight of the final product. The manufacturing process of carbon paper consists of various stages of heat treatment (carbonization and graphitization). While the fibers possess graphite like qualities, the resin-based portion (mostly the binder) of the composite does not graphitize and remains as amorphous carbon [17]. As mentioned earlier, the structure of carbon paper is highly anisotropic since carbonization and graphitization are typically achieved by stacking many sheets in a horizontal or vertical batch furnace.

For the purpose of this thesis research, much of the investigation is based on the carbon paper developed and manufactured by TORAY carbon. This choice has been made based on its availability in various thicknesses (110, 190, 270 and 370 μm) and Teflon treatments (0, 5, 10-60 wt.%). Carbon paper is best described as a carbon-carbon composite since after heat treatment it consists of carbon fibers (of around 7 μm diameter) held together by a carbon matrix [17]. The carbon matrix, which holds the fibers together is usually referred to as a binder and it makes up to 5-15% of the total weight of the final product. The manufacturing process of carbon paper consists of various stages of heat treatment (carbonization and graphitization). While the fibers possess graphite like qualities, the resin-based portion (mostly the binder) of the composite does not graphitize and remains as amorphous carbon [17]. The structure of carbon paper is highly anisotropic since carbonization and graphitization are typically achieved by stacking many sheets in a horizontal or vertical batch furnace. The structure of TORAY carbon paper is analyzed using SEM images as given in Figures 1.3 and 1.4. In order to highlight the anisotropy of the material, scanning electron microscope (SEM) images of the cross section of the carbon paper are examined as shown in Figure 1.3. From this figure, the anisotropy of the material is apparent. Further, the change in the PTFE content in both images is clear. The distribution of the fibers in Figure 1.3 suggests

that Teflon is much more concentrated around the surfaces of the material and it penetrates deeper into the thickness of the material with the increase in its content. In Figure 1.4, the top view of the carbon paper with various PTFE loadings is shown. Comparing Figures 1.4(a) and 1.4(b), it is apparent that the addition of PTFE changes the structure of the binder. In presence of PTFE, the binder is no longer smooth and takes on a shape of a web-like porous material. In order to highlight the effect the PTFE has on the structure of the carbon paper, the distribution of Fluorine is examined as given in Figures 1.4(c) and 1.4(d). As it can be seen, the PTFE coverage of the binder is stronger than that of the actual carbon fibers.

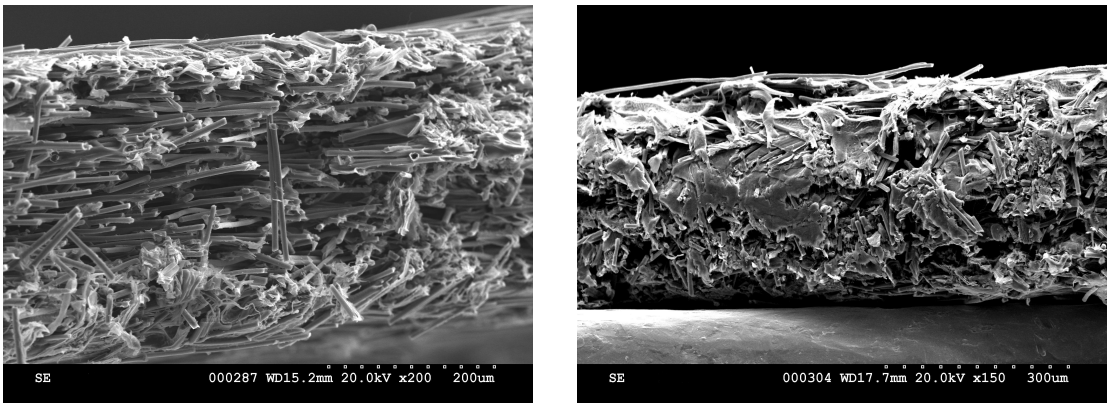

(a) (b)

Figure 1.3: Cross-section view of TORAY carbon paper treated with (a) 20 wt.%; (b) 50 wt.% Teflon

It is also interesting to note the effect of PTFE loading on the deformation of the carbon paper as shown in Figure 1.5. As it can be seen, the deformation of the carbon paper is highly dependent on the amount of Teflon added to the carbon paper sample. After a certain compression pressure, the sample with 50 wt.% PTFE stops deforming and reaches a steady deformation level. This figure suggests that Teflon is not only added to change the hydrophobicity of the carbon paper GDL, it also aids in improving the mechanical durability of the carbon paper.

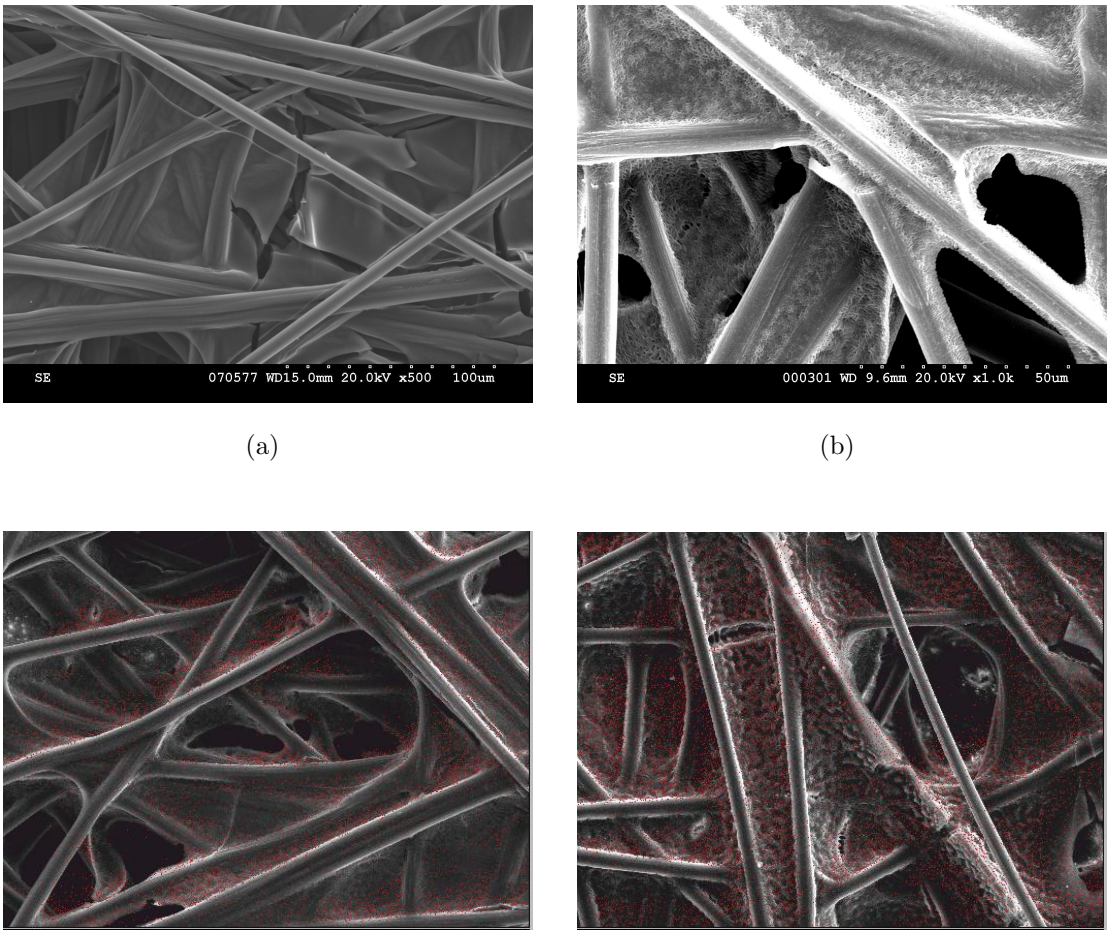

(a) (b)

(c) (d)

Figure 1.4: (a) SEM image of TORAY carbon paper with 0% Teflon treatment; (b) SEM image of TORAY carbon paper with 50 wt.% Teflon treatment; Fluorine distribution on the carbon fibers and binder shown in red dots for TORAY carbon paper treated with (c) 20 wt.% and (d) 50 wt.% Teflon

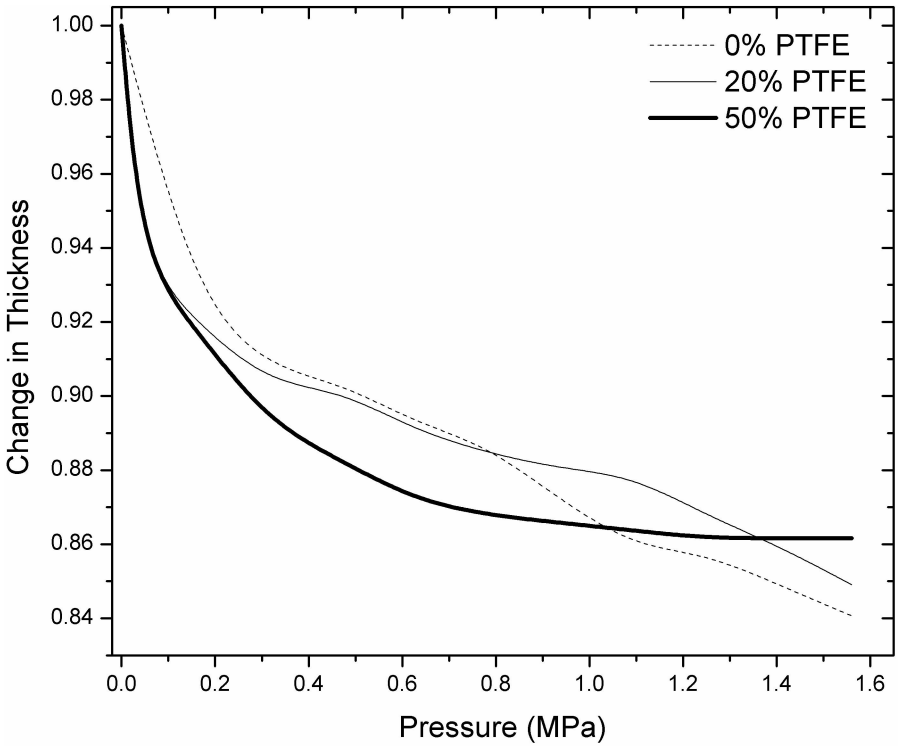

Figure 1.5: Change of thickness of TORAY TPGH-120 carbon paper with compression pressure for samples with PTFE loading of 0, 20 and 50 wt.%

1.3 Thesis Objectives

As it can be seen from the previous section, the structure of the carbon paper GDL can be very complicated. The complexity of its structure will directly influence the transport phenomena, which occur in the GDL. Hence, it is crucial to understand these transport phenomena and their effect on the overall performance of the cell. It is very experimentally expensive to study such phenomena since sensors could affect the transport of species; hence, numerical simulations are often used. However, in order to numerically simulate these phenomena, the transport coefficients of the GDL are needed. The need for such properties is the motivation for this thesis work and thus, the main objective of this thesis is to obtain empirical and theoretical relations for the transport coefficients (gas diffusion coefficient, thermal conductivity, electrical conductivity, intrinsic and relative permeability and capillary pressure) of the carbon paper GDL. This objective is achieved by estimating these transport coefficients experimentally and numerically. This objective becomes clearer in the next chapter, the Literature Review Chapter.

1.4 Scope and Outline of Thesis

In this thesis, the transport properties of the gas diffusion layer of PEM fuel cells are estimated based on experimental and numerical techniques. This thesis is divided into eight chapters. In chapter one, an introduction to the problem at hand, background information on PEM fuel cells and their gas diffusion layer are presented. A detailed literature review is put forward in chapter two. In chapter three, the experimental apparatus are analyzed, while in chapter four, the formulation of the numerical model is given. Based on the experimental results, the structure of the carbon paper is analyzed and the measurements of its effective diffusion coefficient and thermal conductivity are explained in chapter five. The numerical results of the dry and wet GDL are presented in chapters six and seven, respectively, along with the proposed correlations. Finally, chapter eight gives a summary of conclusions as well as recommendations for future work.

Chapter 2

Literature Review

The progress in the research and development of polymer electrolyte membrane (PEM) fuel cells depends heavily on the understanding of the transport phenomena, which occur simultaneously in the cell. Monitoring species transport experimentally can be very difficult as well as expensive and time consuming. Hence, numerical modeling is often used to simulate the transport phenomena. These models can be divided into single phase and multi-phase models. The single phase models are solved under the assumption that water exists in vapor form only, while in the multi-phase models, liquid and vapor water are taken into account.

In order to numerically simulate the transport phenomena, transport coefficients such as the gas diffusion coefficient, electrical conductivity, thermal conductivity, permeability and capillary pressure are usually used. The accuracy of these coefficients governs the overall accuracy of the numerical simulation. In order to gain a better understanding of the literature review put forward in this chapter, the reader should first gain an overview of the numerical simulation of PEM fuel cells. Hence, the first part of this literature review chapter deals with the governing equations of transport phenomena in the gas diffusion layer (GDL) of PEM fuel cells. The rest of the chapter is dedicated to reviewing the available theoretical and experimental expressions of the transport coefficients used in simulating the GDL of PEM fuel cells.

2.1 Numerical Simulation of PEM Fuel Cells

Numerical simulation of transport phenomena in PEM fuel cells can be divided into various categories. These models can be classified based on their time dependency (transient versus steady state), handling of water presence (multi-phase versus single phase), dependency on

temperature (non-isothermal versus isothermal) and based on the components of the cell considered (full cell versus half cell). Transient models are often used over steady state models when investigating transport phenomena that are time dependent such as cold start [18] and poisoning of the cell [3]. The main difference between multi-phase and single phase models is their handling of the state in which water appears in the model. In multi-phase models, the presence of water is taken into consideration in the forms of gas, liquid and dissolved, while in single phase models only the gas phase is considered. The form in which water is considered directly depends on the objectives of the study. Single phase models are usually used to investigate the factors limiting cell performance, while multi-phase models are used to gain a full understanding of the transport mechanisms in the cell. Some of the pioneering single phase models are those by Bernardi and Verbrugge [19, 20] and Springer et al. [21, 22] and two comprehensive multi-phase models are by Baschuk and Li [23] and Wu et al. [24, 25]. Non-isothermal models are used to investigate heat transport in the cell. This is of great interest when dealing with cold start [18] and high temperature PEM fuel cells [26]. Finally, half cell models are often preferred when the study is focused on specific transport phenomena, which are specific to one half of the cell (either the anode or cathode). For instance, carbon monoxide poisoning of the anode catalyst layer is usually investigated by simulating only the anode [3, 27].

2.1.1 Governing Equations

The various transport phenomena in the gas diffusion layer govern the rate of reaction in the catalyst layer (i.e. the overall performance of the cell). Hence, it is necessary to investigate these phenomena. To numerically simulate the transport of gas species, liquid water, heat and electrons, species, mass, momentum, energy and charge should be conserved. In this section, the conservation equations are listed to give an overview of the role that the transport coefficients play in simulating their respective phenomenon.

- **Conservation of Momentum**:
  The conservation of momentum should be applied to both the gas and liquid phases in the GDL. The conservation of the gas phase momentum follows:

$$\frac{\partial}{\partial t}\left(\frac{1}{\epsilon^{\text{eff}}}\rho_g\vec{u}_g\right)+\nabla.\left(\frac{1}{\left(\epsilon^{\text{eff}}\right)^2}\rho_g\vec{u}_g\vec{u}_g\right)=-\nabla P_g+\nabla.\left(\bar{\tau}\right)-\frac{\mu_g}{K\kappa_{rg}}\vec{u}_g \tag{2.1}$$

  where $\epsilon_{\text{eff}}=\epsilon\left(1-s\right)$ is the effective porosity for gas phase transport with ϵ as the

porosity of the GDL and s as the liquid water saturation, ρ_g, $\vec{u}_g$, μ_g and P_g are the density, velocity, viscosity and the pressure of the gas phase, respectively. $\bar{\tau}$ is the stress tensor, and K and κ_{rg} are the intrinsic permeability of the GDL and the relative permeability of the gas phase, respectively. The density of the gas phase is related to the velocity of the gas phase through the continuity equation as given by:

$$\frac{\partial}{\partial t}\left(\epsilon_{\text{eff}}\rho_g\right) + \nabla \cdot \left(\rho_g \vec{u_g}\right) = S_m \tag{2.2}$$

where S_m is the source term and is equal to zero for all gases except for water vapor. Water can change its phase from vapor to liquid and vice versa depending on the thermodynamic properties of the GDL. Hence, for the case of water vapor $S_m = -R_{v\leftrightarrow l}$, which denotes the amount of change in the mass of water vapor.

Due to the small velocity associated with the liquid phase and porous nature of the gas diffusion layer, the conservation of momentum of the liquid phase is governed by the generalized Darcy term. The phase pressure is dependent on the relative permeability of its correspondent phase as follows [28, 29]:

$$0 = -\nabla P_l - \frac{\mu_l}{K\kappa_{rl}}\vec{u}_l \tag{2.3}$$

where P_l, $\vec{u}_l$ and μ_l are the superficial values of the pressure, velocity and viscosity of the liquid phase and κ_{rl} is the relative permeability of the liquid phase.

In Equations (2.1) and (2.3), the relative permeability is a function of the liquid water saturation present in the GDL. Hence, for the purpose of numerically simulating the pressure distribution in the GDL, the relative permeability should be expressed in terms of the liquid water saturation. Further, the intrinsic permeability of the GDL is a function of the porous structure of the layer.

- **Conservation of Gaseous Species**:
  Gaseous species, such as oxygen, nitrogen, hydrogen and carbon monoxide are transported through the void region of the GDL. Diffusive and convective transport should be taken into place and the conservation of gas species follows the governing equation below:

$$\frac{\partial}{\partial t}\left(\epsilon^{\text{eff}}C_i\right) + \nabla \cdot \left(-D_{\text{eff}}\nabla C_i\right) + \nabla . \left(\vec{u}_g C_i\right) = S \tag{2.4}$$

  where D_{eff} is the effective diffusion coefficient and C_i is the concentration of the gaseous species i. The source term for the consumption of the gas species is denoted as S. This

term is equal to zero for all gas species except for water vapor. Water can change phases from the liquid to the vapor phase. Hence, in this case, $S = \frac{-R_{v\leftrightarrow l}}{M_w}$, which denotes the amount of change in water vapor, with M_w as the molecular weight of water.

The effective diffusion coefficient is a function of both the liquid water saturation and the structure of the gas diffusion layer.

- **Conservation of Mass**:
  The conservation of mass equation is applied to simulate the change in liquid water saturation inside the GDL and is given by:

$$\frac{\partial}{\partial t}\left(\epsilon \rho_l s\right) + \nabla \cdot \left(\rho_l \vec{u}_l\right) = R_{v\leftrightarrow l} \tag{2.5}$$

  where $R_{v\leftrightarrow l}$ is the rate of evaporation/condensation.

  The liquid water velocity is related to the pressure of the liquid phase. For the purpose of PEM fuel cell simulation, the pressure of the liquid phase is found from its relation with the capillary pressure. The liquid phase pressure is expressed as follows:

$$P_l = P_c + P_g \tag{2.6}$$

  The gas phase pressure is found once momentum is conserved via Equation (2.3). Hence, an expression of the capillary pressure is needed to obtain the liquid water phase pressure. The capillary pressure is expressed in terms of the structure of the GDL and the liquid water saturation.

- **Conservation of Charge**:
  The transport of electrons follows Ohm's law as given below:

$$\nabla \cdot i_s = \nabla \cdot \left(-\sigma_s^{\text{eff}} \nabla \phi_s\right) = 0 \tag{2.7}$$

  where σ_s^{eff} is the effective electrical conductivity, which is a function of the structure of the electrical conductivity of the solid fibers and the structure of the gas diffusion layer. In the gas diffusion layer, electrons are not produced or consumed; thus, the corresponding source term is equal to zero.

- **Conservation of Energy**:
  In the gas diffusion layer, heat is transferred via conduction and convection, and Joule

heating is responsible for heat generation in the layers as given by:

$$\frac{\partial}{\partial t}\left(\left(\rho c_p\right)^{\text{eff}} T\right) + \nabla \cdot \left(\left(\rho c_p\right)^{\text{eff}} \vec{u}_g T\right) = \nabla \cdot \left(k_{\text{eff}} \nabla T\right) + \frac{J_s^2}{\sigma_s^{\text{eff}}} \tag{2.8}$$

where T is the temperature, k_{eff} is the effective thermal conductivity, J_s is the current density due to electrons transfer and σ_s^{eff} is the electrical conductivity of the carbon paper. In the gas diffusion layer, heat is generated due to joule heating, or in other words, the transfer of electrons through the solid matrix of the GDL, which is defined by the second term of the right hand side of the conservation equation. The thermal conductivity of the layer is normally expressed as an average property of the thermal conductivity of all the species of the layer (gas, solid and liquid water). This average property should be corrected to take into account the distribution of each species in the layer.

Studying the conservation equations listed above, the need for expressions of the transport coefficients is established. In the next sections of this chapter, a survey of the available expressions in literature is given. A detailed literature review of the numerical, theoretical and experimental works dedicated to estimating the effective diffusion coefficient, thermal conductivity, electrical conductivity, intrinsic permeability, relative permeability and capillary pressure is put forward.

2.2 Effective Diffusion Coefficient

Given the broad range of application for porous media, analysis of the effective transport properties is extensive in literature. Theoretical and empirical relations of the effective diffusion coefficient for a wide range of porous materials are found. These relations use the porosity as the sole independent variable and use one or more fitting variables. Much of the early work found in literature is done on soil. Buckingham [30], Penman [31, 32] and van Bavel [33] found empirical relations of the effective diffusion coefficient in soil versus the porosity of the soil sample. Currie [34] also studied the effect of the porosity of the soil sample on the effective diffusion coefficient of a hydrogen-air mixture. He then extended the earlier study to examine the diffusion in other porous materials (glass spheres, kaolin, sand, carborundum, celite, sodium chloride, steel wool, pumice, vermiculite, mica and perspex flakes) [35]. These works were all empirical. Other works are mathematical analyses of the effective diffusion coefficient and some are given by references [36-48]. The analysis on which these mathematical studies are based is similar in that they study porous media that are

composed of spheres. Some of the studies are extended to take into account the presence of liquid water on the effective diffusion coefficient. Others look into the statistical randomness of the distribution of the spheres.

Examining the early works on effective diffusion coefficients in porous materials, a common, general expression for the effective coefficient can be written as:

$$D_{\text{eff}} = D_{\text{bulk}} f(\epsilon)\, g(s) \tag{2.9}$$

where $f(\epsilon)$ is a structural function based on the porosity, ϵ of the medium and $g(s)$ is a function dependent on the liquid water saturation, s, which can be written as:

$$s = \frac{\text{volume of liquid}}{\text{volume of void}} \tag{2.10}$$

Many correlations for the effective diffusion coefficient in the carbon paper gas diffusion layer of PEM fuel cells are available in literature. Currently, the Bruggeman Approximation [36] is the most widely used correlation to obtain the effective diffusion coefficient of gases in the GDL. The relation was derived using effective medium approximations, which are analytical models used to describe macroscopic properties of porous media. These approximations sometimes do not apply to percolating systems; thus, failing to accurately estimate their properties. The Bruggeman approximation was derived for electrical conductivity and the dielectric constant of a medium composed of uniformly distributed spheres. Effective transport relations are sometimes interchangeable; thus, the Bruggeman Approximation in terms of the diffusion coefficients has been commonly written as:

$$\frac{D_{\text{eff}}}{D_{\text{bulk}}} = \epsilon^{m} \tag{2.11}$$

where m is the Bruggeman exponent and its widely used value is 1.5, D_{eff} is the effective diffusion coefficient, D_{bulk} is the bulk diffusion coefficient and ϵ is the porosity.

The Bruggeman Approximation given in Equation (2.11) is usually modified in the presence of liquid water to obtain the effective diffusion coefficient of the wet GDL and it is written as follows:

$$\frac{D_{\text{eff}}^{\text{wet}}}{D_{\text{bulk}}} = \epsilon^{1.5}\,(1-s)^{1.5} \tag{2.12}$$

where s is the liquid water saturation. Equation (2.12) simply states that the effect of gas diffusion through liquid water can be ignored since the diffusion coefficient of gases in liquid water is much smaller than that in the pore space. Hence, presence of liquid water in the

GDL decreases the overall porosity of the GDL; in other words, the pore space available for gas diffusion is decreased.

Other attempts for correlating the effective diffusion coefficient to the bulk diffusion coefficient in porous media are found in the following references [40, 42, 47, 48]. Neale and Nader [40] developed an expression for an isotropic porous medium composed of spherical particles as follows:

$$\frac{D_{\text{eff}}}{D_{\text{bulk}}} = \frac{2\epsilon}{3-\epsilon} \tag{2.13}$$

The expression in Equation (2.13) was developed mathematically for a homogeneous and isotropic agglomeration of impermeable spheres with a porosity, ϵ, and an arbitrary size distribution as shown in Figure 2.1(a). In order to develop the expression, an arbitrary sphere with a radius, R, and its associated pore space having a radius S as shown in Figure 2.1(b) were used. The outer radius of the pore space was chosen in such a way that the porosity of the unit cell (reference sphere and the concentric shell) is identical to that of the original system. In order to satisfy this constraint, Neale and Nader [40] suggested that:

$$\frac{S}{R} = (1-\epsilon)^{-\frac{1}{3}} \tag{2.14}$$

which should hold for the porosity range $0 \leq \epsilon < 1$.

In the study by Das et al. [48], they used a mathematical formulation of the Hashin coated sphere model [49] to obtain the effective diffusion coefficient in the GDL of PEM fuel cells. The expression they found resembles that by Neale and Nader [40], Equation (2.13), and is given as:

$$\frac{D_{\text{eff}}}{D_{\text{bulk}}} = 1 - \frac{3\,(1-\epsilon)}{3-\epsilon} \tag{2.15}$$

It should be pointed out here that the expression given by Equation (2.15) provides an upper bound for the effective diffusion coefficient. This upper bound is formulated for porous media with spherical particles without taking into account certain statistical parameters of the random geometry . Das et al. [48] argued that in order to take the statistical randomness of the geometry as well as the structure of the solid matrix into account a function, $f(\epsilon)$, should be introduced to their expression as follows:

$$\frac{D_{\text{eff}}}{D_{\text{bulk}}} = 1 - f(\epsilon)\,\frac{3\,(1-\epsilon)}{3-\epsilon} \tag{2.16}$$

where $f(\epsilon) \geq 0$ and could vary depending on the geometry of the solid matrix.

Further, it is not surprising that the expressions in Equations (2.13) and (2.15) are the

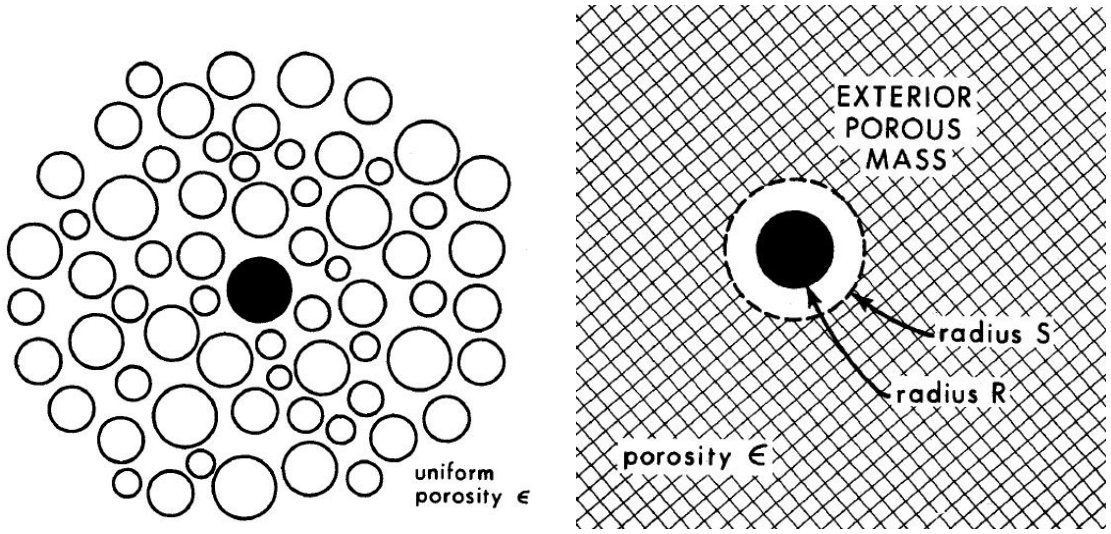

(a) (b)

Figure 2.1: (a) An homogeneous and isotropic swarm of spheres (cross section through center of reference sphere); (b) The proposed model for a homogeneous and isotropic swarm of spheres (cross section through center of reference sphere) [40]

same since they both make the same assumption in regards to the geometry considered as illustrated in Figure 2.2.

Das et al. [48] extended their expression given by Equation (2.16) to take into account the effect of liquid water on the diffusion coefficient of the gas diffusion layer. Their expression is given as:

$$\frac{D_{\text{eff}}^{\text{wet}}}{D_{\text{bulk}}} = 1 + \frac{3\left(1-f_g\right)}{f_g - \dfrac{3D_{\text{bulk}}}{D_{\text{bulk}} - D_l - \dfrac{3\left(1-f_l\right)D_l}{f_l - 3\left(1-f_g\right)}}} \tag{2.17}$$

where D_l is the diffusion coefficient of the gas in liquid water and $f_g = \epsilon\left(1-s\right)$ and $f_l = s\epsilon$ are the volumetric fractions of the gas phase and liquid phase, respectively. Again, due to the small diffusion coefficient of gases in liquid water, the expression in Equation (2.17) shows that the presence of liquid water will only effect the overall pore space available for gas diffusion. In other words, Equation (2.17) can be re-written as:

$$\frac{D_{\text{eff}}}{D_{\text{bulk}}} = 1 + \frac{3\left(1-\epsilon\left(1-s\right)\right)}{\epsilon\left(1-s\right)-3} \tag{2.18}$$

The correlation of the effective diffusion coefficient in porous media obtained by Tomadakis

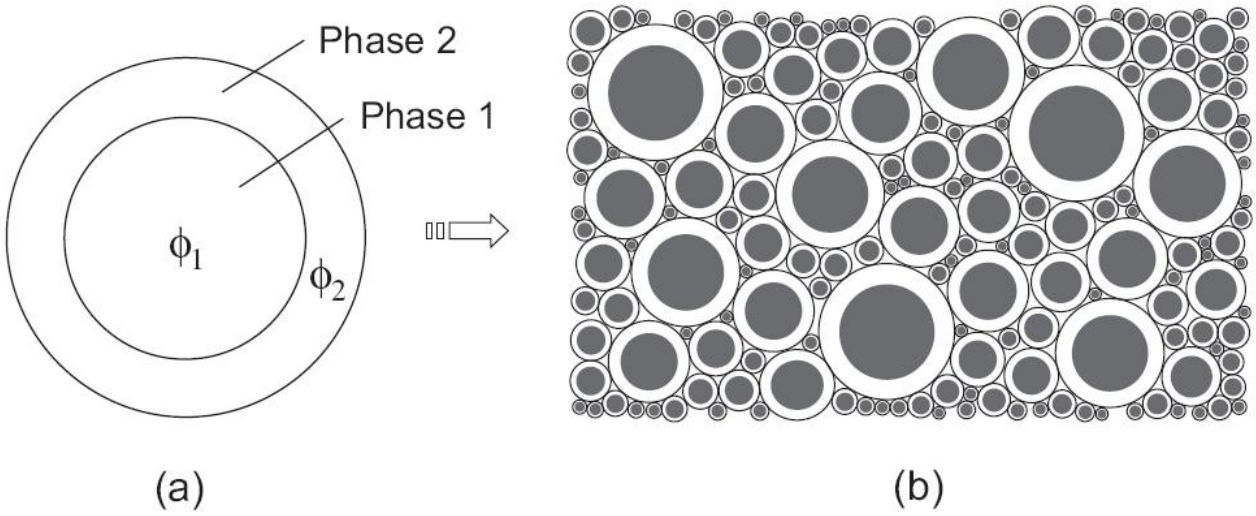

Figure 2.2: Schematic representation of (a) the Hashin coated sphere; (b) cross section of the Hashin coated sphere assemblage. Each coated sphere in part (b) is a scaled version of the coated sphere shown in part (a) [48] - This figure was reconstructed by Das et al. from reference [50]

and Sotirchos [42] was based on the general percolation theory and random distribution of fibers in a porous medium. They used a Monte Carlo scheme to determine the effective diffusion coefficient of randomly placed molecules in the interior of a porous structure. Their scheme was employed to study the effect of the dimensionality of the structure (i.e. d=1, 2, and 3) as well as the Knudsen number. The expression developed for molecular diffusion is as follows:

$$\frac{D_{\text{eff}}}{D_{\text{bulk}}} = \epsilon \left(\frac{\epsilon - \epsilon_p}{1 - \epsilon_p} \right)^{\alpha} \tag{2.19}$$

where ϵ_p is a percolation threshold and α is an empirical constant. A typical value for the percolation threshold is 0.037, and the empirical constant is 0.661 for the three dimensional porous media. The parameter values for one-dimensional and two-dimensional cases for each directionality and diffusion direction were provided in literature [42]. The expression in Equation (2.19) was compared against experimental data for diffusion in sand with various packing and showed very good agreement with experimental data. However, the validity of this expression for estimating the effective diffusion coefficient in the GDL of PEM fuel cells is still questionable because of the significantly different geometries involved. First, it has not been verified against experimental data for diffusion in the GDL. Secondly, the expression for the 3-dimensional porous material assumes that the material is isotropic, which is not true in the case of carbon paper.

The expression by Nam and Kaviany [47] could be considered as an extension to the expression by Tomadakis and Sotirchos [42]. It was also derived from the percolation theory and extended to consider the effect of liquid water condensation on the diffusion process. They assumed that the gas diffusion layer is made up of stacked two-dimensional random carbon fiber mats as shown in Figure 2.3. They assumed that the fibers are infinitely long in the x and y directions, the in-plane direction, and are allowed to overlap. The solid structure is modeled as stacks of continuously overlapping fiber screens.

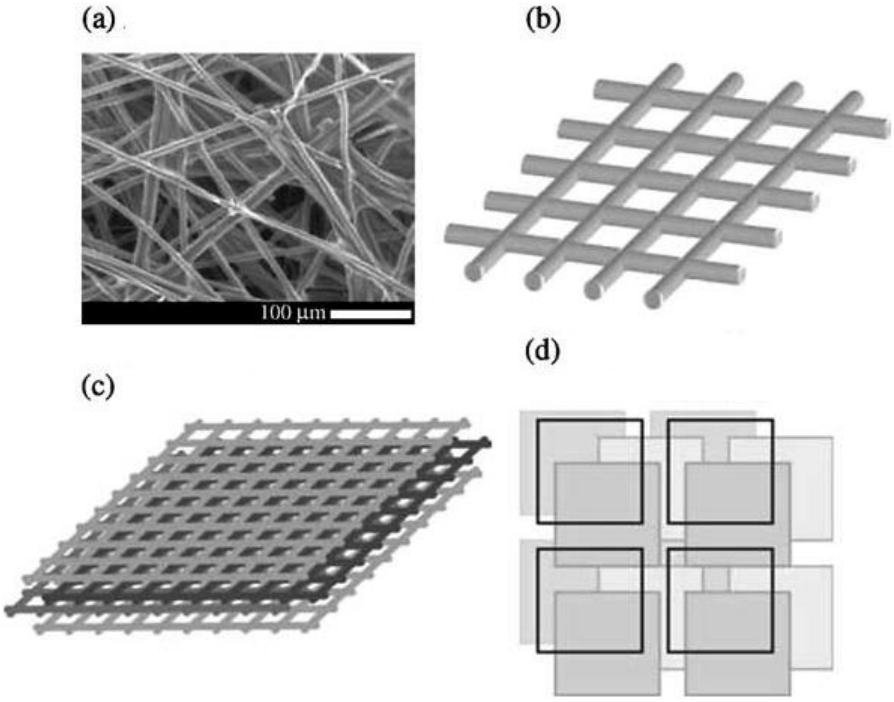

Figure 2.3: Detailed microscale model for fibrous diffusion medium: (a) SEM of random fiber structure (a) Toray carbon paper; (b) a single screen made of overlapping fibers with square pore spaces; (c) stack of fiber screens and; (d) pore spaces of stacks, with an arbitrary screen position shifting [47]

Using the percolation theory to develop a correlation for the effective diffusion coefficient, they found the effective diffusivity as a function of porosity and liquid water saturation to be:

$$\frac{D_{\text{eff}}}{D_{\text{bulk}}} = \epsilon \left(\frac{\epsilon - 0.11}{1 - 0.11} \right)^{0.785} (1 - s)^2 \tag{2.20}$$

Again, the correlation given in Equation (2.20) was not compared to experimental data and simplifications were made in regards to the geometry of the GDL. Similar geometry,

shown in Figure 2.4, was adopted for the GDL in a study by Gostick et al. [51] to understand the behavior of the relative permeability and gas diffusion for different saturation levels. According to the results of their numerical simulation, Gostick et al. [51] argued that many of the available correlations over-predict the effective parameters of the GDL. Their findings also followed a percolation type behavior; however, they did not state a specific correlation for their findings. Their findings are very similar to those calculated by the expression from the study by Nam and Kaviany [47].

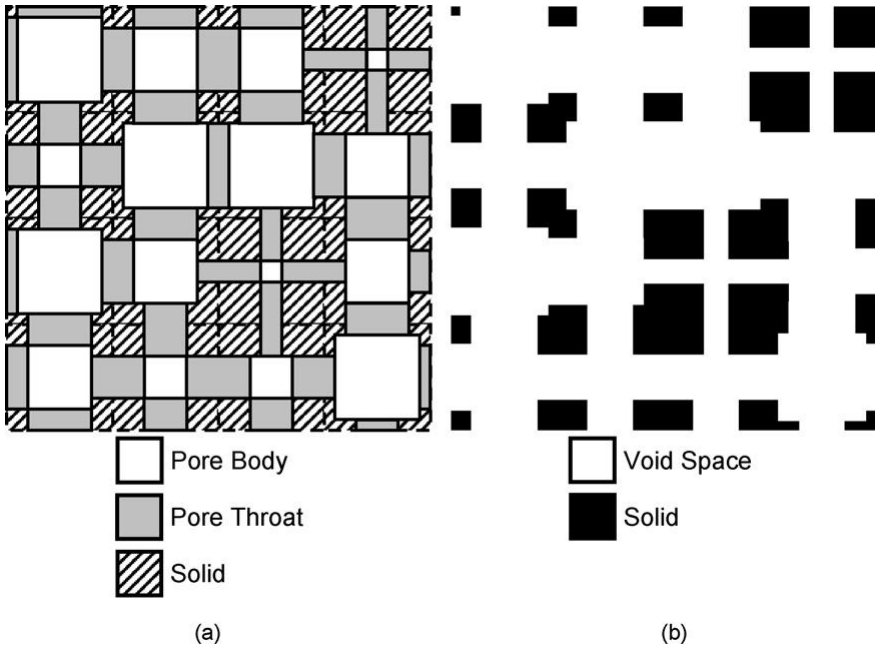

Figure 2.4: 2D schematic diagram of pore network construction (a) Relationship between pores, throats and solid; (b) Structure in terms of void and solid space [51]

It is then apparent that many models are available for obtaining the effective diffusion coefficient in the GDL. However, due to the geometry differences and the lack of experimental data for comparison, it becomes difficult to choose the most appropriate correlation. In recent years, estimating the effective diffusion coefficient, both experimentally and numerically, of gases in carbon paper has gained much interest. Using the limiting current density, Baker et al. [52] estimated the effective diffusion coefficient of an oxygen-nitrogen mixture through a TORAY carbon paper sample. They used Fick's law to relate the limiting current density to the effective diffusion coefficient as given below [52]:

$$D_{O_2}^{\text{eff}} = \left(\frac{fhi_{\text{lim}} RT}{4FP_{O_2}^{\text{in}}} \right) \tag{2.21}$$

where $D_{O_2}^{\text{eff}}$ is the effective diffusion coefficient of oxygen in nitrogen in carbon paper, f is a geometrical factor, h is the thickness of carbon paper, i_{lim} is the limiting current density, R is the universal gas constant, T is the temperature, F is Faraday's constant and $P_{O_2}^{\text{in}}$ is the partial pressure of oxygen at the channel/carbon paper interface.

Kramer et al. [53, 54] measured the effective diffusion coefficient in carbon paper using electrochemical impedance spectroscopy. Electrochemical impedance spectroscopy is applied to measure the effective ionic conductivity of an electrolyte-soaked carbon paper sample. The effective diffusion coefficient is then found using the analogy between Fick's and Ohm's laws. In their early study [53], they measured the effective diffusion coefficient through TORAY carbon paper with no wet-proofing. In their second study [54], they measured the effective diffusion coefficient through TORAY and SGL carbon paper with different Teflon percentage.

In a study by Schulz et al. [55], the stochastic simulation technique was used to create a 3-dimensional reconstruction of carbon paper, which was proposed by Schladitz et al. [56] and is based on a Poisson line process with one-parametric directional distribution where the fibers are realized as circular cylinders with a given diameter. In the study by Schulz et al. [55], they investigated the two-phase flow in the gas diffusion layer. In later studies [57, 58] the same method was used to investigate liquid water transport and its effects on the overall diffusion process of gases in the gas diffusion layer. Much of the work done in this area is summarized in the book chapter by Mukherjee and Wang [59].

The theoretical expressions for the diffusibility reviewed in this chapter and on which much of the discussion of this thesis is based are summarized in Table 2.1.

Table 2.1: Theoretical models for the effective diffusion coefficient

Model	**Mathematical Expression**	**Type**
Bruggeman Approximation [36]	$\frac{D_{\text{eff}}}{D_{\text{bulk}}} = \epsilon^{1.5}$	Effective medium approximation
Neale and Nader [40]	$\frac{D_{\text{eff}}}{D_{\text{bulk}}} = \frac{2\epsilon}{3-\epsilon}$	Effective medium approximation
Tomadakis and Sotirchos [42]	$\frac{D_{\text{eff}}}{D_{\text{bulk}}} = \epsilon\left(\frac{\epsilon-0.037}{1-0.037}\right)^{0.661}$	Percolation theory
Nam and Kaviany [47]	$\frac{D_{\text{eff}}}{D_{\text{bulk}}} = \epsilon\left(\frac{\epsilon-0.11}{1-0.11}\right)^{0.785}$	Percolation theory
Das et al. [48]	$\frac{D_{\text{eff}}}{D_{\text{bulk}}} = 1 - \frac{3(1-\epsilon)}{3-\epsilon}$	Effective medium approximation

2.3 Effective Thermal Conductivity

Thermal management is a crucial issue for polymer electrolyte membrane (PEM) fuel cells due to the heat generated during the electrochemical reactions. PEM fuel cells produce a similar amount of waste heat to their electric power output and can tolerate only a small deviation in temperature from their design point [60]. Heat transfer in the cell is further complicated by its coupling with water transport. Adsorption and release of latent heat are usually associated with the evaporation and condensation processes. Heat transfer in the various components (bipolar plates, gas diffusion layers, catalyst layers and electrolyte membrane) of the cell govern the temperature gradient across it. Hence, many parametric studies, which investigate the effects of design parameters on the temperature distribution, are found in literature (see [61-64]). In order to numerically simulate the transfer of heat in the gas diffusion layers, catalyst layers and electrolyte membrane, the so-called effective thermal conductivity is needed. The effective thermal conductivity is a property for porous materials and is a measure of the contribution of each phase to the thermal conductivity of the layer. This property highly depends on the materials under investigation due to its sensitivity to the distribution of the different species. In this thesis, the focus is on estimating the effective thermal conductivity of the carbon paper GDL. Theoretically, the effective thermal conductivity of the carbon paper GDL in PEM fuel cells is a function of the porosity and the thermal conductivity of the solid carbon, the gas species present and liquid water and can be written as follows:

$$k_{\text{eff}} = f\left(k_{\text{s}}, k_{\text{g}}, k_{\text{l}}, \epsilon, s\right) \tag{2.22}$$

where k_{eff} is the effective thermal conductivity of the carbon paper, ϵ is the porosity of the GDL, s is the liquid water saturation, k_{s}, k_{g} and k_{l} are the thermal conductivity of the solid, gas species and liquid water, respectively.

Estimating the effective thermal conductivity in carbon paper diffusion media is the focus of many theoretical and experimental studies. Ramousse et al. [65] experimentally measured the thermal conductivity of four carbon paper samples. They investigated the effects of manufacturing process and Teflon treatment on the effective thermal conductivity in carbon paper. They reported a maximum and minimum range of 0.3-1.36 and 0.20-0.36 $W/K.m$, respectively, for Quintech carbon paper. Their main conclusion was that many of the theoretical values for the effective thermal conductivity are highly overestimated in literature. Similar measurements were made by Khandelwal and Mench [66]. They measured the through-plane effective thermal conductivity for carbon materials manufactured

by two different manufactures with various Teflon treatments. The effective thermal conductivity of TORAY carbon paper (TGPH-60) was reported to decrease from 1.8 ± 0.27 to 1.24 ± 0.19 W/K.m with the increase of temperature from 26°C to 73°C. The addition of Teflon treatment reduced the effective thermal conductivity drastically. Using SIGRACET carbon paper with 0, 5 and 20 wt.% PTFE, the effective thermal conductivity was measured to be 0.48 ± 0.09, 0.31 ± 0.06 and 0.22 ± 0.04 $W/K.m$, respectively, at a temperature of 58°C. A thermal conductivity of 0.22 ± 0.04 $W/K.m$ at 33°C was measured for ETEK ELAT (a carbon paper GDL with a micro-porous layer). Vie and Kjelstrup [67] also determined the effective thermal conductivity for ETEK ELAT indirectly from measured temperature profiles. Their measured value was 0.2 ± 0.1 $W/K.m$. The effect of compression pressure on the through-plane effective thermal conductivity was studied by Nitta et al. [68]. Despite applying compression pressures up to 5.5 MPa, they concluded that the ETC of TORAY TGPH-060 is not affected by compression. Using SolviCor carbon paper, Burheim et al. [69] reported the thermal conductivity to be 0.27 ± 0.03, 0.36 ± 0.08 and 0.40 ± 0.04 $W/K.m$ for a dry material under 4.6, 9.3 and 13.9 bar compaction pressures, respectively. They further suggested that the thermal conductivity increases by up to 70% due to a residual liquid water saturation of 25%. Karimi et al. [70] determined the through-plane thermal conductivity of various gas diffusion layer materials and under different compression loads and PTFE content at $70°C$. The effective thermal conductivity of SpectraCarb untreated carbon paper was found to vary from 0.26 to 0.7 $W/K.m$ as the compression load increased from 0.7 to 13.8 bars. The presence of a microporous layer and PTFE on SolviCore diffusion material reduced the effective thermal conductivity in comparison to the pure carbon fibers. In the studies by Sadeghi et al. [71, 72], the effect of cyclic compression was taken into account. In [72], they observed a hysteresis effect in the total thermal resistance, thermal contact resistance, effective thermal conductivity, thickness and porosity due to the cyclic compression. They sought to show that the thermal contact resistance is a critical interfacial transport phenomenon and should not be neglected in fuel cell simulations. All the previous studies have been focused on measuring the thermal conductivity in the through-plane direction. Recently, Teerstra et al. [73] measured the in-plane thermal conductivity of carbon paper. Their measurements were made for a mean temperature of $70°C$. They found that depending on the manufacturing process, treatment and orientation of paper during measurement, the in-plane thermal conductivity can vary from a minimum of $3.54 W/m.K$ to a maximum value of $15.1 W/m.K$.

The effective thermal conductivity of the gas diffusion layer has also been estimated analytically [74], numerically [75] and theoretically [62, 63, 76-78]. The theoretical values range

from as high as 65 to as low as 0.15 $W/K.m$. Unlike the effective diffusion coefficient, there are no specific correlations for the effective thermal conductivity in the carbon paper diffusion media of PEM fuel cells. An arithmetic mean correlation, Equation (2.23), is sometimes used [79, 80] to describe the effective thermal conductivity as a function of the porosity and thermal conductivity of the solid and gas species. In other instances, a value for the effective thermal conductivity that lies between a maximum, Equation (2.23), and a minimum, Equation (2.24), is sometimes used [81]. These equations are based on averaging the thermal conductivity of the regions of the porous medium (k_s, k_f) with respect to their volume fractions and are referred to as mixing-law models. With these models, the general character and the possible effect of structure is neglected; however, they still provide convenient predictions for the physical limits of the effective thermal conductivity. The arithmetic mean (Equation (2.23)) was developed by Aichlmayr and Kulacki [82] based on a series arrangement of the components relative to the direction of heat flow, while a parallel arrangement was used to obtain the harmonic mean (Equation (2.24)) by Woodside and Messer [83, 84]. These limits originated from the Wiener bounds [85, 86]. The geometric mean model (Equation (2.25)) provides an intermediate value of the arithmetic and harmonic means and was correlated by Woodside and Messer [83, 84]. These models have been correlated for an isotropic bed of rocks. Many other correlations of the effective thermal conductivity of various porous materials have been reported in literature [87, 88].

$$k_{\text{max}}^{\text{eff}} = \epsilon k_f + (1-\epsilon)\, k_s \tag{2.23}$$

$$k_{\text{min}}^{\text{eff}} = \left[\frac{(1-\epsilon)}{k_s} + \frac{\epsilon}{k_f}\right]^{-1} \tag{2.24}$$

$$k_{\text{intermed}}^{\text{eff}} = k_f^{\epsilon} k_s^{(1-\epsilon)} \tag{2.25}$$

where k_s and k_f are the solid and fluid thermal conductivities, respectively, $k_{\text{max}}^{\text{eff}}$, $k_{\text{min}}^{\text{eff}}$ and $k_{\text{intermed}}^{\text{eff}}$ are the maximum, minimum and intermediate effective thermal conductivities, respectively and ϵ is the porosity of the medium.

The maximum and minimum limits given by Equations (2.23) and (2.24) were modified by Hashin and Shtrikman [49] to give stricter bounds as given below:

$$\phi_1 + \frac{3f_2\phi_1\,(\phi_2-\phi_1)}{3\phi_1 + f_1\,(\phi_2-\phi_1)} \geq \phi_{\text{eff}} \geq \phi_2 + \frac{3f_1\phi_2\,(\phi_1-\phi_2)}{3\phi_2 + f_2\,(\phi_1-\phi_2)} \tag{2.26}$$

where ϕ_1 and ϕ_2 are the bulk properties of phases 1 and 2, respectively, f_1 and f_2 are the

volume fractions of phase 1 and 2, respectively and ϕ_{eff} is the effective property of the coated sphere assemblage. For Equation (2.26) to hold, $\phi_1 > \phi_2$. These bounds have been developed by considering a composite system composed of a large number of coated spheres as shown earlier in Figure 2.2.

2.4 Effective Electrical Conductivity

Similarly to gaseous species transport and heat transfer in the GDL, the transport of electrons is one of the major determinants of the rate of the electrochemical reaction. Again, numerical modeling is often utilized to simulate the transport of electrons in the GDL and the macro-homogeneous assumption is used to simplify the overall structure of the layer. Hence, the so-called effective electrical conductivity is used. The effective electrical conductivity is a function of the solid electrical conductivity and the structure of the GDL as follows:

$$\sigma_{\text{eff}} = \sigma_{\text{solid}} f(\epsilon) \tag{2.27}$$

where σ_{eff} and σ_{solid} are the effective and solid electrical conductivity, respectively and $f(\epsilon)$ is the structural function based on the porosity, ϵ, of the carbon paper GDL.

Estimating the effective electrical conductivity has just recently gained some interest. Although it is easier to measure experimentally than the effective diffusion coefficient and the effective thermal conductivity, not much work is found in literature. Williams et al. [89] reported experimental measurements of the in-plane electronic resistivity of carbon paper manufactured by SGL Carbon Group and TORAY. They showed that the electrical conductivity is highly dependent on the bare carbon paper used and the treatment it undergoes (addition of micro-porous layer and Teflon). Recently, Nitta et al. [90] measured the through-plane and in-plane effective electrical conductivity of SGL SIGRACET 10-BA carbon paper under various compression force. They showed that the electrical conductivity is linearly dependent on the compressive force and increases with the increase in the pressure. They argued that this increase is due to the decrease in the overall porosity of the carbon paper GDL and the reduced fiber electric resistance with pressure. Other values for the through-plane and in-plane effective electrical conductivity have been reported in literature for TORAY and SGL carbon paper and they vary depending on the physical and structural properties of the carbon paper GDL. The reported values range from 5,000 to 23,000 Sm^{-1} for the in-plane conductivity and from 300 to 1,400 Sm^{-1} for the through-plane conductivity [91, 95].

In describing the electrical conductivity of the carbon paper GDL, the physical model known as the effective medium approximation is usually used. This approximation is based on the properties and relative fractions of the components of the porous medium and is often used to describe the conductivity or the dielectric constant of the medium. These two parameters are often interchangeable in the formulas due to the wide applicability of the Laplace equation. Most of the approximations in literature based on this theory are derived for homogeneous structures consisting of either spherical or ellipsoidal particles [36, 96, 97]. Some theoretical approximations of the electrical conductivity also exist in literature with the Bruggeman Approximation being the most widely used for PEM fuel cell modeling. This approximation is commonly written as [36]:

$$\frac{\sigma_{\text{eff}}}{\sigma_{\text{solid}}} = (1-\epsilon)^m \tag{2.28}$$

where m is the Bruggeman exponent and its widely used value is 1.5.

Using similar principals of derivation as that of the Bruggeman Approximation, the electrical conductivity of a homogeneous porous structure can also be written using the relation proposed by Looyenga [96] and is given as:

$$\frac{\sigma_{\text{eff}}}{\sigma_{\text{solid}}} = (1-\epsilon)^3 \tag{2.29}$$

As the dielectric constant of multiphase mixtures is also of interest in many studies, the generalized Maxwell equation is often applied to find various expressions. The Maxwell equation is another form of the effective medium approximation and simply states that the effective dielectric constant is a function of the dielectric constant of the inclusions and the matrix as well as the volume fraction of the embedded material. This type of analysis was used by Das et al. [48] to develop an expression for the effective electrical conductivity of the carbon paper GDL. Their expression was based on the Hashin bounds [49] where these bounds have been developed for a homogeneous mixture of spherical particles and state that the effective properties of a porous material must lie between an upper and lower bound, in other words, these bounds are written as:

$$\eta_2 + \frac{3f_1\eta_2\left(\eta_1-\eta_2\right)}{3\eta_2+f_2\left(\eta_1-\eta_2\right)} \leq \eta_{\text{eff}} \leq \eta_1 + \frac{3f_2\eta_1\left(\eta_2-\eta_1\right)}{3\eta_1+f_1\left(\eta_2-\eta_1\right)} \tag{2.30}$$

where η_1 and η_2 are the bulk properties of phases 1 and 2, respectively, f_1 and f_2 are the volume fractions of phases 1 and 2, respectively and η_{eff} is the effective property of the homogeneous mixture. Using these bounds, Das et al. formulated an expression for the

electrical conductivity of a coated sphere assemblage, which is given by [48]:

$$\frac{\sigma_{\text{eff}}}{\sigma_{\text{solid}}} = \frac{2 - 2\epsilon}{2 + \epsilon} \tag{2.31}$$

2.5 Intrinsic and Relative Permeability and Capillary Pressure

While the overall permeability is independent of the fluid, the relative permeability of a phase is defined as the ratio of the intrinsic permeability of the phase at a given saturation to the total intrinsic permeability of the porous medium. The intrinsic permeability of the gas diffusion layer has been numerically and experimentally investigated by many studies ([98-102]).

The Kozeny-Carman equation is a semi-empirical formula that is typically used to estimate the intrinsic permeability of porous media and is given by:

$$K = \frac{\epsilon^{n+1}}{C\left(1 - \epsilon\right)^{n}} \tag{2.32}$$

where the exponential n and constant C are called Kozeny-Carman constants and these two constants vary for different porous media. For the purpose of estimating the intrinsic permeability of the carbon paper GDL, $n = 2$ [101].

Tomadakis and Robertson [101] also proposed a more comprehensive relationship to predict the anisotropic permeability of in-plane and through-plane of randomly overlapping fiber structures as given below:

$$K = R^2 \frac{\epsilon\left(\epsilon - \epsilon_p\right)^{\alpha+2}}{8\left(\ln \epsilon\right)^2 \left(1 - \epsilon\right)^{\alpha} \left[\left(\alpha + 1\right)\epsilon - \epsilon_p\right]^2} \tag{2.33}$$

where R is the radius of the fibers, ϵ_p is the percolation threshold and α a constant depending on the structure and the flow direction. Tomadakis and Robertson [101] reported that $\epsilon_p = 0.11$ regardless of direction and α is 0.521 and 0.785 for the in-plane and through-plane directions, respectively.

Using a fractal approach, Hao and Cheng [102] proposed that the permeability can be expressed in terms of the tortuosity and porosity as:

$$K = \frac{\lambda_{\max}^2}{32\tau} \frac{2 - Df}{4 - Df} \frac{\epsilon}{1 - \epsilon} \tag{2.34}$$

where $\lambda_{\max}$ is the maximum pore size, τ is the tortuosity and Df is the area fractal dimension and was found by Yu and Li [103] to be related to the porosity as follows:

$$\epsilon = \left(\frac{\lambda_{\min}}{\lambda_{\max}}\right)^{d_E - Df} \tag{2.35}$$

where $\lambda_{\min}$ is the minimum pore size of the GDL and d_E is the Euclid dimension.

The relative permeability of a phase describes the extent to which one phase is hindered by the other phases co-existing in the pore space. Many models have been developed to predict the relative permeability of the wetting and non-wetting phases. These models have been developed from conceptual models of flow in capillary tubes combined with models of pore-size distribution [104]. In general, the relative permeability of a porous material can be represented in terms of the capillary pressure and the wetting phase saturation using the Burdine [105] and Mualem [106] functions as given below:

$$\kappa_{\mathrm{rwp}} = s_{\mathrm{wp}}^2 \left[\frac{\int_0^{s_{\mathrm{wp}}} \frac{ds_{\mathrm{wp}}}{P_c^2}}{\int_0^1 \frac{ds_{\mathrm{wp}}}{P_c^2}}\right] \qquad \kappa_{\mathrm{rnw}} = (1 - s_{\mathrm{wp}})^2 \left[\frac{\int_{s_{\mathrm{wp}}}^1 \frac{ds_{\mathrm{wp}}}{P_c^2}}{\int_0^1 \frac{ds_{\mathrm{wp}}}{P_c^2}}\right] \tag{2.36}$$

$$\kappa_{\mathrm{rwp}} = s_{\mathrm{wp}}^{\eta} \left[\frac{\int_0^{s_{\mathrm{wp}}} \frac{ds_{\mathrm{wp}}}{P_c}}{\int_0^1 \frac{ds_{\mathrm{wp}}}{P_c}}\right]^2 \qquad \kappa_{\mathrm{rnw}} = (1 - s_{\mathrm{wp}})^{\eta} \left[\frac{\int_{s_{\mathrm{wp}}}^1 \frac{ds_{\mathrm{wp}}}{P_c}}{\int_0^1 \frac{ds_{\mathrm{wp}}}{P_c}}\right]^2 \tag{2.37}$$

where Equations (2.36) and (2.37) represent the Burdine and Mualem functions, respectively, κ_{rw} and κ_{rnw} denote the relative permeability of the wetting and non-wetting phases, respectively, P_c is the capillary pressure, η is a factor that accounts for pores and flow path tortuosity and s_{wp} is the wetting phase saturation. In summary, these two functions rely on the knowledge of the relationship between the capillary pressure and the wetting phase saturation ($P_c(s_{\mathrm{wp}})$). Integration of this relationship yields the relative permeability. Two of the most commonly used expressions for $P_c(s_{\mathrm{wp}})$ are the van Genuchten function [107] and the Brooks-Corey function [108]. These two functions will be discussed further in this paper. The use of the van Genuchten relation for $P_c(s_{\mathrm{wp}})$ along with the Mualem function, Equation (2.38) is obtained for the relative permeability of the wetting and non-wetting phases. Similarly, the use of the Brooks-Corey function for $P_c(s_{\mathrm{wp}})$ along with the Burdine function, Equation (2.39) is obtained for the relative permeability of the wetting and non-wetting phases.

$$\kappa_{\mathrm{rwp}} = s_{\mathrm{wp}}^{\eta} \left[1 - \left(1 - s_{\mathrm{wp}}^{1/m}\right)^m\right]^2 \qquad \kappa_{\mathrm{rnw}} = (1 - s_{\mathrm{wp}})^{\eta} \left(1 - s_{\mathrm{wp}}^{1/m}\right)^{2m} \tag{2.38}$$

$$\kappa_{\mathrm{rwp}} = s_{\mathrm{wp}}^{3+2/\lambda} \qquad \kappa_{\mathrm{rnw}} = (1 - s_{\mathrm{wp}})^2 \left(1 - s_{\mathrm{wp}}^{1+2/\lambda}\right) \tag{2.39}$$

where m is a fitting parameter and λ describes the pore distribution.

For the purpose of modeling liquid water transport in the GDL of PEM fuel cells, the power law function [87] is the most widely used with the general form written as:

$$\kappa_{\mathrm{rwp}} = s_{\mathrm{wp}}^{n} \qquad \kappa_{\mathrm{rnw}} = (1 - s_{\mathrm{wp}})^n \tag{2.40}$$

where n is a fitting parameter.

As mentioned earlier, the relative permeability is dependent on the capillary pressure, which is defined as the difference in pressure across the interface between two immiscible fluids, and thus defined as:

$$P_c = P_{\mathrm{non-wetting}} - P_{\mathrm{wetting}} \tag{2.41}$$

where P_c is the capillary pressure and $P_{\mathrm{non-wetting}}$ and P_{wetting} are the pressure of the non-wetting and wetting phases, respectively.

Normally a liquid water droplet is taken to be in the shape of a cylindrical pore and hence, the capillary pressure can be written in the general form as a function of the pore size, contact angle and surface tension [109]:

$$P_c = \frac{2\sigma \cos\theta_c}{r} \tag{2.42}$$

where σ is the surface tension, and r is the radius of the cylindrical pore and θ_c is the contact angle and depends on the properties of the material. The contact angle is defined as the angle between the liquid-gas interface and the solid surface where all three phases intersect. The hydrophobicity of the material determines the contact angle. A hydrophilic medium has a contact angle less than 90°, while the contact angle of a hydrophobic medium is greater than 90°.

The capillary pressure of two-phase flow in a porous medium can be represented by the following empirical correlation [110]:

$$P_c = \sigma \cos(\theta_c) \left(\frac{\epsilon}{K}\right)^{0.5} f(s) \tag{2.43}$$

where the term $f(s)$ is known as the Leverett function and represents the dimensionless capillary pressure as a function of liquid saturation, $\left(\frac{\epsilon}{K}\right)^{0.5}$ is the characteristic of the pore

length scale. The most widely used expression for the function $f(s)$ is:

$$f(s) = \begin{cases} 1.417(1-s) - 2.120(1-s)^2 + 1.263(1-s)^3 & \text{if } 0^\circ \leq \theta_c < 90^\circ \\ 1.417s - 2.120s^2 + 1.263s^3 & \text{if } 90^\circ < \theta_c < 180^\circ \end{cases} \tag{2.44}$$

where the above relation was proposed by Udell [111] using the experimental results by Leverett [110] for packed beds.

Other common models that are used to relate the capillary pressure to the wetting phase saturation are the van Genuchten (VG) model [107] (Equation (2.45)) and Brooks-Corey (BC) model [108] (Equation (2.46)).

$$s_{\text{wp}} = \left(1 + \left(\frac{P_c}{P_{cb}}\right)^n\right)^{-m} \tag{2.45}$$

$$s_{\text{wp}} = \left(\frac{P_c}{P_{cb}}\right)^{-\lambda} \tag{2.46}$$

where P_{cb} corresponds to a characteristic capillary pressure (break through pressure) associated with the first formation of a sample planning cluster of pores invaded by the non-wetting phase [112], m and n are fitting parameters and λ corresponds to the pore size distribution.

The function in Equation (2.44) has been criticized for its use in PEM fuel cell modeling since it ignores the detailed pore morphology of the GDL and only relies on the influence of porosity and permeability of the porous medium to estimate the capillary pressure. Hence, much work has been dedicated to measure the capillary pressure of a saturated carbon paper GDL. Some of the experiments that have been carried out can be found in [113-119]. Kumbur et al. [115-117] proposed correlations for the capillary pressure based on drainage measurements of the SGL 24 series and E-TEK Elat carbon cloth materials as given below:

$$P_c = 2^{0.4C}\left(\frac{293}{T}\right)^6 \sigma(T)\sqrt{\frac{\epsilon}{\kappa}} K(s_{\text{nw}})\, f(C) \tag{2.47}$$

where C is the compression rate, T is the temperature, σ is the surface tension, ϵ is the porosity of the layer, κ is the absolute permeability of the layer, $K(s_{\text{nw}})$ takes the effect of the non-wetting phase saturation into account and $f(C)$ is the effect of compression on the change in structure of the GDL and is given as:

$$f(C) = \left(\frac{0.9}{1 - 0.0083C^2 + 0.0911C} + 0.1\right)^{0.5} \tag{2.48}$$

Another correlation obtained for the capillary pressure was derived by Ye and Nguyen [120] based on the experimental data of Nguyen et al. [113]. Using a volume displacement technique, the capillary pressure within a Toray TGP-H-060 with 10% PTFE loading was measured. The capillary pressure in pascals is evaluated using:

$$P_c = 2.09\left(e^{22.2(0.321-s)} - e^{44.9(0.321-s)}\right) + 35.6 \tag{2.49}$$

It should be pointed out here that the capillary pressure used to obtain the correlation in Equation (2.49) lies in a relatively small range. The measured capillary pressure is one to two orders of magnitude smaller than that of [114-117, 119]. Physically, smaller capillary pressure means higher water retention ability; hence, a higher level of saturation would be expected for this expression.

Another correlation has been proposed by Natarajan and Nguyen [121] for the capillary head in centimeters and it is given as:

$$H_c = 0.0173\left[\exp\left(-3.7\left(s-0.494\right)\right) - \exp\left(3.7\left(s-0.494\right)\right) + 21\right] \tag{2.50}$$

From the discussion above, it is clear that there is much debate as to the relation between the capillary pressure and liquid water saturation. The choice of an expression for the capillary pressure is very crucial for simulating liquid water transport in the cell as has been shown by Wu et al. [122] as they investigated the effect of the capillary expressions by Leverett (Equation (2.44)), Kubmur et al. (Equation (2.47)) and Ye and Nguyen (Equation (2.49)).

2.6 Summary of Chapter

In this chapter, a detailed overview of the work on the effective transport properties of the carbon paper GDL published in literature has been put forward. Despite the fact that many of these studies mentioned above have been focused on estimating the effective properties of the carbon paper GDL, much work is still lacking. Hence, in this thesis, the effective transport properties will be estimated numerically and experimentally.

Chapter 3

Experimental Setup

In this chapter, the experimental methods utilized for the purpose of this thesis research to further investigate the transport properties of the carbon paper GDL are discussed. In this chapter, four measurements techniques are described, the method of standard porosimetry, the Loschmidt cell and the method of monotonous heating. The method of standard porosimetry is used to characterize the structure of the carbon paper GDL as well as to measure the capillary pressure versus the liquid phase saturation. The Loschmidt cell is a diffusion cell, which is used to measure the through-plane diffusion coefficient of the carbon paper GDL. Finally, the method of monotonous heating is the method used for the measurement of the thermal conductivity of the carbon paper GDL. Two variants of this method are used; one for the in-plane conductivity measurements and the other for the through-plane measurements.

3.1 Structure Characterization by the Method of Standard Porosimetry

In order to understand the effect of PTFE on the structure of carbon paper, the pore distribution of the carbon paper under investigation was analyzed using the Method of Standard Porosimetry (MSP). This method [123-125] depends on the use of standard samples to measure the change of working fluid inside the carbon paper GDL and has been used in other studies to investigate the capillary pressure and wettability effects of the carbon paper GDL [114, 118]. While in contact, the standard and the sample are in capillary equilibrium, the known capillary pressure in the standard is the same as that in the sample. The capillary pressure is varied by allowing the standard and sample to dry slowly while in contact; hence,

both their capillary pressure is varied together. The saturation of the working fluid is found by weighing the sample and the standard periodically. From this, the capillary pressure of the sample can be obtained from the known capillary pressure curve of the standard. This method, however, is limited to scanning only in the direction of decreasing liquid phase saturation.

The standard sample is a porous disk that is designed in such a way so that the fluid/solid contact angle is exactly 0°. In this thesis, the wetting fluid used is ACS grade octane (99.99%). In order to ensure that no air is trapped in the material when the liquid enters, the GDL sample and the standard are first evacuated and then flooded with the fluid. Once the samples are exposed to air, the octane will slowly evaporate from both the sample and the standard, resulting in a changed saturation as illustrated by Figure 3.1.

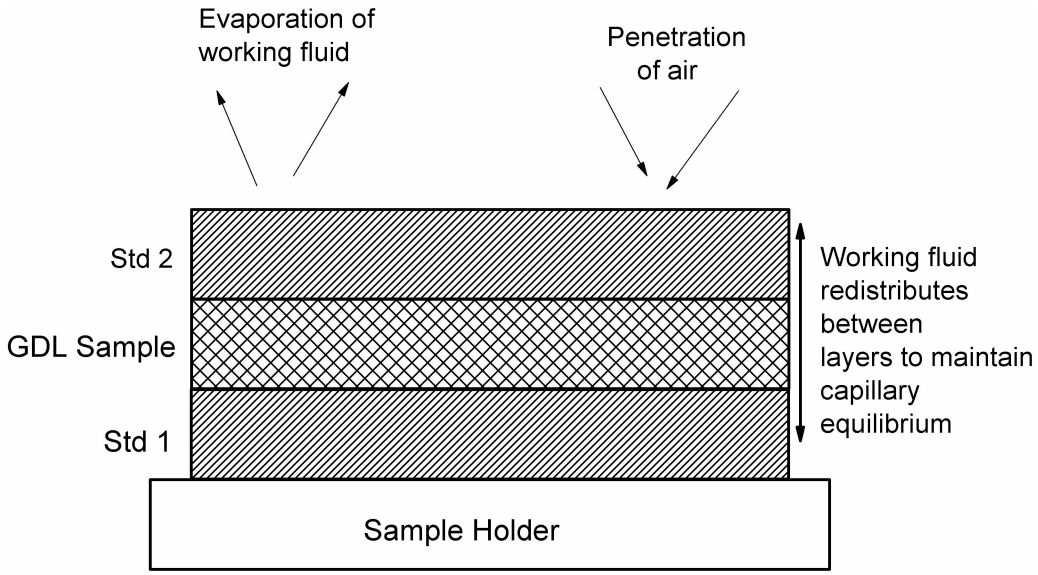

Figure 3.1: Schematic of sample and standards showing fluid movement occurring during method of standard porosimetry experiment.

The generation of a capillary pressure versus saturation curve from this process is shown in Figure 3.2. The process of this method is a three step process. First step (Figure 3.2(a)) involves the periodic separation and weighing of the standards and samples individually in order to obtain their respective saturation levels. Since the standards have a known capillary pressure curve (Figure 3.2(a)), their capillary pressure can be found from the knowledge of their saturation, which is Step 2 in this process and is shown in Figure 3.2(b). The final step is based on the assumption that the samples and the standard are in capillary equilibrium; hence, the capillary pressure of the sample is equated to the capillary pressure

of the standards and so the sample saturation can be related to the standards' capillary pressure as illustrated by Figure 3.2(c). The test is then said to be complete once the working fluid is fully evaporated from the sample.

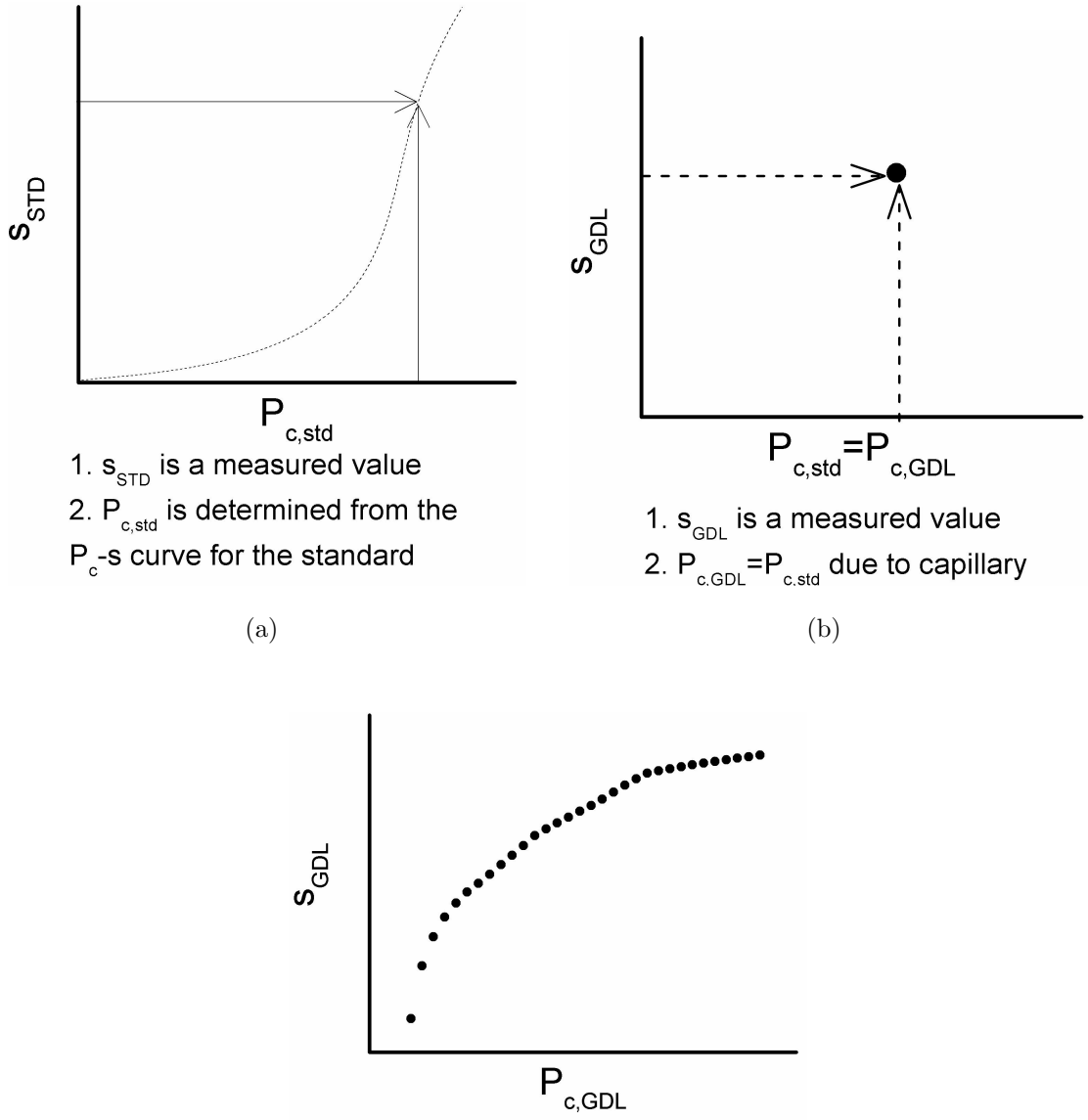

Figure 3.2: Procedure for obtaining GDL capillary pressure curves using MSP.

Although octane is used as the working fluid, the results of this investigation can be used to understand the invasion by liquid water. When using octane as the wetting fluid, the

capillary pressure in terms of the octane saturation can be found and can be transformed to take into account liquid water. This transformation is based on the following relation:

$$P_{\text{c,water}} = \frac{\sigma_{\text{water-air}} \cos\theta_{\text{water-air}}}{\sigma_{\text{octane-air}} \cos\theta_{\text{octane-air}}} P_{\text{c,octane}} \tag{3.1}$$

where $P_{\text{c,water}}$ is the capillary pressure of the water-air system, $P_{\text{c,octane}}$ is the capillary pressure of the octane-air system, $\sigma_{\text{water-air}}$ and $\sigma_{\text{octane-air}}$ are the surface tensions of water and octane, respectively, and $\theta_{\text{water-air}}$ and $\theta_{\text{octane-air}}$ are the contact angles of water and octane, respectively. For the purpose of evaluating the capillary pressure for the water-air system for the purpose of this thesis, $\sigma_{\text{water-air}} = 72$ dyne/cm, $\sigma_{\text{octane-air}} = 21.75$ dyne/cm, $\theta_{\text{water-air}} = 112^\circ$ [114] and $\theta_{\text{octane-air}} = 0^\circ$.

3.2 Effective Diffusion Coefficient

3.2.1 Experimental Apparatus

To measure the diffusion coefficient of a carbon paper sample, a Loschmidt cell consisting of two chambers is used as shown in Figure 3.3. This cell has been developed at NRC-Institute for Fuel Cell Innovation (IFCI). The cell consists of a top (a) and bottom (b) chambers with the interior length and diameter of each chamber as 177.5 mm and 20.6 mm, respectively. The chambers can be connected, position (5a), or separated, position (5b), by a ball valve (5). The ball valve, which is considered as part of the bottom chamber, is an Apollo 86-104-49. The upper side of the ball valve marks the middle of the diffusion cell and is represented as $z = 0$ on the coordinate system. Two mass flow controllers (Omega, Model FMA-5508) with a flow capacity of 0-500 mL/min are connected to the inlets (1 and 2) to control the gas flow rate when the chambers are filled with the gases. An oxygen sensor (Ocean Optics FOXY-AL300) is used to measure the diffusion of an oxygen mixture. Its 300 μm in diameter aluminum jacketed optical fiber probe is installed in the top chamber at a position of $z = 19$ mm, represented as (6) in the figure. On the tip of the optical fiber probe, ruthenium complex in a sol-gel substrate is applied. The probe is connected to an excitation source and a spectrometer (Ocean Optics S2000-FL) by a bifurcated optical fiber. The spectrometer is connected by the computer via a USB A/D converter (Ocean Optics ADC 1000). The response time of the oxygen sensor was around 1 second and the accuracy is 1% of full range for 0-100% (mole percent). For measurements involving water vapor in the mixture, a relative humidity sensor (Sensirion SHT75) is used. A humidifier system is

coupled with the supplied gases at both inlets (1 and 2). The system (TesSol FCTS BH 500) is used to control the relative humidity in the range of 0-90%. The relative humidity in both chambers is monitored using two relative humidity sensors (7 and 8).

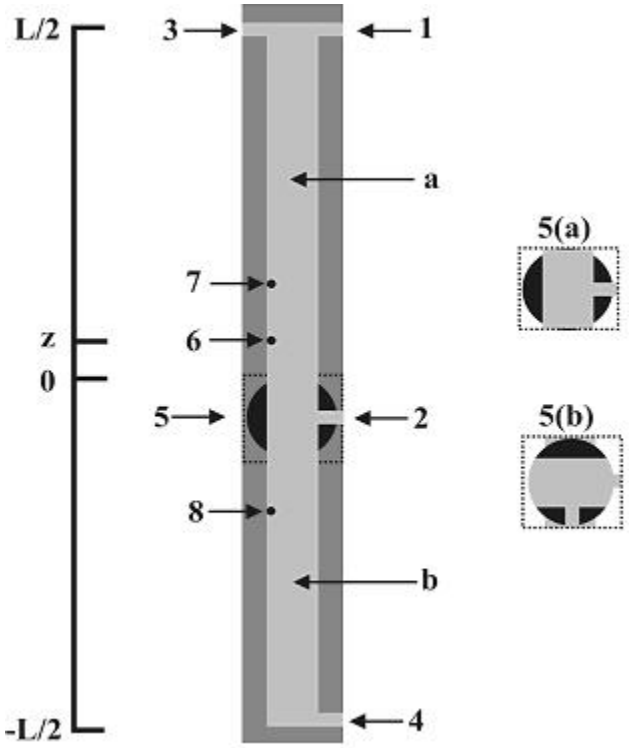

Figure 3.3: Schematic diagram of the diffusion cell - 1: gas inlet 1; 2: gas inlet 2; 3 and 4: outlets; 5: a ball valve; 5(a): open position of valve; 5(b) closed position of valve; 6: oxygen sensor; 7 and 8: humidity sensors.

The oxygen and relative humidity sensors are used to measure the change of oxygen and water vapor concentration with time. The system is built so that the diffusion process of gases would follow the one-dimensional Fick's law of diffusion. The validity of this assumption was evaluated in detail in [126, 127]. Thus, the diffusion process in the Loschmidt cell is governed by the following equation:

$$\frac{\partial C_i}{\partial t} = D_{i-j}^{\mathrm{eq}} \frac{\partial^2 C_i}{\partial z^2} \tag{3.2}$$

where D_{i-j}^{eq} is the so-called equivalent diffusion coefficient of species i in j, z is the spatial dimension and the general solution to this one-dimensional diffusion process is [128]:

$$C_i = \frac{C_i^b}{2} \mathrm{erfc}\left(\frac{z}{2\sqrt{(t-t_0)\, D_{i-j}^{\mathrm{eq}}}}\right) \tag{3.3}$$

where C_i^b is the initial concentration of species i in the bottom chamber and t_0 is the time delay at which diffusion commences.

3.2.2 Data Analysis

In order to obtain the equivalent diffusion coefficient, the measured concentration over time is fitted to Equation (3.3) as shown in Figure 3.4. The presence of t_0 should be pointed out here. The diffusion process is delayed by about 125 seconds in order to ensure the accuracy of the measurements.

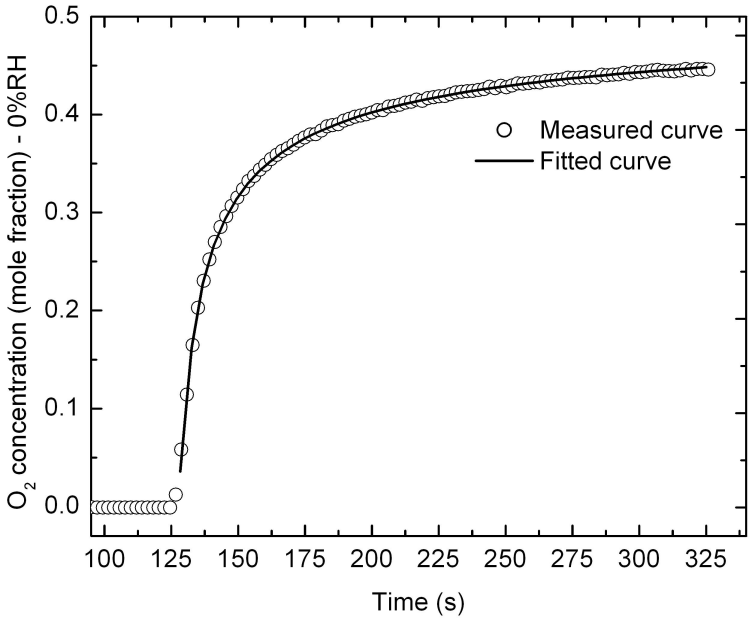

Figure 3.4: Sample data fitting - the concentration evolution of oxygen in nitrogen at $79°C$ determined by oxygen sensor with 0% relative humidity (open circles). The continuous line represents the best curve fit using Equation (3.3) to the experimental data.

After obtaining the equivalent diffusion coefficient, the resistance network shown in Figure 3.5 is used to find the effective diffusion coefficient in the carbon paper GDL. From this network, it is found that the equivalent resistance, R_{eq}, is due to the diffusion in the sample and in the chamber and is obtained by:

$$R_{\text{eq}} = \frac{z}{D_{i-j}^{\text{eq}} A_c} \tag{3.4}$$

where z is the distance from the zero axis to the oxygen sensor and A_c is the cross sectional area of the interior of the chamber, which is available for diffusion.

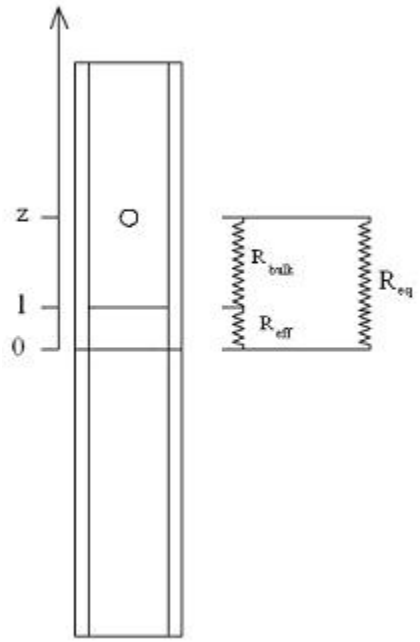

Figure 3.5: Resistance network due to diffusion in the chamber and the sample - R_{eq} is the equivalent resistance, R_{eff} is the resistance due to the diffusion in the sample and R_{bulk} is the resistance due to the diffusion in the chamber.

The resistance due to the diffusion in the chamber is denoted by R_{bulk} and is calculated below:

$$R_{\text{bulk}} = \frac{z - l}{D_{i-j}^{\text{bulk}} A_c} \tag{3.5}$$

where l is the thickness of the sample.

Similarly, the resistance due to the diffusion in the sample, R_{eff}, is found by:

$$R_{\text{eff}} = \frac{l}{D_{i-j}^{\text{eff}} A_c} \tag{3.6}$$

Combining Equations (3.4-3.6), the equivalent resistance becomes:

$$R_{\text{eq}} = \frac{z}{D_{i-j}^{\text{eq}} A_c} = \frac{z - l}{D_{i-j}^{\text{bulk}} A_c} + \frac{l}{D_{i-j}^{\text{eff}} A_c} \tag{3.7}$$

From Equation (3.7), the effective diffusion coefficient, D_{i-j}^{eff}, can then be obtained as:

$$D_{i-j}^{\text{eff}} = \frac{l}{\frac{z}{D_{i-j}^{\text{eq}}} - \frac{z-l}{D_{i-j}^{\text{bulk}}}} \tag{3.8}$$

3.2.3 Experimental Conditions

In this thesis, the effect of the temperature and Teflon treatment on the effective diffusion coefficient is measured. The experimental conditions of this thesis are summarized as follows:

1. The effect of the temperature of an oxygen-nitrogen mixture on the effective diffusion coefficient of oxygen in nitrogen is measured for a temperature range of 25-80 °C. The sample used is a TORAY carbon paper (TPGH-120) with no Teflon treatment and a thickness of 370 μm.

2. The effect of Teflon treatment on the effective diffusion coefficient of oxygen-water vapor in nitrogen-water vapor is measured for a Teflon treatment range of 0-40% by weight. The sample used is a TORAY carbon paper (TPGH-120) with variable Teflon treatment percentage and a thickness of 370 μm.

All the measurements are made under atmospheric pressure.

3.2.4 Uncertainty Analysis

In order to ensure the accuracy and repeatability of the measurements a total of 60 repeated measurements at different days and different times of the day are made for each measurement condition (or data point). The accuracy of the measurements is then evaluated using the standard deviation of the measurements with a 95% confidence interval. The measured effective diffusion coefficients (data points) reported in this thesis are then the average of all the repeated measurements within 95% confidence levels.

3.3 Effective Thermal Conductivity Measurements

Heat management of polymer electrolyte membrane (PEM) fuel cells is important under all operation conditions since it accounts for much of the losses in the cell. Recently, much interest has been dedicated to understanding heat transport in fuel cells operating in sub

zero conditions. Start-up of PEM fuel cells under sub zero conditions is critical for the commercialization of these cells for practical applications, such as backup power and automotive applications. Under these conditions, cyclic thawing and freezing occurs due to operation and shut down of the cell. In the presence of ice, the pores of the catalyst layer could be blocked hindering the transport of reactant gases to the reaction sites. Numerical simulations are often used to understand the heat transport under these conditions [129, 132]. A successful cold start process depends on the heating up of the catalyst layer, which is governed by the heat transport in all the other components of the cell and specifically the gas diffusion layer (GDL). Hence, the use of accurate thermal conductivity of the GDL in the numerical simulations is very crucial.

The temperature field and heat transfer in the thin anisotropic carbon paper can be determined by its apparent thermal conductivity and diffusivity, which are directionally dependent properties. As mentioned earlier in the introduction section, carbon paper is a fibrous material that is composed of graphitized carbon fibers, which are held together by a carbonized matrix [17]. The addition of PTFE is usually adopted to increase the hydrophobicity of the carbon paper and its mechanical durability. Typical operating temperatures of PEM fuel cells lay in the range of -30$^{\circ}C$ to +120$^{\circ}C$. In this temperature range, the thermal physical properties of the carbon paper can be used to determine its thermal durability.

The literature survey reveals that experimental measurements of the in-plane thermal conductivity of carbon paper is lacking in literature. However, to correctly simulate heat transfer in the gas diffusion layer (GDL), the anisotropic thermal conductivity should be taken into account. Anisotropic properties do not just have an effect on the overall cell performance, they also affect the local transport phenomena. Pharoah et al. [81] used a 2-dimensional simulation of the PEM fuel cell cathode to emphasize the need to appropriately characterize the relevant anisotropic properties of the GDL. They showed that neglecting the anisotropic nature and associated transport coefficients of the porous electrode significantly influences both the nature and the magnitude of the model predictions. Further, measurements of the thermal conductivity for sub zero temperatures is virtually non-existent in literature. The lack of these measurements could be due to the difficulty associated with measuring the directional dependency of such material in a wide range of temperature and during phase transformation. The evaluation of the thermal physical properties of carbon paper is necessary in both the through-plane and in-plane directions due to the anisotropic geometry of such a material. It is crucial to establish the dependency of thermal conductivity on temperature, which is especially important due to the change in crystal structure of the carbon during manufacturing. This type of analysis is limited in literature. Consequently,

the objective of this part of the thesis is to experimentally measure the in-plane and through-plane thermal conductivity of the thin carbon paper using the method of monotonous heating, which is widely used to measure other porous materials such as insulation materials. This method allows the measurements to be carried out for a wide range of temperature; thus, phase transformation in the presence of PTFE can be investigated. This type of investigation has both practical and scientific interest since new reference data is important for the further development of the GDL of PEM fuel cells and the verification of theoretical predictions.

In the following sections, the experimental apparatus, the experimental conditions and errors associated with the measurements are discussed. The discussion will cover both apparatus used for the in-plane and through-plane measurements.

3.3.1 Measurement of the In-plane Thermal Conductivity

The in-plane thermal conductivity was measured using a quasi-steady method based on monotonous heating. A monotonic heating regime is considered as a regime of heating or cooling of a solid when the rate of temperature change through the sample is maintained nearly uniform [133, 134, 137]. This regime is described by a generalization of the theory of quasi-steady conditions with constant rate heating, no dependency of the physical properties of the test samples on temperature and no internal heat sources or sinks. During this regime at $Fo > 0.5$, the temperature increases with the same and constant rate in all points of the sample [133, 134, 137]. This technique can be applied under the quasi-steady state condition for direct measurements of the thermophysical properties of the materials in a wide temperature range without the assumption about the linearity of the thermal conduction equation. The basic physical model of the heat transfer during monotonic heating can be described using a simple geometry (plate, disc, cylinder or sphere). These geometries can be used to study the thermophysical properties at monotonic heating conditions.

A temperature field, T(x=0,t), is developed inside the solid with regard to the base section, (x=0), with a temperature difference $\theta(x,t) = T(X,t) - T(0,t)$. The non-linear equation of the thermal conduction is:

$$\nabla \cdot (k \nabla T) = C\rho \left(\frac{\partial T}{\partial t} \right) \tag{3.9}$$

where k is the thermal conductivity, C is the heat capacity, ρ is the density, T is the temperature and t is time. The application of the monotonous heating method to the

measurement of the in-plane thermal conductivity, in this study, is explained in more detail in the next section.

3.3.1.1 Experimental Apparatus

In order to obtain the in-plane thermal conductivity of the carbon paper samples, the thermal diffusivity was measured by the method of monotonous heating at Integrity Testing Laboratory (ITL) in Markham, Ontario. A schematic drawing of the method and the setup used for the measurements in this study are shown in Figure 3.6, respectively. To measure the in-plane thermal diffusivity, a multi-layer sample composed of 12 layers of identical samples was used as shown in Figure 3.6(c). In describing the samples as identical, it is meant that the samples are taken from the same batch in order to ensure that their porous structure is as identical as possible. Thermocouples with an outer diameter of 0.8 (mm) were mounted in the middle between layers. The thermocouples were insulated by Teflon insulation. The two sides of the sample were fitted between two alumina plates heated by two heaters (Figure 3.6(c)). The two cylindrical heaters were placed between aluminum plates. The high thermal conductivity of aluminum ensured the uniform temperature field across the sample.

The outer surfaces of the sample were insulated by fiber insulation material (not shown in Figure 3.6(c))to ensure a one-dimensional heat flux in the in-plane direction through the sample. One dimensional temperature distribution in the sample was ensured by the high thermal conductivity of the aluminum plates and the very small thermal conductivity of the side insulation (0.025 W/m.K).

In this study, the basic physical model of the heat transfer during the monotonic heating can be described using the simple geometry of a square (as given in Figure 3.6(a)). Inside this sample, a temperature field is developed following the non-linear equation of thermal conduction given earlier in Equation (3.9). For one dimensional unsteady heat conduction with constant properties, Equation (3.9) can be re-written as:

$$\frac{\partial^2 T}{\partial x^2} = \frac{1}{\alpha}\frac{\partial T}{\partial t} = \frac{b}{\alpha} = \text{constant} \tag{3.10}$$

where $b = \dfrac{\partial T}{\partial t}$ is the rate of heating, which is maintained constant during the experiment, $\alpha = \dfrac{k}{C\rho}$ is the diffusivity of the material. With the rate of heating maintained constant during the experiment, Equation (3.10) becomes a second order, in terms of direction x,

separable ODE and, in this study, is subject to the following boundary conditions:

$$\begin{aligned} \theta_{-X} &= T_1 - T_0 \\ \theta_{+X} &= T_2 - T_0 \end{aligned} \tag{3.11}$$

where $\theta_{-X} = T_1 - T_0$ and $\theta_{+X} = T_2 - T_0$ are the differences of temperature between points on the edges of the sample and the center and are measured quantities.

Applying the boundary conditions given by Equation (3.11), the solution to Equation (3.10) yields:

$$\alpha = \frac{bR^2}{\theta_{-X} + \theta_{+X}} = \frac{bL^2}{2\theta} \tag{3.12}$$

where $\theta = \dfrac{\theta_{-X} + \theta_{+X}}{2}$ is the average temperature difference between the points near the two surfaces and L is the distance between the center and edge of the sample.

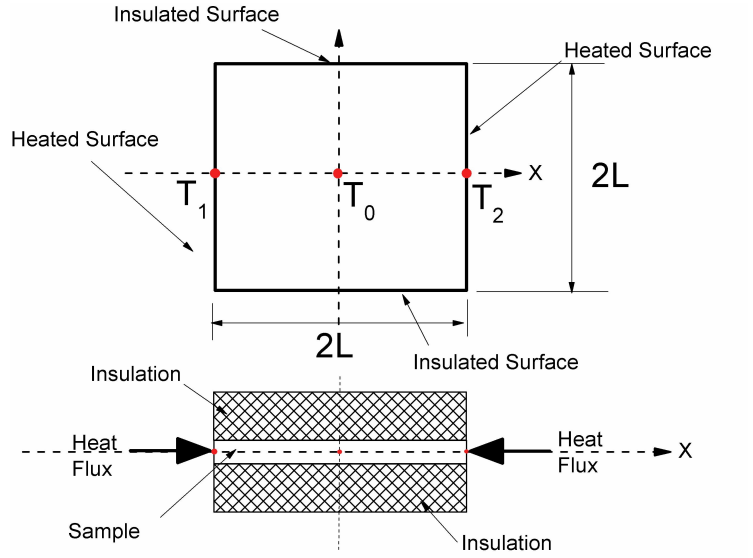

(a)

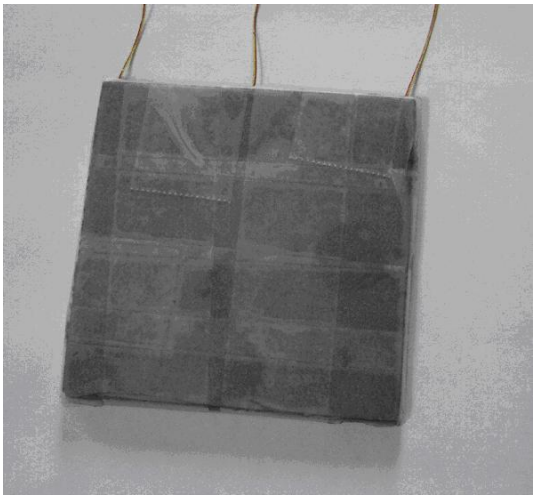

(b)

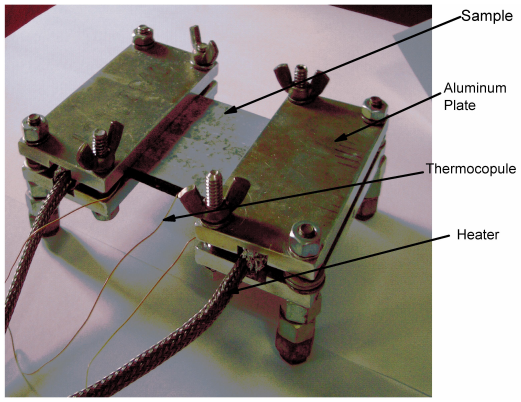

(c)

Figure 3.6: (a) Schematic of the in-plane thermal diffusivity test method - Red dots show placement for thermocouples (Top figure shows the top view of the test apparatus and the bottom figure shows the side view); (b) Sample used for in-plane thermal diffusivity measurements with the thermocouples mounted; (c) Photo of the setup of the in-plane thermal diffusivity test.

Analytical analyses of this method showed that possible errors caused by side heat transfer are in the range of 1-2%. In order to further investigate the the accuracy of this method to measure the thermophysical properties of materials, we measured the thermal conductivity of a standard material (steel 304) having the same geometric shape and size of the investigated material. Discrepancy of our test results of this standard material and the standard reference data was in the range of 2-3%.

3.3.1.2 Data Analysis

In this thesis, the in-plane thermal conductivity was determined as a product of the thermal diffusivity of the carbon paper, specific heat capacity and volume density as follows:

$$k_{\text{eff}}^{\text{in}} = \alpha \rho C_p^{\text{specimen}} \tag{3.13}$$

where α is the thermal diffusivity, ρ is the volume density of the sample and C_p^{specimen} is the specific heat of the specimen. The volume density of all the samples under investigation was measured using the Method of Standard Porosimetry (MSP), which was described earlier in this chapter.

Specific heat of the investigated materials was calculated as an additive function based on the composition of the materials given earlier and the reference data on carbon and Teflon [135, 136]. The specific heat of basic materials is reported as a function of temperature, $T(^{\circ}C)$, for Carbon [135]:

$$C_p^{\text{carbon}} = 1.062 \times 10^{-6} T^3 - 2.983 \times 10^{-3} T^2 + 3.2T + 639.66 \tag{3.14}$$

For Teflon [136]:

$$C_p^{\text{PTFE}} = 4T + 1000 \tag{3.15}$$

where the specific heat is given in $Jkg^{-1}K^{-1}$ and the temperature T is in degrees Celsius.

Using the known composition of the carbon paper material and the specific heat of carbon and PTFE, the specific heat of the carbon paper is found as a volume average as follows:

$$C_p^{\text{specimen}} = wt.\% C_p^{\text{PTFE}} + (1 - wt.\%)\, C_p^{\text{carbon}} \tag{3.16}$$

where $wt.\%$ is the percentage of Teflon in the specimen. Typical results of the specific heat of carbon paper samples treated with Teflon are presented in Figure 3.7.

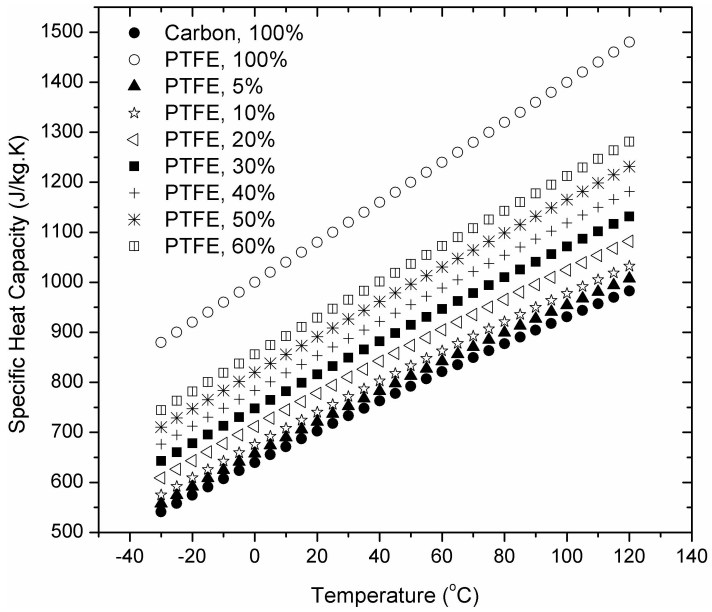

Figure 3.7: Specific heat of specimens calculated using Equation 3.16

3.3.1.3 Experimental Conditions

The experimental conditions of this thesis under which the in-plane thermal diffusivity was measured are summarized as follows:

1. The effect of temperature on the in-plane thermal diffusivity was investigated for the temperature range from -20 to $+120\ ^{\circ}C$ for all the samples under study.

2. The effect of Teflon treatment on the in-plane thermal diffusivity was determined for four different loadings (0, 5, 20 and 50 wt.%). The samples used were manufactured by TORAY carbon (TORAY-TPGH-120) with thickness of 370 (μm)

All measurements were made under atmospheric pressure.

3.3.1.4 Uncertainty Analysis

The thermal conductivity is evaluated using the measured thermal diffusivity, which is a function of the following parameters:

$$\alpha = f\left(\frac{dT}{dt}, \Delta T, L\right) \tag{3.17}$$

where $\frac{dT}{dt} = b$ is the heating rate, ΔT is the temperature difference and L is the length of the sample. Hence, the uncertainty associated with determining the thermal diffusivity depends on these three parameters. However, to calculate the uncertainty of the thermal conductivity measurements, the error in obtaining the specimen density, ρ, should also be taken into account.

The main uncertainty in the experiments comes from the heating rate, $\frac{dT}{dt}$ with a maximum error of 5%. The maximum error associated with the thermocouples is 3%, with the length is 1% and with the density of the sample is 2.5%. Hence, the maximum uncertainty for the thermal conductivity can be calculated from [145]:

$$\frac{\delta k_{\text{eff}}}{k_{\text{eff}}} = \sqrt{\left(\frac{\delta b}{b}\right)^2 + \left(\frac{\delta \Delta T}{\Delta T}\right)^2 + 2\left(\frac{\delta L}{L}\right)^2 + \left(\frac{\delta \rho}{\rho}\right)^2} \tag{3.18}$$

For the measurements of the in-plane thermal conductivity, the maximum uncertainty is estimated to be ±6.4%.

3.3.2 Measurement of the Through-plane Thermal Conductivity

The basic operational principle of this method is the use of a slug that is manufactured from a thermally conductive material, which is capable of withstanding various operational temperatures [147]. The material of choice for the slug must have a thermal conductivity substantially higher than that of the tested material (carbon paper in this thesis). When the outer surface of the test samples are exposed to a heating element, heat will pass through the test material causing the temperature of the slug to rise. The temperature rise through this slug is controlled by three elements, the rate of heat conducted through the slug's surface, its mass and its heat capacity. Hence, the rate in temperature rise of the slug is directly proportional to the heat flux entering it. Under these conditions, the slug becomes a flux-gauging device; hence, the thermal conductivity of the sample can be calculated directly. This technique can be used to measure the thermal conductivity of a wide range of geometries and the design of the slug will be directly influenced by the geometry of the test material. In this study, the tested materials (carbon paper) have a rectangular shape; hence, the slug also is of a rectangular shape. The experimental technique utilized in this thesis for the measurement of the through-plane thermal conductivity along with the experimental conditions and the error associated with this technique are discussed in the next sections.

3.3.2.1 Experimental Technique and Apparatus

In this thesis, the through-plane thermal conductivity of TORAY carbon paper was measured at Integrity Testing Laboratory (ITL) using a thermal capacitance (Slug) calorimeter (ASTM-E2584-07), which is based on Fourier's Law. This method has been used extensively in other studies [135, 141, 142, 146] to measure the thermal conductivity of compressed fiber materials and allows for the measurements of the thermal conductivity to be carried out for a wide range of temperatures. A schematic drawing of the method and the setup used for the measurements of the through-plane thermal conductivity in this thesis are shown in Figure 3.8.

This method is based on the assumption that the heat flow through the carbon paper sample is one-dimensional. In other words, the temperature distribution in the carbon paper sample depends on the spatial coordinate x as shown in Figure 3.8 and time t; that is $T = T(x,t)$. The solution is determined for the case where the temperature of the surfaces of the carbon paper samples exposed to the Aluminum plates is increasing at a constant rate. In this study, we consider a pair of carbon paper specimens, as shown in Figure 3.8, each having a thickness L, with the initial condition that the temperature is constant throughout the thickness of the specimen and the slug, in other words $T(x,0) = T_i$. By symmetry, the mid-plane of the steel slug plate will be an adiabatic boundary, so that we need only consider one specimen and one half of the steel slug plate. Assuming constant properties, the temperature in the specimen must satisfy the one-dimensional Fourier's law of conduction:

$$\frac{\partial^2 T}{\partial x^2} = \frac{1}{\alpha}\frac{\partial T}{\partial t} \tag{3.19}$$

where $\alpha = \dfrac{k}{\rho C}$ is the thermal diffusivity, k is the thermal conductivity of the carbon paper samples, ρ is the density of the carbon paper samples and C is the heat capacity of the carbon paper specimens.

If the rate of heating is maintained constant, say $\dfrac{\partial T}{\partial t} = b$, during the experiment, then the right-hand side of Equation (3.19) will be constant. Equation (3.19) can be integrated with the solution in the form of second order polynomial in x:

$$T(x,t) = \frac{b}{2\alpha}x^2 + d_1 x + d_2 \tag{3.20}$$

where d_1 and d_2 are the constants of integration. Hence, two boundary conditions are required to determine the integration constants. Considering the left sample shown in Figure

3.8(a) without loss of generality, the boundary condition at the left surface of the sample can be written as:

$$\text{At x=0:} T(0,t) = bt + T_i = T_1 \tag{3.21}$$

where b is the heating rate and is constant having the units (K/s) and T_1 is the temperature at $x = 0$ and is also a measured quantity in this thesis research.

To determine the second boundary condition at the right surface of the left sample in Figure 3.8(a), consider energy balance for the left half of the steel slug in the middle of Figure 3.8(a): heat conducted in through the sample carbon paper on the left must equal to the heat absorbed by one half of the steel slug plate. Since the thermal conductivity of the steel slug is much larger than that of the sample carbon paper, the steel slug, having an equivalent Biot number of much less than 0.1, essentially maintains a uniform temperature distribution. Therefore, the energy balance for the steel slug will result into the second boundary condition at the right surface of the sample as:

$$\text{At x=L:} k\frac{\partial T}{\partial x} + Hb = 0 \tag{3.22}$$

where

$$H = \frac{M_{\text{slug}} C_{\text{slug}}}{2A} \tag{3.23}$$

is the thermal capacity of the slug plate per unit surface area $(J/m^2.K)$, M_{slug} is the mass of the slug, C_{slug} is the heat capacity of the slug, A is the cross section area of the slug and is $6cm \times 6cm = 36cm^2$ in this study.

Using the boundary conditions given by Equations (3.21) and (3.22), the constants of integrations can be found and the solution of Equation (3.19) becomes:

$$T(x,t) = \frac{b\rho c}{2k}x^2 - \frac{(Hb + \rho bcL)}{k}x + T_1 \tag{3.24}$$

Using the solution for the temperature distribution across the carbon paper sample and given by Equation (3.24), the temperature difference across the carbon paper sample is then:

$$\Delta T = T(0,t) - T(L,t) = \frac{bL}{k}\left(H + \frac{L\rho C}{2}\right) \tag{3.25}$$

Hence, the thermal conductivity of the carbon paper sample can be found as:

$$k = \frac{bL\left(H + \frac{L\rho C}{2}\right)}{\Delta T} \tag{3.26}$$

using Equation (3.23) for H and factoring out the cross section area, A, Equation (3.26) can be rewritten as:

$$k = \frac{bL\left(M_{\text{slug}}C_{\text{slug}} + M_{\text{sample}}C\right)}{2A\Delta T} \tag{3.27}$$

where $\Delta T = T_1 - T_0$, with T_1 and T_0 are measured values in this study. In this study, the thermal conductivity is evaluated at an average temperature, which is equal to the average of the mean slug temperature and the exterior specimen temperature.

As illustrated in Figure 3.8, the main elements of the system are the measurement cell, moveable furnace, thermocouples connected to the Data Acquisition System (DAQ), power supply, thermal control unit and computer. The moveable furnace is shown in its upper position. When the experiment is running the furnace is lowered to its base. The temperature is increased at a constant rate, which is assured by an automatic thermal control unit. Time-dependent thermal voltage signals are measured by three K-type thermocouples and registered by the DAQ system. In order to obtain measurements of the thermal conductivity at sub zero temperatures, the calorimetric system and samples were cooled in liquid nitrogen before heating.

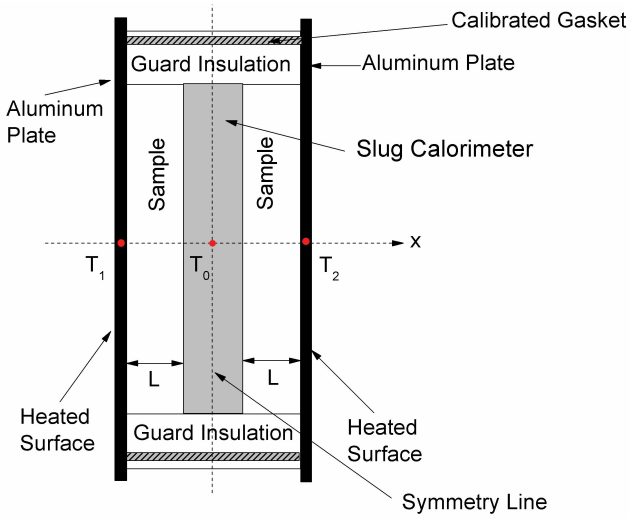

(a)

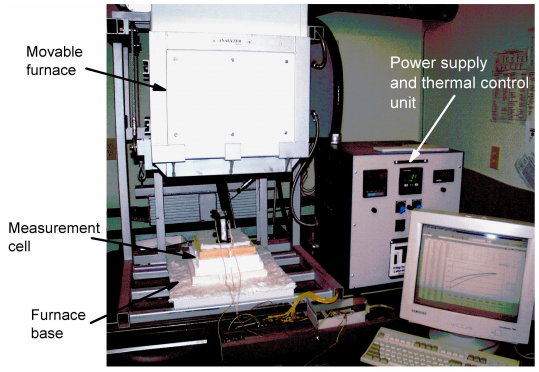

(b)

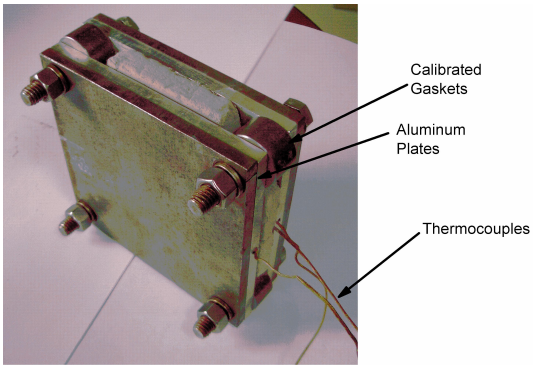

(c)

Figure 3.8: Experimental apparatus for measuring the through-plane thermal conductivity of the carbon paper GDL (a) Schematic of the thermal conductivity test method; (b) Photo of test apparatus; (c) Photo of measurement cell.

3.3.2.2 Experimental Conditions

The experimental conditions encountered in this thesis under which the through-plane thermal diffusivity was measured are summarized as follows:

1. The effect of temperature on the through-plane thermal conductivity was investigated for the temperature range from -20 to $+120$ $^{\circ}C$ for all the samples under study.

2. The effect of Teflon treatment on the through-plane thermal conductivity was determined for two different loadings (0 and 60 wt.%). The samples used were manufactured by TORAY carbon.

3. The effect of deformation on the through-plane thermal conductivity was measured for two different deformation percentages (1% (low) and 16% (high)). The thickness of the samples, d, was ensured by using stainless steel gaskets calibrated with a tolerance of ± 0.01 (mm).

All measurements were made under atmospheric pressure.

3.3.2.3 Uncertainty Analysis

In this thesis, the through-plane thermal conductivity is a function of the following parameters:

$$k_{\text{eff}} = f\left(b, \Delta T, L, A, \rho\right) \tag{3.28}$$

where b is the heat flux, ΔT is the temperature difference, L is the thickness of the sample, A is the cross section area of the sample and ρ is the density of the sample, which was evaluated using the method of standard porosimetry. Hence, the uncertainty associated with determining the thermal conductivity depends on these five parameters. It should be pointed out here that the mass of the carbon paper sample depends on the volume and density of the sample. The main uncertainty in the experiments comes from the heat flux, q with a maximum error of 5%. The maximum error associated with the thermocouples is 3% and with the thickness and area is 1%. The error associated with the density is 2.5%. Hence, the maximum uncertainty for the thermal conductivity can be calculated from [145]:

$$\frac{\delta k_{\text{eff}}}{k_{\text{eff}}} = \sqrt{\left(\frac{\delta b}{b}\right)^2 + \left(\frac{\delta \Delta T}{\Delta T}\right)^2 + 2\left(\frac{\delta L}{L}\right)^2 + \left(\frac{\delta \rho}{\rho}\right)^2 + 2\left(\frac{\delta A}{A}\right)^2} \tag{3.29}$$

For the through-plane thermal conductivity measured in this thesis, the maximum uncertainty is estimated to be $\pm 7\%$.

3.4 Chapter Summary

In this chapter, four experimental apparatus, which are utilized in this thesis, have been discussed. First, the method of standard porosimetry (MSP) is discussed. This method is typically used to characterize the structure of the carbon paper GDL and to measure

the capillary pressure versus the saturation. The second method described is the use of a Loschmidt cell to measure the effective diffusion coefficient of the carbon paper GDL. Finally, two methods based on monotonous heating and used to measure the in-plane and through-plane effective thermal conductivity are described.

Chapter 4

Numerical Formulation

In this thesis, the effective properties of a dry carbon paper diffusion media was determined numerically in both the in-plane and through-plane directions. As shown in Figure 4.1 and detailed in the modeling domain section, a cubic computational domain is used. The modeling domain was constructed with a realistic morphology to represent carbon paper composed of long, straight, cylindrical fibers. To obtain these effective properties, it is necessary to solve for the concentration, temperature and potential distributions in the void and solid regions of the carbon paper. In the next sections, the governing equations, boundary conditions, modeling domains and numerical and mathematical procedure used for determining these properties are discussed in detail.

4.1 Dry GDL Properties

4.1.1 Modeling Domain

The modeling domain constructed for the purpose of this thesis is of a carbon paper GDL with straight, cylindrical fibers that are infinitely long. Two common methods can be used to construct a realistic three-dimensional pore morphology of carbon paper. The first such method is the use of three dimensional volume imaging techniques. This technique relies on the two-dimensional images of the material, which can be generated with the use of non-invasive experimental techniques, such as X-ray and magnetic resonance. The resultant two-dimensional images are then combined to construct the three-dimensional image of the microstructure. This technique can be both expensive and time consuming. The second method involves the use of digitally stochastic models. The pore distribution and pore size of the microstructure are required and are usually obtained using a porosimeter. This

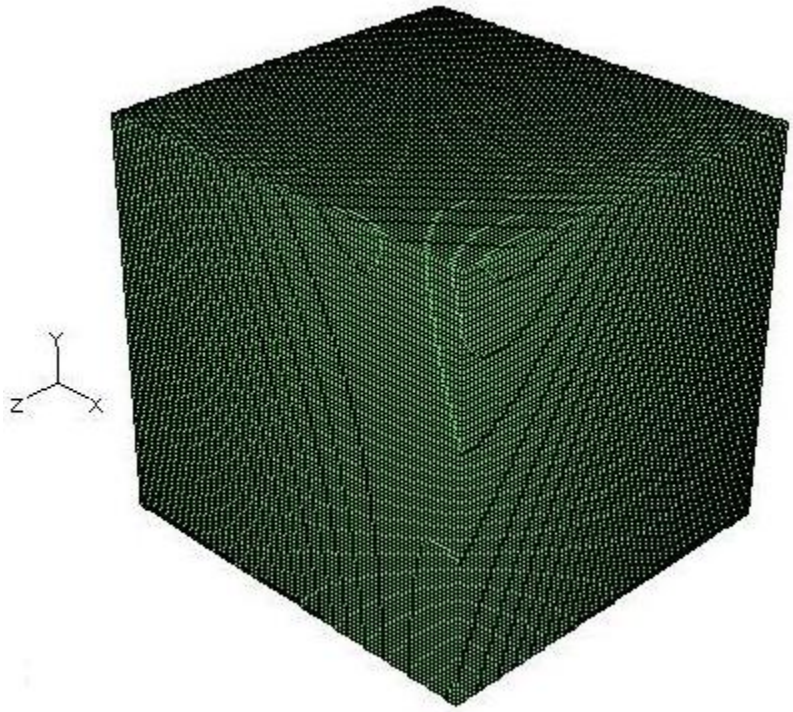

Figure 4.1: Cubic modeling domain.

technique has been employed by many groups [55, 57, 58, 152] and proved successful.

In this thesis, the microstructure of a carbon paper GDL is reconstructed using the stochastic model procedure developed by Schladitz et al. [56]. The method relies on knowing the microstructure of carbon paper using two-dimensional cross sectional images. After acquisition of these images, the model geometry is reconstructed based on stochastic methods by fitting model parameters. The geometric characteristics of the microstructure are determined and the parameters of the model are chosen such that the characteristic properties of carbon paper (porosity, fiber radius and distribution) are presented correctly. Further, other characteristic properties, such as the anisotropy, are also determined. For the purpose of this thesis, to construct the modeling domain the following assumption must be made:

1. The fibers are considered to be cylindrical, with a constant radius and are infinitely long.

2. The fibers are allowed to overlap.

3. According to the fabrication process of carbon fiber, the fiber system is isotropic in the material plane. In this case, the material plane is defined as the xy plane.

4. The effect of the binder is ignored in this model.

With these assumptions, the directional distribution of the geometry can be obtained. Schladitz et al. [56] suggested that a stationary Poisson line process with a one-parametric directional distribution can be used to determine the fiber directions. The centers defined can then be used as the centers of cylindrical fibers. The directional distribution of the fibers is given by its probability density and, if written in polar coordinates, is a function of the altitude θ alone:

$$p(\theta) = \frac{1}{4\pi} \frac{\beta \sin\theta}{(1 + (\beta^2 - 1)\cos\theta)^{3/2}} \tag{4.1}$$

where the parameter β describes the anisotropy of the structure.

Using the stochastic model technique described above, ITWM developed the GeoDict code [153] to construct various porous structures and it is used in this thesis to obtain the modeling domain. A sample mesh of fibers for a carbon paper sample with a 90% porosity is shown in Figure 4.2. The total volume of this sample is $180\mu m \times 180\mu m \times 180\mu m$. The fibers are infinitely long with a circular cross section having a radius of 7 μm. It is clearly seen from Figure 4.2 that the modeling domain is highly anisotropic. As mentioned earlier, the fibers are parallel to the xy-plane. In order to construct the anisotropic structure, the anisotropy parameter, β, in GeoDict is set to 10,000. β is a measure of the distribution of the fibers in the xy plane. An increasing β results in fibers that are parallel to the xy plane.

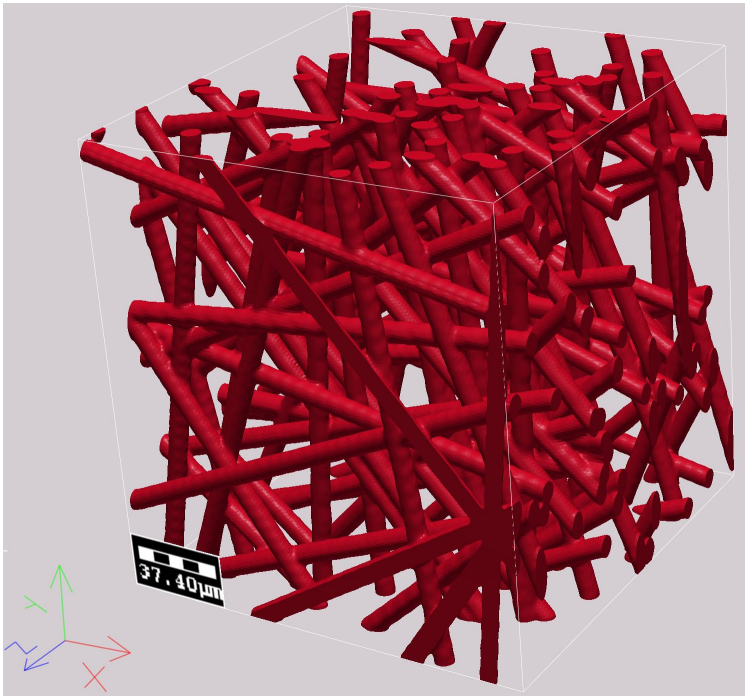

Figure 4.2: Three-dimensional sample mesh for modeling domain - anisotropic carbon paper GDL at 90% porosity with no binder. (This structure is denoted as **True** structure in this thesis)

4.1.1.1 Effect of Structure Anisotropy

In this section, two additional domains are introduced. These domains are used to estimate the effect of anisotropy on the overall transport properties of a dry porous material. The structure that is considered as fibers is given in Figure 4.3(a). This domain is composed of equal amounts of two structures; long cylindrical fibers perpendicular to the xy plane are added to the real structure of the carbon paper GDL. The sample mesh given in this figure has a total porosity of 81%.

The second structure to be considered is a representation of an isotropic porous medium with infinitely long, straight cylindrical fibers as illustrated in Figure 4.3(b). The mesh given in this figure is a sample mesh with a 90% porosity. The total volume of this mesh is $180 \times 180 \times 180$ μm . The fibers are infinitely long with a circular cross section having a radius of 7 μm. In order to obtain this isotropic structure, β was set to equal 1.

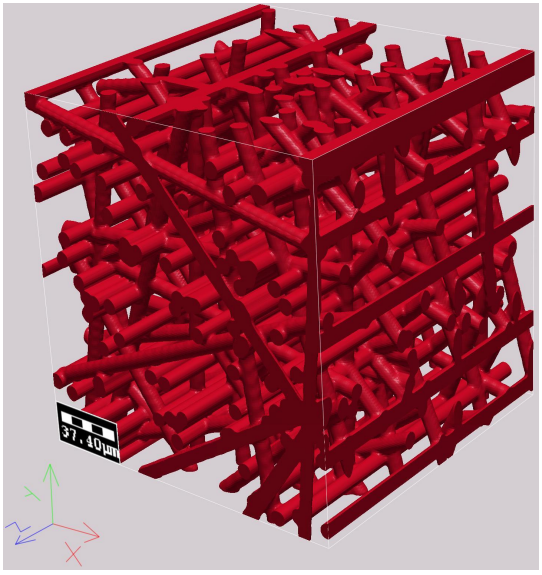

(a)

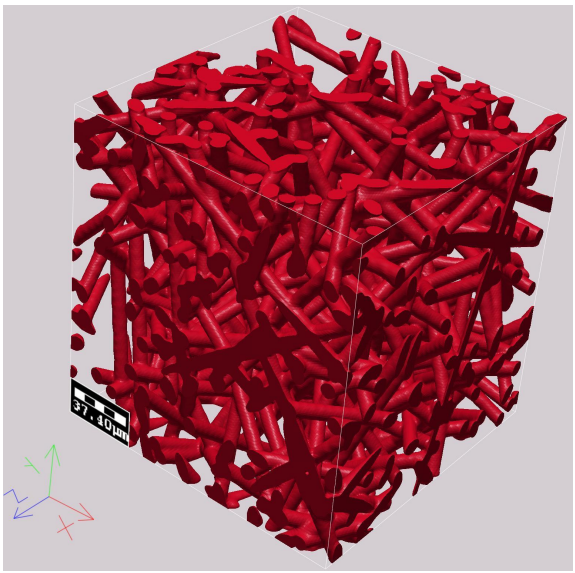

(b)

Figure 4.3: (a) 3-D mesh of anisotropic carbon paper GDL with embedded fibers at 81% porosity. (Denoted as **fibers** in this thesis); (b)3-D mesh of an isotropic carbon paper GDL at 90% porosity with no binder. (Denoted as **isotropic** in this thesis)

4.1.2 Governing Equations

The mathematical problem is solved from a macroscopic level. At this level, continuous and differential quantities can be determined. For the purpose of this thesis, the concentration, temperature, potential and pressure distributions should be simulated. The concentration of the species is solved using the second Fick's law of diffusion in the void region. The temperature distribution in the void and solid regions follows Fourier's law and Ohm's law is used to solve for the potential in the solid region. Since species are not produced nor consumed in the carbon paper GDL, the three laws can be written in the form of a Laplace equation as follows:

$$\nabla.\left(\xi_{\vartheta}\nabla\rho_{\vartheta}\right) = 0 \tag{4.2}$$

where ρ and ξ are the variable and its property, respectively, of the region ϑ (either solid or void). ρ represents either the concentration of species i, C_i, temperature T or the potential ϕ. ξ is either the diffusion coefficient, D, thermal conductivity k or the electrical conductivity σ.

When solving for the concentration gradient in the reconstructed GDL, the Knudsen effect is taken into account when considering Fick's Law of diffusion. In small pores, where Knudsen effects are of interest, the diffusion coefficient is approximated by Bosanquet's formula [151]:

$$D = \left(D_{\text{bulk}}^{-1} + D_{\text{Kn}}^{-1}\right) \tag{4.3}$$

where D_{Kn} is the Knudsen diffusion coefficient and depends on the thermal velocity and the characteristic length of the porous material.

To solve for the pressure gradient in the pore space, the stationary Stokes equation is used as follows:

$$\begin{aligned} \nabla P &= \mu\nabla^2 u \\ \nabla.u &= 0 \end{aligned} \tag{4.4}$$

where u is the velocity of the gas, ∇P is the gradient of the pressure and μ is the dynamic viscosity.

4.1.3 Boundary Conditions

The Laplace equation given by Equation (4.2) is solved to obtain the concentration, temperature and potential distributions. Diffusion of gases occurs in the void region of the

Table 4.1: Boundary conditions.

Boundary	**Through-plane (z-direction)**	**In-plane (x-direction)**
$z = 0$	$\rho_i\,(z = 0) = \rho_{\text{in}}^{z}{}^{\dagger}$	Symmetry boundary condition
$z = 180$	$\rho_i\,(z = 180) = \rho_{\text{out}}^{z}{}^{\ddagger}$	Symmetry boundary condition
$x = 0$	Symmetry boundary condition	$\rho_i\,(x = 0) = \rho_{\text{in}}^{x}{}^{\star}$
$x = 180$	Symmetry boundary condition	$\rho_i\,(x = 180) = \rho_{\text{out}}^{x}{}^{*}$
Other boundaries	Symmetry boundary condition	Symmetry boundary condition

† inlet variable in the z direction.
‡ outlet variable in the z direction.
* inlet variable in the x direction.
* outlet variable in the x direction.

GDL; hence, the concentration distribution is only obtained for the void space. Heat can be conducted through the solid and void regions of the GDL; hence, when obtaining the temperature distribution, Equation (4.2) must be applied to both the solid and void regions. Finally, electrons are conducted via the solid carbon fibers; thus, the potential distribution inside the solid region must be obtained. Equation (4.4) is applied to the void region to solve for the pressure distribution. Concentration, or temperature, or potential or pressure is specified at two parallel surfaces as shown in Table 4.1 to solve for the in-plane and through-plane effective properties.

Internal Boundaries: Since the concentration distribution is solved in the void region, the potential distribution is solved in the solid region and the pressure distribution is solved in the void region, at the internal boundaries (solid/void interface), the symmetry boundary condition is used. However, in the case of the temperature distribution, Equation (4.2) is solved on the whole cubic domain (i.e. for the solid and void regions) with the coefficient k_ϑ as a piecewise constant, which has one value for the solid and another for the air. Hence, temperature and heat flux at the internal boundary, or at the interface between the solid carbon and air is continuous. This can be defined mathematically as follows:

$$T_{\text{air}} = T_{\text{fiber}} \tag{4.5}$$

$$-k_{\text{air}}\nabla T_{\text{air}} = -k_{\text{fiber}}\nabla T_{\text{fiber}} \tag{4.6}$$

External Boundaries: The external boundaries were used to define a gradient. For instance, for the purpose of solving the temperature distribution, Equation (4.2) is applied to the solid and void regions and solved in both the in-plane and through-plane directions. The

temperature is specified at two external surfaces and the symmetry boundary condition is used at the other four surfaces as shown in Figure 4.1. For example, for the determination of the in-plane ETC, or the x-direction in Figure 4.1, the front and back surfaces are specified with known temperatures while the rest of the surfaces (top, bottom, left and right) are considered insulated. It might be mentioned here that the specified temperature is the same for both the solid and void regions of the interface.

4.1.4 Determination of the Effective Properties

In the physical system considered in this research, there are no chemical reactions through which the species can be generated nor consumed; thus, the source term is equal to zero in Equation (4.2). With the source term being equal to zero, Equation (4.2) yields a unique solution for the boundary conditions given in Table 4.1. Using the solution of Equation (4.2), the average flux can be evaluated as:

$$j = \frac{1}{A} \int_A \left(-\xi_\vartheta \vec{n}.\nabla \rho_\vartheta\right) dA \tag{4.7}$$

where j is the average flux over a cross section that is normal to the flux and A is the surface area over which the flux is evaluated.

Once j is obtained, the effective property of the porous domain can be found. Prior to solving for the effective property, it is important to ensure that the solution has converged properly. j must be equal at different cross-sections. The value of j was evaluated at the inlet, outlet and mid section. Further, a residual of 10^{-8} was used as the convergence criteria. The effective property can then be calculated as follows:

$$\xi_{\text{eff}} = \frac{j}{\frac{\rho_{\text{in}} - \rho_{\text{out}}}{t}} \tag{4.8}$$

where t is the length in the gradient direction.

In order to solve for the permeability of the gas diffusion layer, Equation (4.4) is used to solve for the pressure distribution. With the boundary conditions listed earlier, this equation yields a unique solution. Upon solving Equation (4.4), the total discharge, Q, is evaluated as an integral average over the surface area in the direction of the pressure drop and the intrinsic permeability of the layer can be found as follows:

$$K = \frac{\mu t Q}{\Delta P} \tag{4.9}$$

where K is the intrinsic permeability in m^2 and Q is the total discharge in m/s.

4.1.5 Numerical Procedure

GeoDict was used to generate the mesh of the reconstructed carbon paper GDL. The generated meshes were imported into the commercial CFD solver Fluent (6.3.26). This package is based on a finite volume method. Once the mesh was imported into Fluent, Equation (4.2) was solved in the void and solid regions for the concentration, temperature and potential distributions. Due to the anisotropic nature of the domains under consideration, the effective properties must be found for three directions y, x and z. A user-defined-scalar discretized using a second-order finite volume approach with double precision was used to solve the governing equation (Equation (4.2)).

4.1.6 Representative Elementary Volume (REV)

Using the effective medium approximation, the heterogeneous properties (density, diffusion coefficient, conductivities, etc.) are often replaced with a hypothetical homogenous property. The porous structure is regarded as a continuum and partial differential equations are used to solve for the properties. Due to the complexity of the porous structures and their dimensions, the numerical problem can be computationally expensive; hence, a representative volume is often used. The concept of representative elementary volume (REV) is used to identify the smallest volume over which a measurement can be made yielding a value representative of the whole heterogeneous system [154]. To determine this volume, the effect of varying the length scales on the effective property is evaluated. The fluctuations in the value of the effective property is minimized at the REV and a representative amount of heterogeneity can be confidently averaged. At this volume, the macroscopic property is relatively insensitive to small changes in volume or location [155]. REV is often used to numerically estimate the properties of sand rocks and soil. The volumes under consideration are usually very large; hence, making it very numerically expensive to model the actual dimensions of the system. The principles of the technique are employed to understand the effect of varying the dimensions of the carbon paper GDL volume on the in-plane and through-plane effective properties.

The effective properties evaluated in the through-plane and in-plane directions and a three-dimensional modeling domain is used. Hence, the length scales of the x, y and z directions are varied. In order to obtain the REV, the coefficient of variation (CV) is used. CV is used as an estimator of the variability of the effective property [156]. The coefficient

of variation is defined as the ratio of the standard deviation and the arithmetic average as given below:

$$CV = \frac{\sigma}{\mu} \tag{4.10}$$

where σ is the standard deviation and μ is the arithmetic average. The coefficient of variation must be corrected if the sample size is less than or equal to 10. The common correction factor used is $\left[1 + \frac{1}{4\,(N-1)}\right]$ [157]. Corbett and Jensen [158] explained that heterogeneity is dependent on the coefficient of variation as follows:

$$\begin{aligned} 0.0 < CV < 0.5 \quad & \text{homogeneous} \\ 0.5 < CV < 1.0 \quad & \text{heterogeneous} \\ CV > 1.0 \quad & \text{Very heterogeneous} \end{aligned} \tag{4.11}$$

The coefficient of variation for the various porous structures discussed earlier was evaluated for a thickness interval of 100-400 μm. This range was chosen since the thickness of carbon paper varies from 110-370 μm [91]. In theory, the thickness of the structure should not affect the effective properties. However, in practice, the thickness of the structure may affect the result of the calculations. If the size of the model is too small, the results may systematically differ from those for larger structures. In other words, due to the reconstruction of the solid matrix, variations can be encountered. This variation has been observed experimentally by Ramousse et al. [65]. The measured through-plane effective thermal conductivity for Quintech carbon paper varied with thickness from 0.36 to 0.33 $W/K.m$ for 190 μm and 280 μm thick GDL, respectively. Using 7 volumes, the coefficient of variation was determined for various porosity values and shown in Figure 4.4. The 7 volumes used in this case vary from $100 \times 100 \times 100$ μm to $400 \times 400 \times 400$ μm with a 50 μm interval. It is interesting to note here that the variation of the CV in the through-plane direction is small for small porosity values. When constructing the carbon paper structure for high porosity values, discontinuities in the fiber distribution are more likely to occur. Nonetheless, it is clear that the coefficient of variation lies in the homogeneous range as suggested by Equation (4.11).

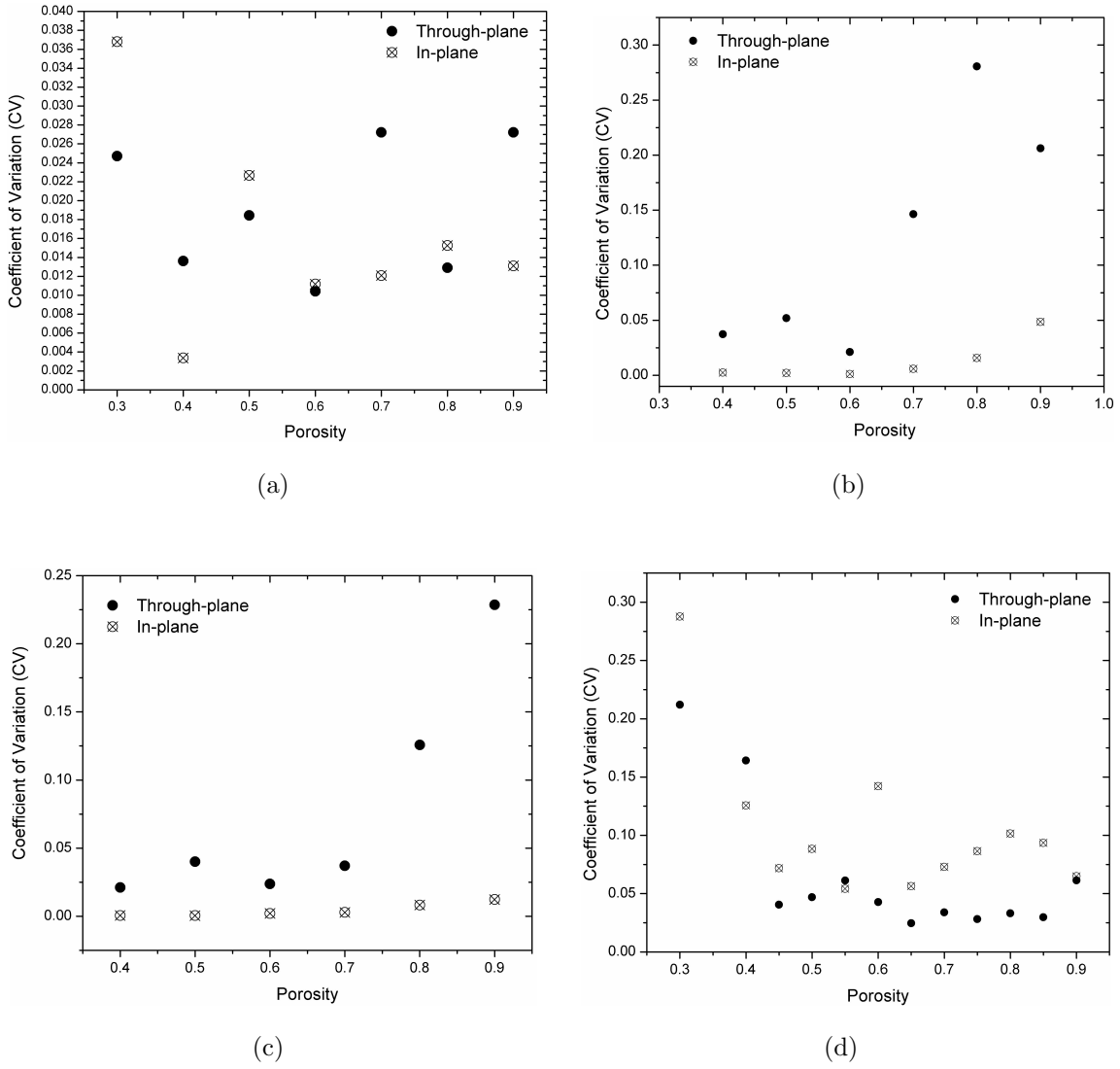

Figure 4.4: The coefficient of variation for the in-plane and through-plane directions for (a) the diffusion coefficient; (b) the thermal conductivity; (c) the electrical conductivity; (d) the intrinsic permeability

In summary, the coefficient of variation is evaluated for each porosity value in order to check the conditions of Equation (4.11). However, examining Figure 4.4, a trend is noticed. It is seen that the coefficient of variation is highly dependent on the porosity value and is especially highlighted in the through-plane direction. The CV decreases with the decrease in the porosity value. Since discontinuities in the fiber distribution are more probable to occur when constructing a highly porous medium, the variation in the effective property is more likely to occur.

4.2 Wet GDL Properties

4.2.1 Modeling Domain

The modeling domain used to simulate the properties of the wet GDL is the same as that used for the dry condition discussed earlier and given in Figure 4.2. For more details refer to section 4.1.1.

4.2.2 Two-phase Simulation

The full morphology (FM) model is used to simulate the presence of liquid water in the carbon paper GDL. This method relies on simulating the presence of liquid water via the determination of the quasi-static primary drainage curve of the wetting phase saturation and its relationship with the capillary pressure, $s_w(P_c)$. This approach can be summarized as having 5 main steps as follows:

1. The initial state of the carbon paper diffusion media is assumed to be entirely filled with the wetting phase (i.e. gas phase in this thesis) and the capillary pressure is zero. At one end, the diffusion medium is connected to a non-wetting phase reservoir while at the opposite end it is connected to the wetting phase reservoir.

2. The pore space, X, is eroded by spheres with increasing radius, r, starting with the smallest radius, which is $r = 1$ (μm) in this thesis. The erosion is defined as:

$$\epsilon_{B_r}(X) = \{x : B_{x,r} \subseteq X\} \tag{4.12}$$

   where $B_{x,r}$ is the structuring element centered at point x. The radius, r, is related to the capillary pressure according to the Young-Laplace equation:

$$P_c = \frac{2\sigma \cos\theta_c}{r} \tag{4.13}$$

   where σ is the surface tension between the non-wetting and wetting phases, θ_c is the contact angle between the wetting phase and the solid. Since the simulation is built under the quasi-state two phase distribution, the contact angle in Equation (4.13) refers to the static contact angle and is merely a numerical parameter in the evaluation of the capillary pressure. It does not influence the shape of the water droplet. The water droplet takes on a spherical shape. Hence, the selection of an appropriate contact angle is key in quantitatively evaluation the capillary pressure-saturation relationship.

There is much debate over the quantitative value of the contact angle and much measurements are found in the published literature. Benziger et al. [159] reported an advancing/receding contact angles of 115°/30° for untreated TORAY carbon paper. In case the paper was treated with PTFE, the contact angle was measured to be 170° for the advancing water and 120° for receding water despite of the amount of PTFE added to the paper. Gostick et al. [114] measured the observed and effective contact angles on untreated TORAY carbon paper to be 146° and 112°, respectively. In this thesis, the contact angle for the untreated carbon paper was taken to be 130°.

In order to define the pore radius in this case, the pore morphology uses the morphological opening as given below:

$$\mathcal{O}_r(X) = \bigcup_{B_{r,x}} \subseteq X, x \in X \tag{4.14}$$

where X represents the pore space and $B_{r,x}$ is a sphere with radius r and center point x. Here, $\mathcal{O}_r$ is the part of the pore space in which the structuring element B_r fits. Hence, $\mathcal{O}_r$ is defined to be the space of pores with radius $\acute{r} \geq r$. The non-wetting phase saturation can then be written as a function of the capillary pressure as follows:

$$s_{nw}(P_c) = \frac{\left|\mathcal{O}_{2\sigma\cos\theta/P_c}(X)\right|}{|X|} \tag{4.15}$$

The above equation is built on the assumption that the interfaces between the wetting and non-wetting phases are of spherical shape or at least can approximated by a superposition of spheres. Further, the wetting and non-wetting phases are distributed freely in this model, which can be seen as an equilibrium state reached by repeated drainage and imbibition of the wetting phase.

3. At any given capillary pressure, the pores are filled with the non-wetting phase only if the erosion of the pore space has a continuous connection from the non-wetting reservoir.

4. The phase saturation of the non-wetting and wetting phases related to a given capillary pressure is determined under the assumption that the eroded set is dilated using the same structuring element as for erosion:

$$\mathcal{D}_{B_r}\left[\epsilon_{B_r}(X)\right] = \left\{x : B_{x,r} \bigcap \epsilon_{B_r}(X) \neq \emptyset\right\} \tag{4.16}$$

5. Repeat from Step 2 for the next pressure using the next larger structuring element.

In summary, the method described above relies on specifying the radius of the spherical droplet. This radius is used to calculate the capillary pressure, the degree of erosion of the pore space and in turn the saturation of the non-wetting fluid.

4.2.3 Thermal Conductivity

Transfer of heat in the GDL is governed by heat conduction as follows:

$$\nabla \cdot (k \nabla T) = 0 \tag{4.17}$$

where k is the local (isotropic) thermal conductivity and is dependent on the position in the computational domain. Hence, computationally, the thermal conductivity used for any given grid cell is directionally-independent. The effective thermal conductivity of the layer is dependent on the direction due to the geometrical anisotropy of the GDL and is related to the heat flux as given by Fourier's law of conductivity:

$$j = -k_{\text{eff}} \nabla T \tag{4.18}$$

where j is the heat flux and ∇T is the temperature gradient. The tensor k_{eff} is determined following the homogenization theory [160] by solving the three auxiliary problems in the domain corresponding to three space directions (x, y and z) $\vec{e_1}$, $\vec{e_2}$ and $\vec{e_3}$:

$$\nabla \cdot \left(k\left(x\right)\left(\nabla T_l + \vec{e_l}\right)\right) = 0 \text{ in } \Omega,\ l \in 1,2,3 \tag{4.19}$$

with periodic boundary values:

$$T_l\left(x + id_1\vec{e_1} + jd_2\vec{e_2} + kd3\vec{e_3}\right) = T_l\left(x\right)\ \ \forall i,j,k \in \mathbb{Z} \tag{4.20}$$

with the three solutions for T_1, T_2 and T_3 the components of the the coefficient tensor k_{eff} can be found by integration:

$$k_{\text{eff}}^{ij} = \frac{1}{d_1 d_2 d_3} \int_{\Omega} \left(\vec{e_i}, k\left(x\right)\left(\nabla T_j + \vec{e_j}\right)\right) dx,\ \ i,j \in \{1,2,3\} \tag{4.21}$$

which is symmetric by construction [160]. To solve equations (4.20)-(4.21), the EJ-Heat solver implemented in GeoDict [153] and developed by Wiegmann and Zemitis [161] was used.

In the presence of liquid water, the local thermal conductivity of three species should be defined. These species are the solid fibers, liquid water and the gas phase. In this thesis, the thermal conductivity of the solid fibers, liquid water and gas is taken to be 140 ($W/K.m$), 0.6 ($W/K.m$) and 0.026 ($W/K.m$), respectively.

4.2.4 Diffusion Coefficient

In the pore space, the diffusion is governed by:

$$\nabla \cdot (D \nabla C) = 0 \tag{4.22}$$

where C denotes the concentration and D is the directionally independent diffusion coefficient of the gas in the pore space. In the presence of liquid water, Equation (4.22) is solved in the space occupied by the wetting (i.e. gas) phase for each capillary pressure value, where water and fibers are treated alike. In other words, the water is treated as immobile and impassable for the gas particles and Neumann boundary condition is applied on both gas-water and gas-solid interfaces. To solve for the concentration distribution in the gas pores, concentrations on the boundaries in the direction of the gradient and boundary conditions in the two perpendicular directions are used. The diffusivity tensor, D_{eff}, averaged over the domain fulfills Fick's first law:

$$j = -D_{\text{eff}} \nabla C \tag{4.23}$$

where ∇C denotes the concentration gradient and j is the concentration flux. As before, GeoDict [153] was used to solve three auxiliary boundary value problems to obtain all D_{eff}^{ij}. The method for solving Equation (4.22) is described in detail in [161, 162].

4.2.5 Relative Permeability

In case of a partly saturated porous medium, the permeability is dependent on the saturation of the medium; hence, the flow is governed by:

$$\vec{u} = -\frac{1}{\mu} \kappa(s) \nabla P \tag{4.24}$$

where $\vec{u}$ denotes the average superficial flow velocity, μ is the viscosity, P is the pressure and $\kappa(s)$ is a saturation dependent permeability. If the pressure gradient is parallel to the i^{th}

axis, Darcy's law reduces to the scalar equations:

$$\vec{u_j} = -\frac{\kappa_{ij}(s)}{\mu L}\delta P,\ j = 1, 2, 3 \tag{4.25}$$

where δP is the pressure drop along the i^{th} axis and L is the length of the sample in the i-direction. To determine the coefficient $\kappa_{ij}(s)$ it is thus sufficient to determine the average flow velocity for a given pressure drop. To determine the whole matrix, this has to be done for all three space directions. The average flow velocity is found by solving the governing flow equation in the pore space, namely the stationary Stokes equation:

$$-\mu\Delta u + \nabla P = 0,\ \nabla u = 0 \tag{4.26}$$

where the pressure drop along the i^{th} axis is a boundary condition. Periodic boundary conditions are used in directions perpendicular to the pressure drop. To obtain the velocity, u, the FFF-Stokes solver of Wiegmann and Zemitis [161] was used.

4.3 Chapter Summary

In this chapter, the numerical method used to estimate the transport coefficients of the porous carbon paper GDL was described. The pore morphology of the carbon paper GDL was reconstructed based on a digitally stochastic model. In this thesis, the liquid water distribution is found using the full morphology model and is treated as an immobile entity (i.e. it is treated as a structuring element). The numerical model is used to estimate the intrinsic and relative values of the permeability, diffusion coefficient, thermal conductivity and electrical conductivity as well as the capillary pressure.

Chapter 5

Results and Discussion - Experimental

In order to validate the numerical results of this thesis, it is also necessary to experimentally measure the effective transport coefficients and also understand the structure of the porous medium under investigation. In this chapter, the method of standard porosimetry described earlier in Chapter 3 is used to characterize the structure of the carbon paper gas diffusion layer. The effect of Teflon treatment on the overall porosity, the pore distribution, the surface area occupied by the pore and the capillary pressure is measured and examined. Further, using the Loschmidt cell apparatus, the measurements of the through-plane effective diffusion coefficient are put forward. In this chapter, the effects of temperature and Teflon treatment on the effective diffusion coefficient are investigated. This investigation gives the reader a clear understanding of the importance of the numerical results of this thesis. A comparison between the experimental results of this thesis and the available theoretical approximations of the effective diffusion coefficient shows the need for more accurate correlations. Finally, the experimental results of the in-plane and through-plane effective thermal conductivity are also discussed. In this thesis, the effective thermal conductivity was measured for a wide range of temperature; hence, in this chapter, the effect of phase transformation on the effective thermal conductivity is analyzed.

The experimental measurements of this thesis were all done using TORAY-TPGH carbon paper. The Teflon treatment is applied to the material via the dipping process and its drying process is slow to ensure a uniform distribution of the PTFE material. Some of the results presented in this chapter are based on the journal articles [163, 164].

5.1 Structure Analysis

The investigated materials are TORAY-TPGH 120 carbon paper with various degrees of PTFE loadings (0, 5, 20 and 50 wt.%) and a thickness of 370 (μm). The Method of Standard Porosimetry (MSP) was used in this thesis to measure the porosity and volume density of the samples under investigation as well as to measure the pore size distribution of the sample and the capillary pressure versus wetting and non-wetting phase saturation. Octane was used as the wetting fluid in this thesis. As mentioned earlier, octane has a contact angle of 0°, hence it can totally wet the carbon paper sample. As it is a very strong wetting fluid, the porosity given in this thesis is the total porosity and is the sum of the hydrophobic and hydrophilic pores. The test results are given in Table 5.1.

Table 5.1: Total porosity and volume density of samples

Sample	**Teflon by Weight**	**Volume Density** (g/cm^3)	**Porosity**
1	0%	0.36±0.01	78%±2.0%
2	5%	0.49±0.01	76%±2.0%
3	20%	0.60±0.02	70%±1.7%
4	50%	0.89±0.02	57%±1.4%

It is also interesting to investigate the effect of PTFE loading on the overall pore distribution. For this investigation, the effect of four Teflon loadings (0, 5, 20 and 50 wt.%) on the pore volume and the overall surface area occupied by the pores was plotted as in Figures 5.1 and 5.2, respectively. From Figure 5.1, it can be seen that the overall pore volume of the carbon paper sample decreases with the increase in the Teflon treatment. Further, at a pore radius $r \leq 3000$ nm, the effect of Teflon on the overall pore volume is minimal. This implies that Teflon cannot penetrate pores with a radius lower than 3 μm. At $3000 \leq r \leq 5500$ nm, a transition region is also observed. As it can be seen, this region is independent of the Teflon loading, in other words, the overall trend is the same for all loadings. Finally, the pore volume reaches a plateau that is linear with the PTFE loading. The value reached for the 0, 5, 20 and 50 wt.% samples is 1.8, 1.7, 1.3 and 0.70, respectively. A similar trend is also observed for the overall surface area of the pores as given in Figure 5.2. The total surface area of the pores decreases with the increase in Teflon treatment.

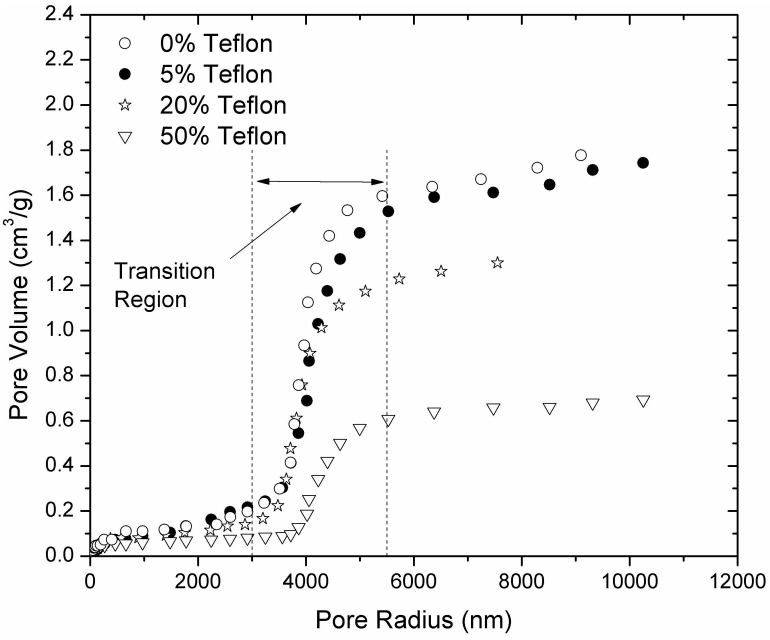

Figure 5.1: Effect of Teflon loading on the pore volume.

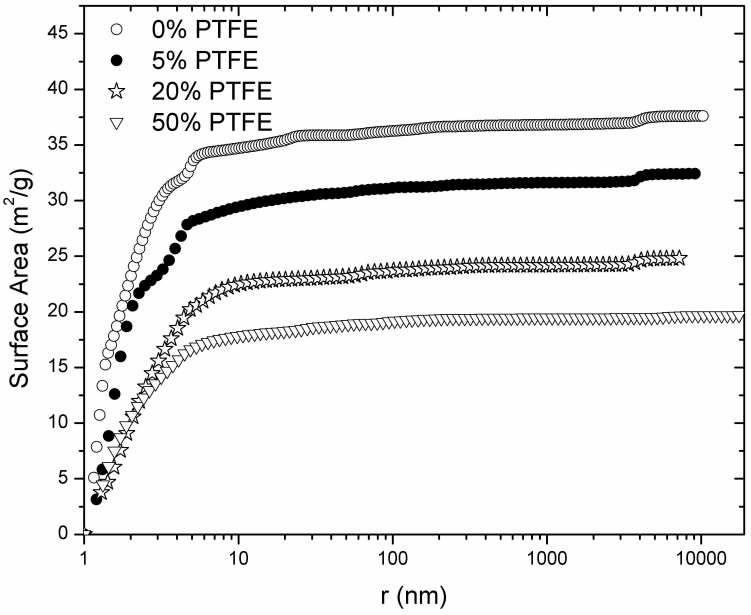

Figure 5.2: Effect of Teflon loading on the overall surface area occupied by the pores.

5.2 Measurement of the Capillary Pressure

Using the method of standard porosimetry the effect of PTFE on the capillary pressure was also examined. Figure 5.3 illustrates the relationship between the capillary pressure

of an octane-air system and the wetting phase (octane) saturation. The capillary pressure decreases once Teflon is introduced to the system. Further addition of Teflon does not result in drastic changes to the capillary pressure. This implies that the contact angle between the non-wetting phase and the solid phase is no longer affected by amount of PTFE. This finding is in agreement with that by Benziger et al. [159]. As mentioned earlier, they found that the receding and advancing contact angle between liquid water and the solid did not change despite the amount of PTFE added to the paper. Further, it is interesting to note the behavior of the capillary pressure versus the saturation of the octane for saturation levels higher than 0.9 and lower than 0.1 As it can be seen, in this range the capillary pressure is almost the same for all Teflon values.

Using the results of the capillary pressure of the octane-air system, Equation (3.1) can be used to obtain the capillary pressure of water-air system in terms of the non-wetting phase (liquid water) saturation. In order to do this transformation, the contact angle between the liquid water and solid is needed. In the study by Fairweather et al. [119], they measured the contact angle of Teflonated TORAY-TPGH-90 between 130-133° regardless of loading. Their study was conducted on four PTFE loadings, 5, 10, 20 and 40 wt.%. Using a contact angle of 130° and the transformation shown in Equation (3.1), the capillary pressure of an air-water system versus liquid water saturation was obtained for various PTFE loadings as shown in Figure 5.4.

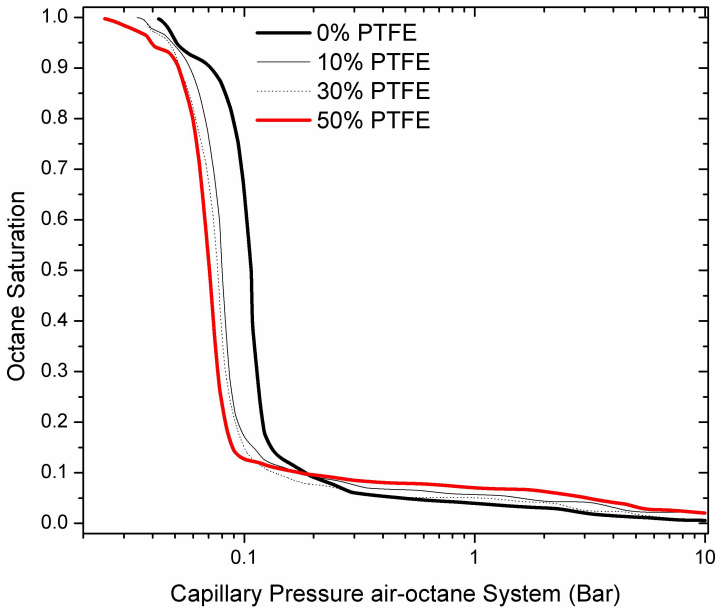

Figure 5.3: Experimental measurements of the capillary pressure of an air-octane system and its dependence on the wetting phase saturation.

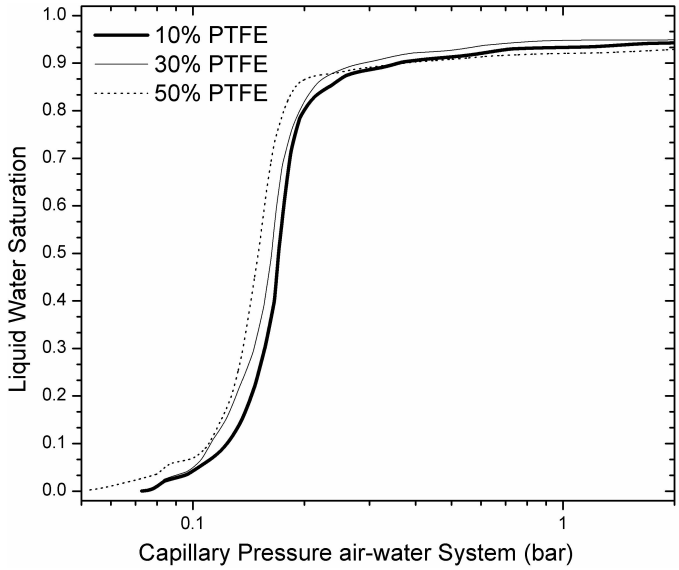

Figure 5.4: Experimental measurements of the capillary pressure of an air-water system and its dependence on the liquid water saturation - capillary pressure data were extracted from those for an air-octane system using a contact angle of 130°

5.3 Diffusion Coefficient

5.3.1 Effect of Temperature

The effect of temperature on the effective diffusion coefficient of gases in carbon paper is of great importance since PEM fuel cells can operate on temperatures in the range of 25-120 °C. To study this effect, the effective diffusion coefficient of oxygen in nitrogen is measured for different temperatures. The carbon paper sample used is TORAY carbon paper (TPGH-120) with a thickness of 370 μm, a 0% PTFE content (no wet-proofing) and a porosity of 76%. The mixture had 0% relative humidity and was fed at a pressure of 1 atm. The measurements of the effective diffusion coefficient made are given in Figure 5.5. In this figure, the bulk diffusion coefficient at different temperatures (also measured in this study) is also plotted.

The bulk diffusion coefficient is measured at the beginning of the test to ensure that the system is functioning properly. It is evident that due to the structure of the carbon paper, the diffusion coefficient decreases considerably. The measured bulk diffusion coefficient agrees

with the theory developed by Fuller et al. [148], which evaluates D_{AB} as:

$$D_{\mathrm{AB}} = \frac{1.00 \times 10^{-3} T^{1.75} \left(1/M_A + 1/M_B\right)^{0.5}}{P\left[\left(\sum \upsilon\right)_A^{1/3} + \left(\sum \upsilon\right)_B^{1/3}\right]} \tag{5.1}$$

where D_{AB} is the mass diffusivity of gas species A through B in cm^2/s, T is the absolute temperature in K, M_A and M_B are the molecular weights of A and B, respectively in g/mol, P is the absolute pressure in atm, with the atomic and structural diffusion volume increment υ is summed over the atoms, group of atoms, and structural features of each diffusion species.

Studying the trend of variations illustrated in Figure 5.5, it is interesting to note the difference in the slope of both lines representing the bulk and effective diffusion coefficients measured. It is seen that the effect of temperature on the bulk diffusion coefficient is different from that on the effective diffusion coefficient, or the effective diffusion coefficient seems to increase with temperature more slowly than the bulk temperature. This suggests that the effective diffusion coefficient is not dependent on the temperature of the gas only. To better understand the extent to which temperature affects the overall diffusion process in the carbon paper GDL, the diffusibility (Q) should be investigated. As mentioned earlier, Q is defined as the ratio of the effective to the bulk diffusion coefficient. The measured diffusibility for different temperatures is given in Table 5.2.

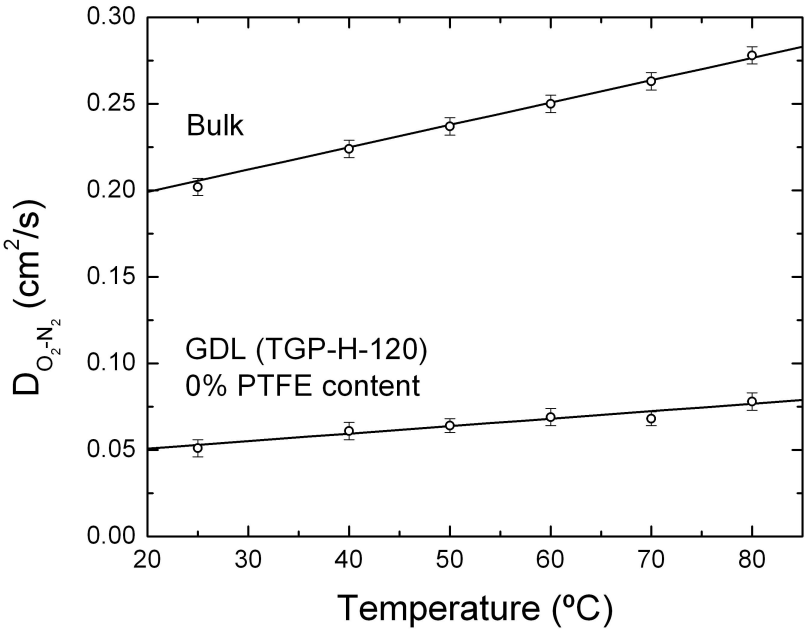

Figure 5.5: Effect of temperature on the bulk and effective diffusion coefficients of oxygen-nitrogen mixture - Error bars are shown in the figure

Table 5.2: Effect of temperature on the diffusibility

Temperature ($^{\circ}C$)	**Diffusibility** ($Q = \frac{D_{\text{eff}}}{D_{\text{bulk}}}$)
25	0.252
40	0.272
50	0.270
60	0.276
70	0.258
80	0.281

From Table 5.2, it is seen that the temperature has very little effect on the overall diffusibility. Hence, the structure of the carbon paper is the determinant of the magnitude of diffusibility. This finding is consistent with that found by [149]. In their work, they measured the effect of operating pressure on the diffusibility in carbon paper and found that the operating pressure does not affect the overall diffusibility. Therefore, the temperature dependence of the effective diffusion coefficient originates from the corresponding dependence of the bulk diffusion coefficient on temperature. The experimental results of this thesis are compared against the available theoretical models discussed earlier in Chapter 2 as given in Table 5.3.

The diffusibility is calculated under the dry condition (i.e. the liquid water saturation in the carbon paper GDL is zero) and using a porosity of 76%. Comparing the model predicted diffusibility to that measured, it is clear that the existing models available in literature overpredict the effective diffusion coefficient significantly, by as much as a factor of 2.5. Hence, the use of these models for the purpose of PEM fuel cell modeling/simulation will result in considerably underestimating the mass transport limitations, especially at high current densities. The difference between the model predicted and measured values is due to the difference in the geometry involved, as pointed out earlier, all the available models in literature for the effective diffusion coefficient were developed based on spherical particles that form the porous media. In order to account for the geometry effects, some models, such as the Bruggeman Approximation [36], suggest the use of the tortuosity factor, and others, such as Das et al. [48], propose the use of a shape factor. In order to predict either the tortuosity or shape factors, which properly describe the geometry of the carbon paper GDL, experimental data for a different porosity values are needed.

Table 5.3: Diffusibility for TORAY TPGH-120 as predicted by the existing effective diffusion coefficient models available in literature for $\epsilon = 0.76$ and measured in this thesis

Model	**Expression** $(Q = \frac{D_{\text{eff}}}{D_{\text{bulk}}})$	**Diffusibility**
Bruggeman [36]	$\frac{D_{\text{eff}}}{D_{\text{bulk}}} = \epsilon^{1.5}$	0.650
Neale and Nader [40]	$\frac{D_{\text{eff}}}{D_{\text{bulk}}} = \frac{2\epsilon}{3-\epsilon}$	0.667
Tomadakis and Sotirchos [42]	$\frac{D_{\text{eff}}}{D_{\text{bulk}}} = \epsilon\left(\frac{\epsilon-0.037}{1-0.037}\right)^{0.661}$	0.615
Nam and Kaviany [47]	$\frac{D_{\text{eff}}}{D_{\text{bulk}}} = \epsilon\left(\frac{\epsilon-0.11}{1-0.11}\right)^{0.785}$	0.579
Das et al. [48]	$\frac{D_{\text{eff}}}{D_{\text{bulk}}} = 1 - \frac{3(1-\epsilon)}{3-\epsilon}$	0.667
Experimental measurements of thesis		0.27

5.3.2 Effect of Teflon Treatment

The addition of Teflon could also change the diffusion process of gases in the carbon paper GDL. In order to understand this change, the effective diffusion coefficient of an oxygen-water vapor in nitrogen-water vapor was determined for the range of 0-40 wt.% Teflon treatment, and the results are reported in Figure 5.6. The bulk diffusion coefficient of oxygen-water vapor in nitrogen-water vapor is 0.322 cm^2/s and it was also determined by Astrath et al. [150]. The diffusibility decreases as the Teflon treatment percentage is increased. It is believed that this increase is due to the change in porosity.The porosity of the carbon paper GDL is decreased since more solid material, being Teflon, is added; thus, decreasing the volume of pore available for diffusion.

5.4 Thermal Conductivity - In-plane

Using the method of monotonous heating described earlier in Section 3.3.1 was used in order to measure the in-plane thermal conductivity of TORAY carbon paper for a wide range of temperature and various Teflon loadings. In this part of the thesis, the experimental measurements are discussed in detail. Further, the importance of such measurements for understanding heat transfer in the GDL is highlighted.

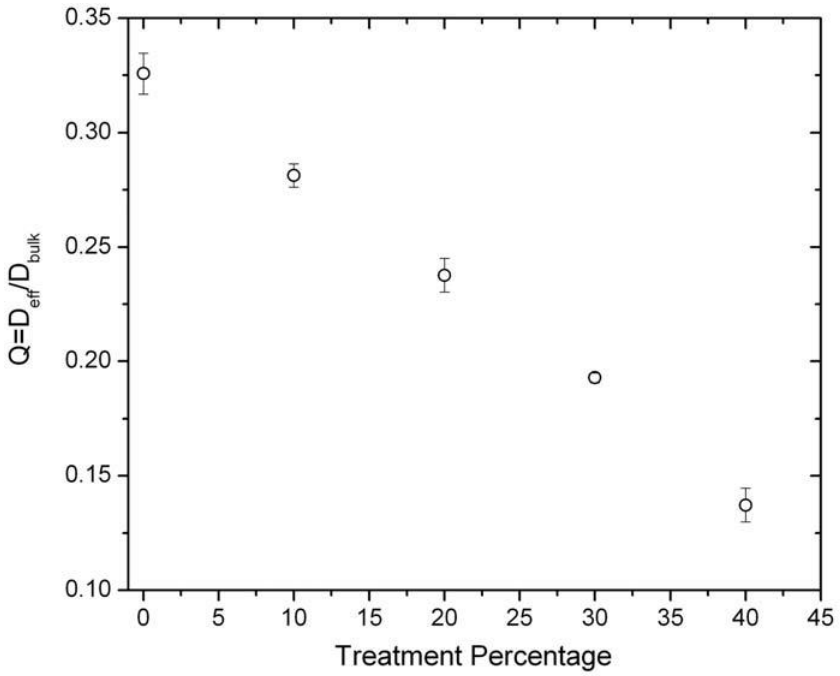

Figure 5.6: Effect of Teflon treatment (wt.%) on the diffusibility of oxygen-water vapor in nitrogen-water vapor mixture for a temperature of 80°C- error bars are shown in the figure.

5.4.1 Effect of Temperature

The effect of temperature on the thermal diffusivity of the carbon paper samples was measured in this study. The thermal diffusivity is the fundamental quantity that enters into transient heat transfer situations. Transient modeling of heat transport is of interest when considering cold start applications to monitor temperature change with time. The thermal diffusivity of TORAY-TPGH-120 carbon paper with no Teflon treatment and for the temperature range of -20 to +120 °C is given in Figure 5.7.

An empirical relation of the dependence of the in-plane thermal diffusivity with temperature can be deduced from the experimental data and is given as:

$$\alpha_{\text{apparent}} = -4.91 \times 10^{-11} T^3 + 1.42 \times 10^{-8} T^2 - 1.46 \times 10^{-6} T + 8.91 \times 10^{-5} \qquad (5.2)$$

where α_{apparent} is the measured thermal diffusivity and is given in m^2/s, T is the temperature in degrees Celsius and the coefficient of determination $R^2 = 0.993$.

Using the experimental measurements of the thermal diffusivity, the thermal conductivity can be calculated as discussed earlier using Equation (3.13). The in-plane thermal conductivity of untreated carbon paper for the temperature range of -20 to $+120$ ($^\circ C$) is given in

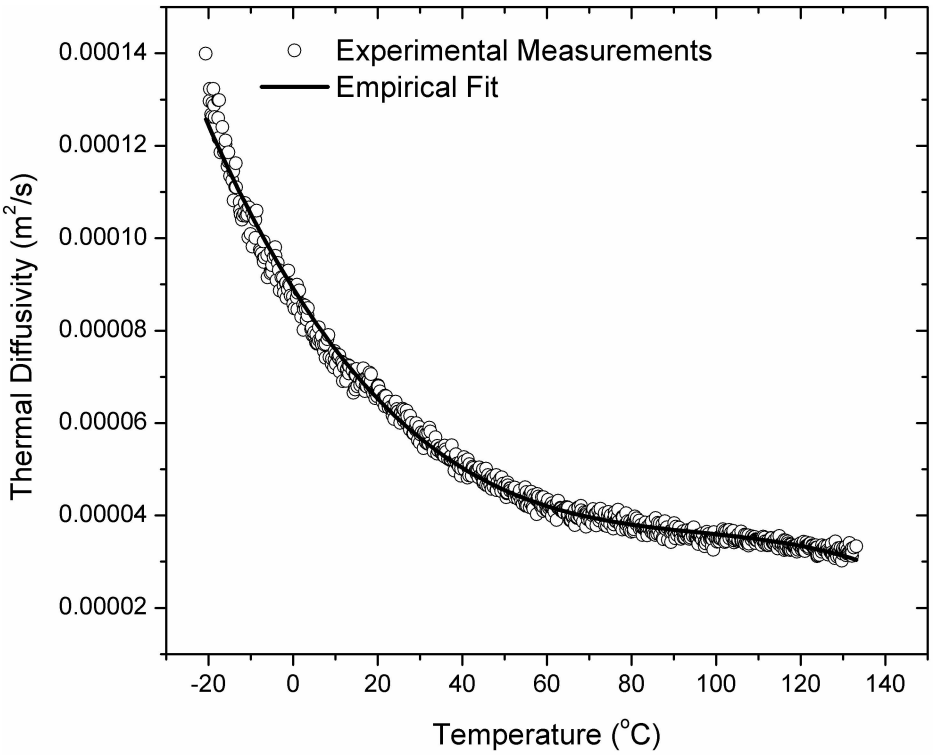

Figure 5.7: Effect of temperature on the in-plane thermal diffusivity of TORAY-TPGH carbon paper with no Teflon treatment - empirical fit is given by Equation (5.2)

Figure 5.8. As it can be seen, the thermal conductivity decreases with the increase of temperature. This trend follows that observed for various types of graphite [165, 166, 167]. This trend is expected since much of the heat transfer in the in-plane direction occurs through the fibers and as mentioned before, due to the heat treatment process that carbon paper undergoes during manufacturing the fibers graphitize.

Using the experimental data, an empirical correlation can be deduced for the dependence of the in-plane thermal conductivity on the temperature and it is given as:

$$k\text{eff}^{\text{in}} = -7.166 \times 10^{-6} T^3 + 2.24 \times 10^{-3} T^2 - 0.237T + 20.1 \tag{5.3}$$

where T is the temperature in degrees Celsius, $k\text{eff}^{\text{in}}$ is the thermal conductivity in the in-plane direction in W/m.K and $R^2 = 0.9864$.

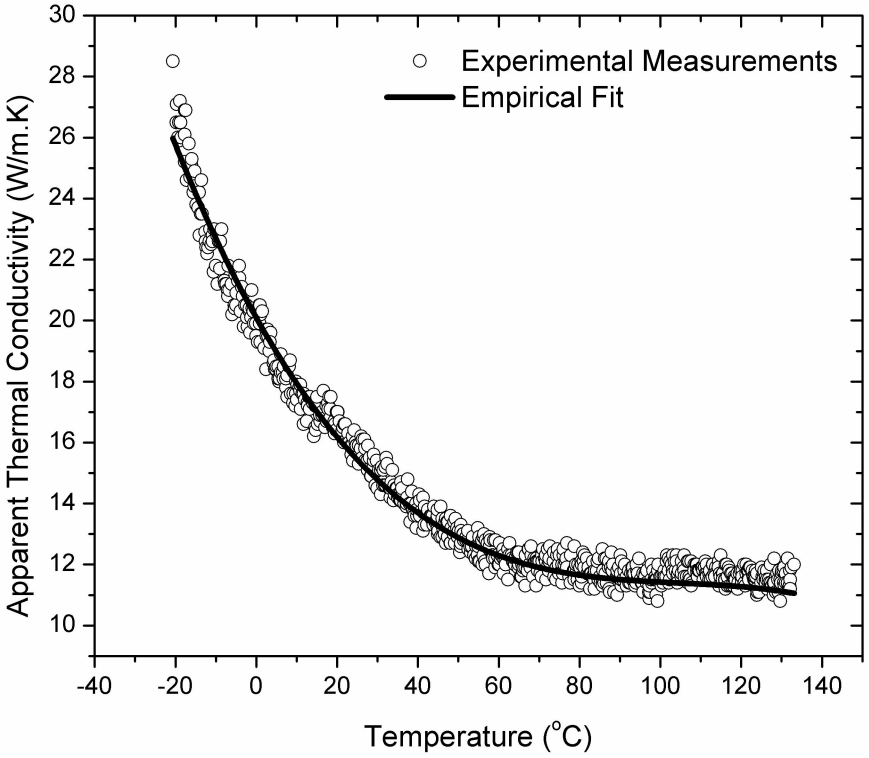

Figure 5.8: Effect of temperature on the in-plane thermal conductivity for an untreated carbon paper sample- Empirical Fit is given by Equation (5.3)

5.4.2 Effect of Teflon Treatment

The in-plane thermal diffusivity of TORAY-TPGH-120 carbon paper treated with various Teflon loadings (5, 20 and 50 wt.%) was measured and the findings are plotted in Figure 5.9. As it can be seen, the thermal diffusivity of the material decreases with an increase in Teflon loading. Adding 5 wt.% PTFE results in a drastic decrease of the thermal diffusivity. Further addition of Teflon loading does not do much more damage to the overall thermal diffusivity of the carbon paper sample.

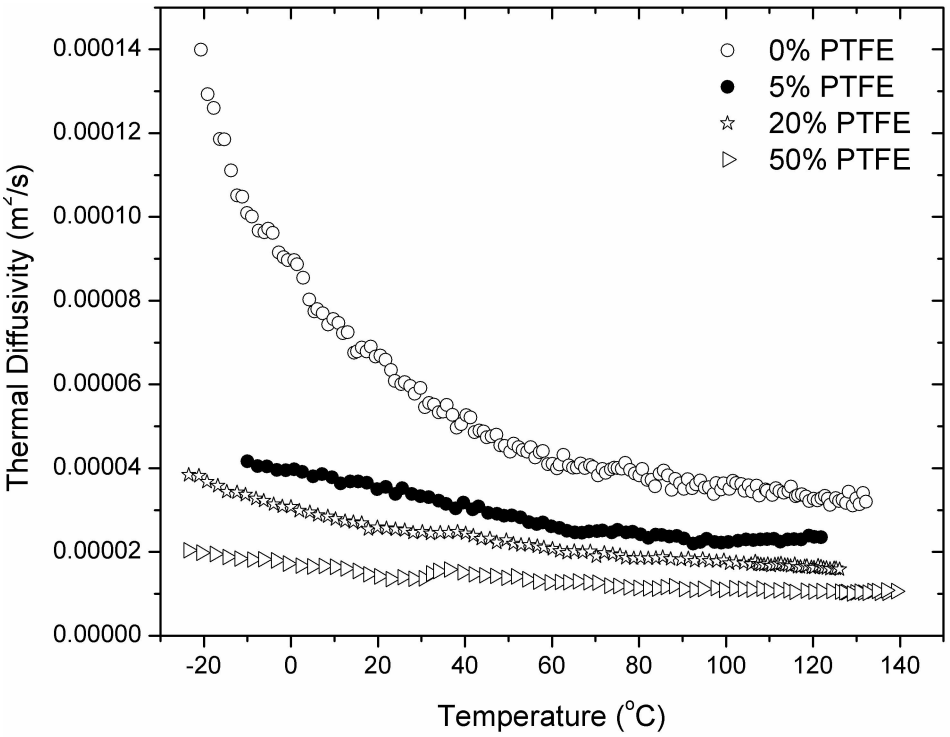

Figure 5.9: Effect of Teflon loading on the in-plane thermal diffusivity of TORAY-TPGH carbon paper

Using the measured thermal diffusivities, the effect of temperature on the in-plane thermal conductivity of two samples (0 and 5 wt.% PTFE) is shown in Figure 5.10. From this figure, it can be seen that the in-plane thermal conductivity is significantly reduced due to the addition of PTFE as low as 5 wt.%. This decrease can be attributed to the low thermal conductivity of Teflon ($\approx 0.35\,(W/m.K)$ [136].

The addition of PTFE to the carbon paper GDL increases the heat barrier resistance; hence, decreasing the overall thermal conductivity. It is also interesting to note that the in-plane thermal conductivity for the 5% sample is not as pronounced as that for the 0% sample. This finding implies that the presence of Teflon in the sample is the main contributor to the thermal resistance. As shown in Figure 5.12(b), the effect of temperature on the thermal conductivity of PTFE is minimal. This same trend is observed for higher PTFE contents as shown in Figure 5.11.

In this figure, the change of the in-plane thermal conductivity with temperature for the 20% and 50% samples is given. It is interesting to observe the two peaks shown in the figure. A minimum apparent thermal conductivity is reached at a temperature of 23.5 ($^{\circ}C$) and a maximum is reached at a temperature of 35 ($^{\circ}C$). This trend can be explained by

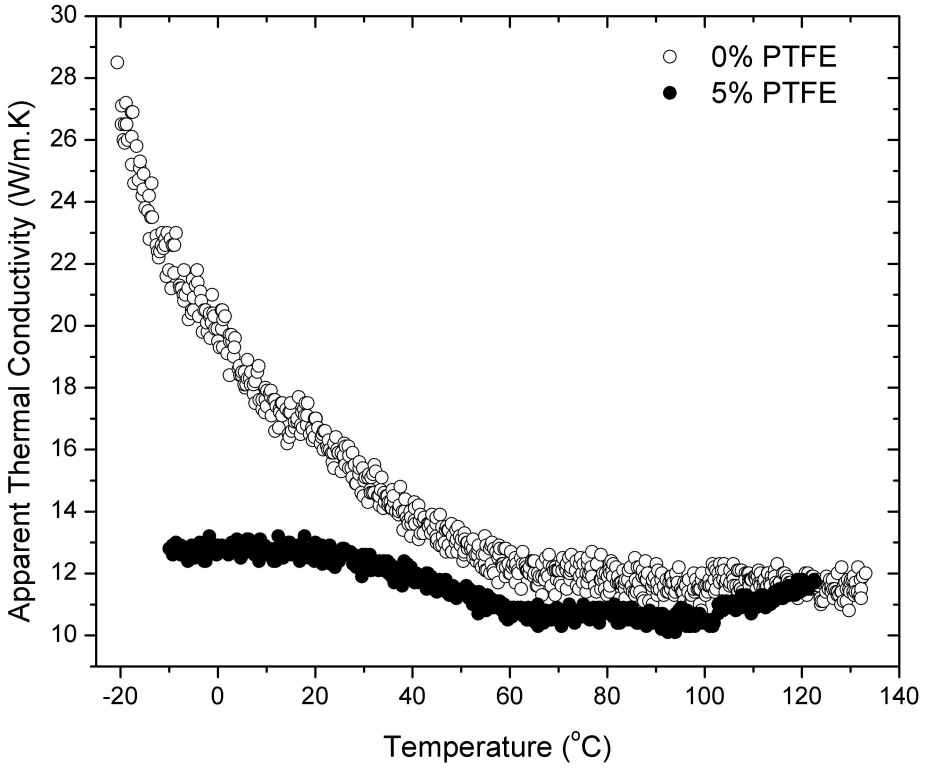

Figure 5.10: Comparison between 0% and 5% Teflon loading

visiting the specifications of Teflon shown in Figure 5.12. Blumm et al. [136] measured the thermal expansion and expansivity of PTFE as shown in Figure 5.12(a) for the temperature range of $-130°C$ to $+150°C$. Thermal expansivity, also known as the physical coefficient of thermal expansion, is defined as the rate of expansion divided by the original sample length. They found that the sample length increases over the entire temperature range with a slight increase in the rate of expansion versus temperature. Beginning at $19.2°C$, they detected two overlapped steps in the thermal expansion curve. They explained that these steps are a result of the solid-solid transition [168]. An expansion step of approximately 0.4% was measured from the well ordered to the partially ordered phase, while a smaller step of approximately 0.1% was measured for the transition from the partially ordered to the very disordered phase above $35°C$. On the thermal conductivity graph of the 20% and the 50% samples, these transitions are seen at temperatures of $34.2°C$ and $21°C$. However, as expected they are more pronounced for the higher PTFE loading.

Further, an important observation that should be mentioned in this section is the change of the in-plane thermal conductivity with the Teflon loading. The addition of as little as 5 wt.% PTFE to the carbon paper GDL results in a decrease in the in-plane thermal conduc-

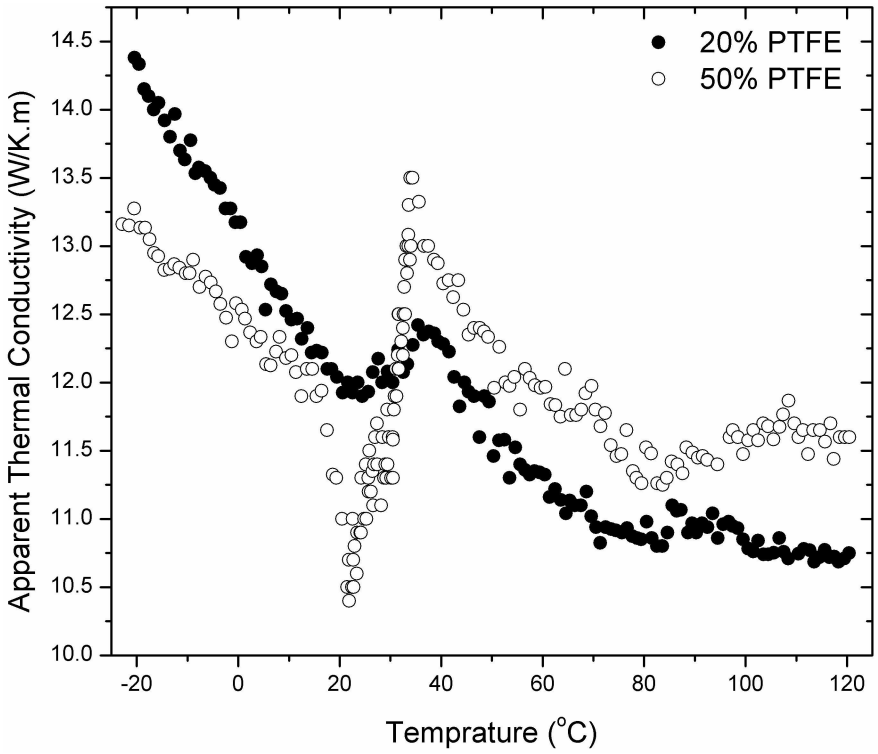

Figure 5.11: Effect of PTFE on the in-plane thermal conductivity of carbon paper GDL

tivity. Further increases to the PTFE loading does not affect the overall in-plane thermal conductivity. For the three studied PTFE loadings, the in-plane thermal conductivity lies in the range of 10.1-14.7 (W/m.K).

Finally, due to the lack of measurements of the in-plane thermal conductivity published in literature, it is difficult to carry out a full comparison. However, the measurements done by Teerstra et al. [73] can be used for some comparison. In their study, they measured the in-plane thermal conductivity of TORAY carbon paper with 3% wt. PTFE at 70°C to be 15.1±0.2 (W/K.m), which compares well with the measurements of this study. At 70°C, we measured the thermal conductivity of TORAY carbon paper with 0% and 5% wt. PTFE to be 12.5±0.9 and 10.6±0.7 (W/K.m), respectively

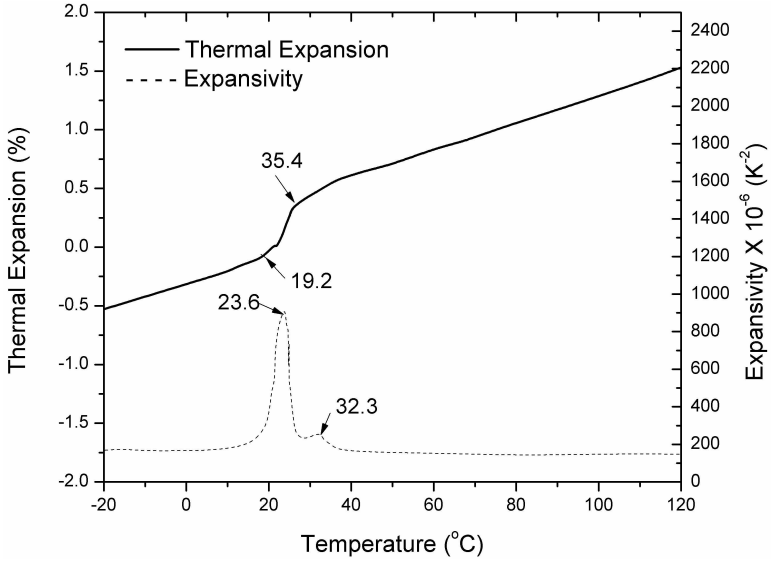

(a)

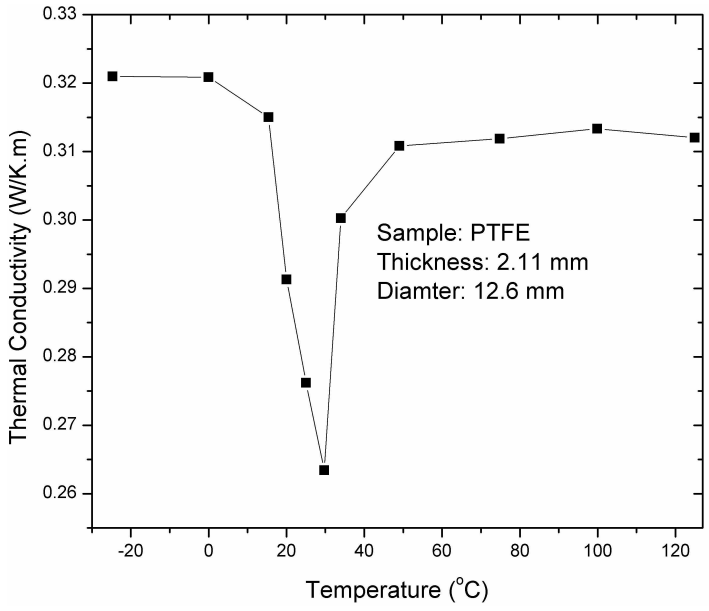

(b)

Figure 5.12: (a) Thermal expansion and expansivity of the PTFE material; (b) Thermal conductivity of the PTFE material [136]

5.5 Thermal Conductivity - Through-plane

In order to investigate the effect of anisotropy on the effective thermal conductivity, it is necessary to experimentally measure the through-plane thermal conductivity. As was shown earlier, the in-plane thermal conductivity is highly influenced by the temperature and PTFE. Hence, the effects of temperature, PTFE loading and deformation on the through-plane thermal conductivity were measured and are presented in the following sections. Two deformation levels are investigated in this thesis, 16% and 1%, which are indicated as high and low deformation, respectively. As it is shown in Figures 5.13 and 5.14, the combined effect of these three factors is complicated.

5.5.1 Effect of Deformation

Deformation of the carbon paper GDL in the direction of its thickness (through-plane direction) is very common during the assembly of the cell. The pressure used to compress the components of the cell will result in the decrease of contact resistances between these components; hence, facilitating the transport processes.

From Figure 5.13, it can be easily seen that this compression has a significant effect on the through-plane thermal conductivity. The thermal conductivity increases as the compression level increases, which is attributed to the increase in contact area between the stacked carbon fibers. In other words, the contact resistance between these fibers is reduced due to the compression.

At low deformation, the through-plane thermal conductivity increases with an increase in temperature. This increase can be attributed to the thermal expansion of the graphitized carbon fibers. Due to the increase in temperature, the contact resistance between the fibers is decreased; hence, the overall conductivity of the fibers is increased. This trend is especially interesting when considering the change of the in-plane thermal conductivity with temperature. As was shown in the previous section, the in-plane thermal conductivity of TORAY-TPGH-120 carbon paper decreases with an increase in temperature. Hence, these two findings suggest that the structure of the carbon may be directionally dependent. Further, this change in trend with temperature could be related to cracks in the carbon binder, which usually exist in the through-plane direction and lead to thermal resistance. This phenomenon is discussed in more detail in the next chapter of this thesis.

The trend at high deformation is not as straight forward. At high deformation, the thermal conductivity of the untreated carbon paper increases with temperature under sub zero conditions. However, at temperatures higher than $0°C$, the thermal conductivity of

the sample decreases with the increase in temperature, which is in agreement with the measurements of Khandelwal and Mench [66]. This trend suggests that a change in the crystal structure of the carbon occurs at around zero degrees Celsius. In the case where Teflon is added to the sample, the thermal conductivity of the carbon paper increases with the increase in temperature and reaches a constant value at a temperature of around $35°C$. This temperature value corresponds to the temperature at which PTFE transitions from the partially ordered to the very disordered phase [136]. Further, another two instances where a phase change occurs were measured for the 60% sample at $3°C$ and $17°C$. Blumm et al. [136] detected an expansion step for a pure PTFE sample at $19.2°C$ that was attributed to a partially ordered phase. This expansion resulted in a decrease in the thermal conductivity of the PTFE sample. A similar analogy can be used to explain the sudden decrease in thermal conductivity of the 60% sample at about $17°C$.

5.5.2 Effect of Teflon Treatment

The effect of PTFE loading on the through-plane thermal conductivity is investigated for two different loadings (0 and 60 wt.%) at both deformation levels (low and high) as given in Figure 5.14. As it can be seen, the general trend at both deformation levels is the same in that the thermal conductivity of the carbon paper GDL decreases with the increase in Teflon loading. This decrease is generally attributed to the low thermal conductivity of PTFE, which increases the overall heat barrier resistance. This trend was also observed earlier for the in-plane thermal conductivity. Further, it is interesting to point out that the through-plane thermal conductivity of both samples (0% and 60%) at high deformation is comparable at temperatures higher than $35°C$. As mentioned earlier, this temperature is denoted as a temperature where a phase change in PTFE occurs. Further, from Figure 5.14, it can be seen that at high deformation levels, the thermal conductivity of both samples is scattered around an average value. The thermal conductivity of both samples under high deformation lies in the range of $1.3 \leq k \leq 1.6$ W/K.m. with the average thermal conductivity around 1.45 W/K.m. This finding suggests that the thermal conductivity is no longer dependent on the PTFE content in the carbon paper sample. This is similar to the trend observed for the in-plane thermal conductivity earlier in this chapter. In addition, the change in the PTFE structure at high temperatures, coupled with the high deformation, might be resulting a contact area between the carbon fibers as that of the untreated sample.

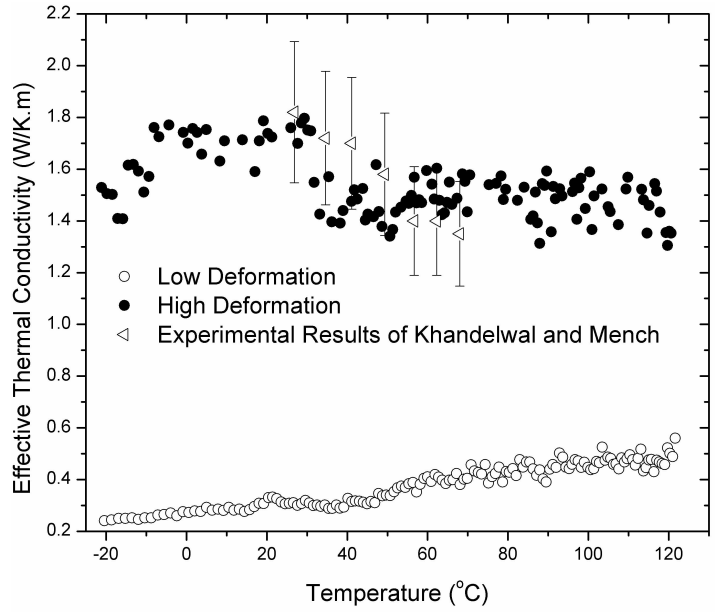

(a)

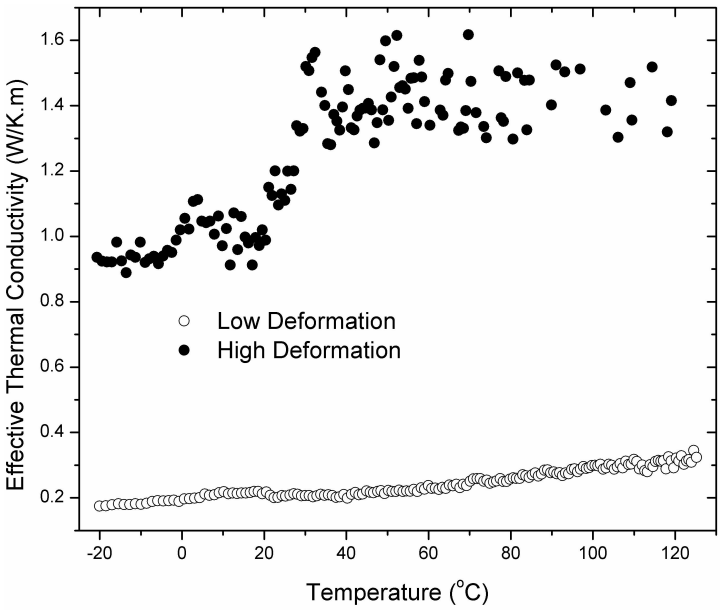

(b)

Figure 5.13: Effect of deformation on the through-plane thermal conductivity of TORAY carbon paper - Other experimental measurements taken from [66] (a) 0% PTFE loading; (b) 60% PTFE loading.

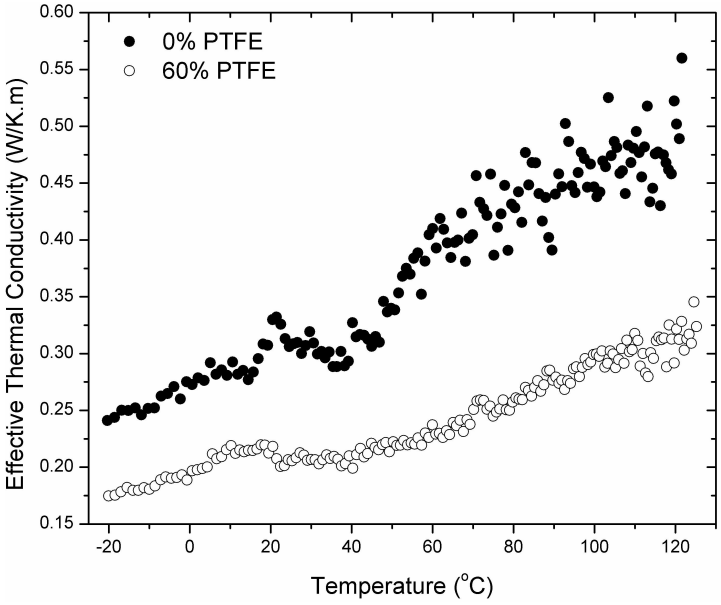

(a)

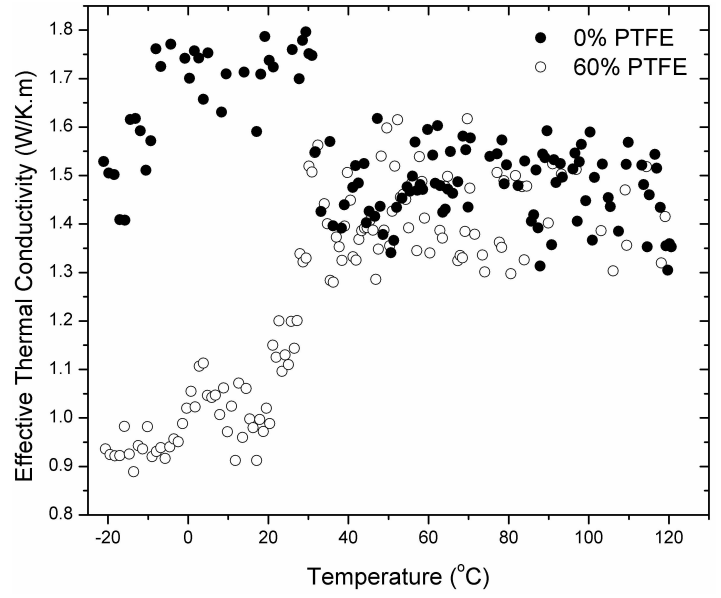

(b)

Figure 5.14: Effect of Teflon loading on the thermal conductivity of carbon paper under (a) Low deformation; (b) High deformation

5.6 Chapter Summary

In this chapter, the structure of the carbon paper GDL, the effective diffusion coefficient and effective thermal conductivity were all investigated experimentally using the experimental apparatus discussed earlier in Chapter 3 of this thesis.

Using the method of standard porosimetry, the pore structure of the GDL was characterized. Using octane as the wetting fluid, the total pore area of the carbon paper GDL was investigated for different PTFE loading. It was shown that the addition of Teflon to the carbon paper GDL resulted in a decrease of the overall pore area of the carbon paper GDL. However, the overall trend of the pore distribution was similar and despite the addition of 50 wt.% PTFE to the carbon paper, most of the pores in the carbon paper lay in the macro category. Further, it was shown that the capillary pressure versus wetting-phase saturation decreased once PTFE was introduced to the carbon paper sample. This decrease is mainly attributed to the increased hydrophobicity of the carbon paper GDL in the presence of Teflon.

Further, a Loschmidt cell was used to measure the through-plane effective diffusion coefficient of the carbon paper GDL of PEM fuel cells. The effects of temperature and Teflon treatment on the overall diffusibility of the gases were investigated. It was found that the temperature does not affect the overall diffusibility of the gas in carbon paper. The addition of Teflon to carbon paper results in the decrease of the overall diffusibility of the gases in the layer mainly due to the decrease in porosity of the layer. A comparison between the determined and that predicted by the existing effective diffusion coefficient models available in literature indicated that these models over predict the effective diffusion coefficient significantly. This overprediction can lead to underestimating the mass transport limitations in the gas diffusion layer of PEM fuel cells, especially at high current densities and low porosity values.

Finally, the method of monotonous heating was used to investigate the effect of anisotropy on the thermal conductivity of thin carbon paper for a wide temperature range encountered in the practical application of PEM fuel cells. Both the in-plane and through-plane thermal conductivity of carbon paper were measured for the temperature range from $-20°C$ to $+120°C$. The dependence of the in-plane thermal conductivity on the temperature was more straight forward than its through-plane counterpart. It was found that the in-plane thermal conductivity decreases with an increase in temperature reaching an asymptotic value. However, the change of the through-plane thermal conductivity with temperature was found to be highly dependent on the compression pressure. This could be mainly attributed to the

cracks and gaps between the fibers and the change of the thermal resistance due to these imperfections with temperature. Further, the effect of Teflon on the thermal conductivity in both directions was investigated. It was shown that the addition of Teflon dramatically decreased the thermal conductivity. In the in-plane direction, a phase change was shown to occur around $21°C$ and $35°$ degrees in samples with high Teflon loading (20 and 50 wt.%). For the three studied PTFE loadings (5, 20, and 50 wt.%), the in-plane thermal conductivity lies in the range of $10.1 - 14.7$ $(W/m.K)$.

Chapter 6

Results and Discussion – Numerical – Dry GDL

An Understanding of the limitations of mass transport in the gas diffusion layer (GDL) of polymer electrolyte membrane (PEM) fuel cells is crucial in the research and progress of this technology. Due to the complexity of monitoring species transport experimentally, numerical simulations are often preferred and used to investigate mass transport in PEM fuel cells. However, due to the complex structure of the GDL, the macro-homogeneous assumption is often utilized. In other words, the structure of the layer is simplified and all the ingredients of the layer are assumed to be evenly distributed over the layer. Hence, the effective diffusion coefficient is used to simulate the diffusion of the gaseous species through the layer. This effective coefficient is lower than its corresponding bulk coefficient due to the presence of the solid matrix in the GDL. Currently, the Bruggeman Approximation is the most widely used correlation for estimating the effective diffusion coefficient in the GDL. Other semi empirical models are also available and have been discussed in the Literature Review Chapter. However, these correlations overestimate the effective diffusion coefficient due to the assumptions on which they are based.

Heat management is another important aspect for PEM fuel cell commercialization. Due to the porous nature of the gas diffusion layer and its complexity of anisotropy, the effect of the structure on the thermal conductivity is usually taken into account by introducing an effective thermal conductivity. For the purpose of PEM fuel cell modeling, the thermal conductivity of the GDL is often estimated through series or parallel resistances. However, these expressions do not take into account the complex structure of the GDL; hence, they either over or under estimate the thermal conductivity of the layer.

Finally, the transport of electrons is another important determinant of the overall electro-

chemical reaction rate and to understand it, numerical models are often utilized. Currently, the Bruggeman Approximation is used to estimate the effective electrical conductivity in the carbon paper GDL. This correlation overestimates the effective electrical conductivity and ignores the anisotropic nature of the GDL.

Realizing the need for correlations of the effective properties of the GDL, the numerical model of this thesis is used to estimate the effective diffusion coefficient, effective thermal conductivity and effective electrical conductivity of a dry gas diffusion layer. In this chapter, the numerical results are compared to both the available experimental data and theoretical approximations. Finally, correlations for both the through-plane and in-plane directions are proposed. The results presented in this chapter are presented in the journal articles [169, 170].

6.1 Diffusion Coefficient

6.1.1 Comparison to Experimental Data

The structure of carbon paper is anisotropic; hence, the diffusion of species is directionally dependent. The diffusion is simulated in both the in-plane and through-plane directions to obtain the corresponding diffusion coefficients and the numerical results are compared to experimental data as given in Figure 6.1.

The anisotropic nature of the carbon paper is found to have an effect on the diffusion process. Hence, the assumption that the gas diffusion layer of a PEM fuel cell is isotropic is not valid. Further, it is seen that the in-plane diffusion of gases is faster than that in the through-plane direction. This finding is consistent with the structure of the carbon paper. The diffusion resistance is higher in the through-plane direction due to the arrangement of fibers. This implies that the use of the anisotropic carbon paper can help increase the overall diffusion magnitude of gases in the GDL. Finally, a threshold porosity, ϵ_p, at which the effective diffusion coefficient becomes zero exists and is in the range $0.2 < \epsilon < 0.3$. The existence of the threshold porosity implies that the fibers are packed in such a way prohibiting the diffusion process from occurring. This analogy is similar to sphere packing.

To verify the accuracy and validity of the numerical method, the results of the numerical model were compared to experimental data. The experimental results of this thesis were obtained for a TORAY carbon paper (TPGH-120) with various Teflon treatment percentages. TORAY carbon paper (TPGH-60) was used to obtain the experimental data for the study by Kramer et al. [53]. Although the experimental data by the two studies were obtained

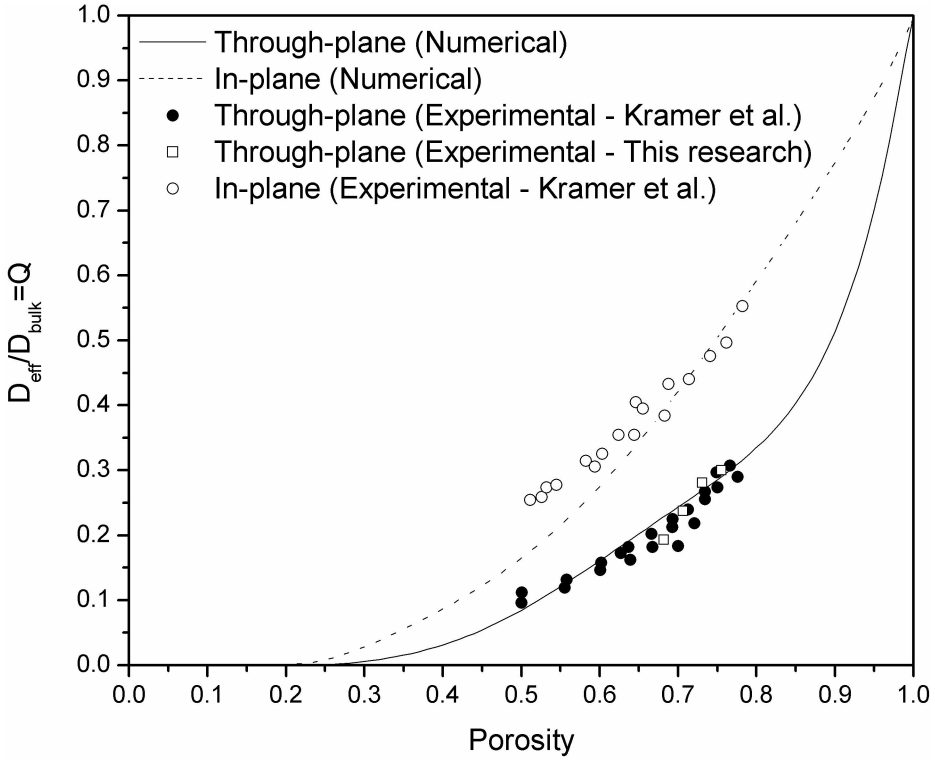

Figure 6.1: Comparison of numerical results of the in-plane and through-plane diffusibility of gases in carbon paper with experimental data of Kramer et al. [53] and experimental measurements of this thesis.

using two different samples, the measurements are still comparable since the samples are manufactured by the same company using the same technique. The only difference between the two samples is their thickness.

Experimental data is not available for the entire porosity range of $0 \leq \epsilon \leq 1$ simply because carbon paper is not available commercially for that range. The porosity range for untreated carbon paper, which is available in market, is $0.75 \leq \epsilon \leq 0.9$. With the addition of Teflon treatment, the lower limit of this porosity range can be decreased. Kramer et al. [53] compressed their carbon paper samples during measurements in order to obtain an even lower porosity range. The compressive force used was studied carefully to ensure that the carbon fibers do not fracture. A good agreement between the numerical and measured results of Kramer et al. [53] is seen; refer to Figure 6.2. For the in-plane diffusibility, the numerical results deviate from the measured data at the low porosity range. This deviation could be due to compressing the carbon paper during measurements to obtain the desired porosity. No error range has been reported for the measured data making it difficult to further understand this difference.

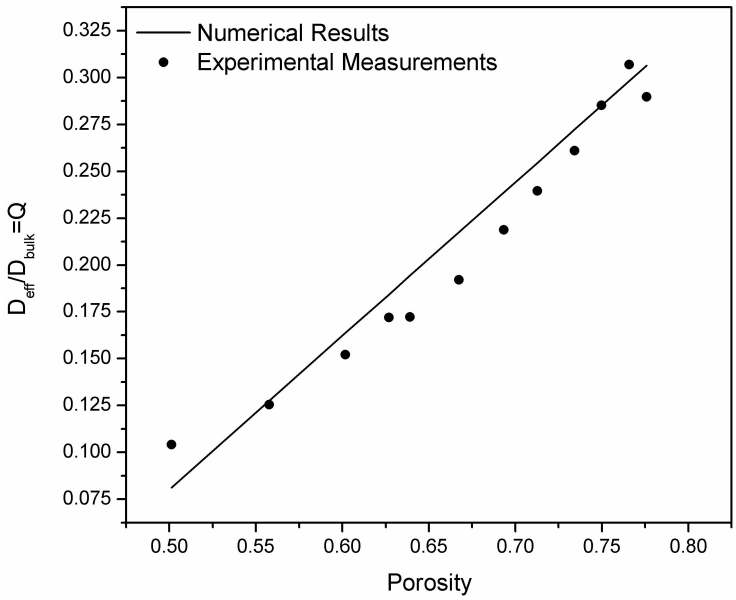

(a)

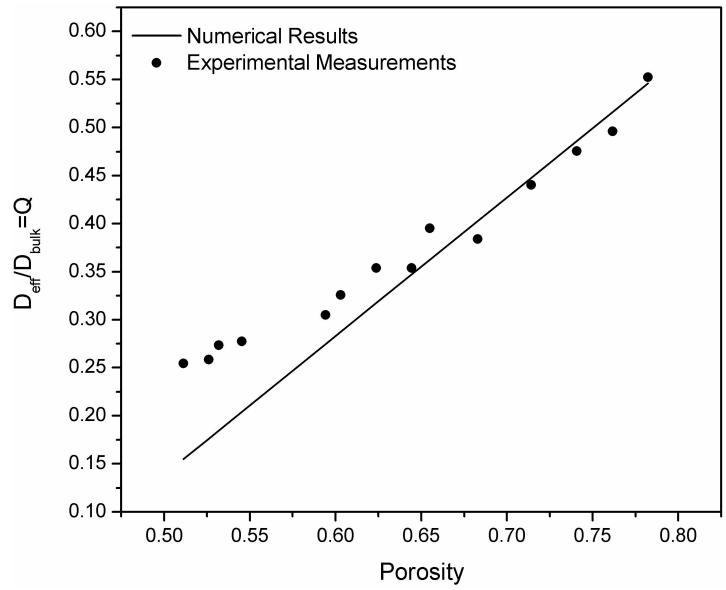

(b)

Figure 6.2: Comparison between the present numerical results and experimental data by Kramer et al. [53] for the porosity range of $0.5 \leq \epsilon \leq 0.77$. (a) Through-plane direction; (b) in-plane direction.

6.1.2 Comparison to Theoretical Models

As mentioned earlier, many theoretical expressions of the effective diffusion coefficient of carbon paper exist with the Bruggeman Approximation being the most widely used in numerical simulations. These theoretical expressions were discussed in detail in Chapter 2 and summarized in Table 2.1. A comparison between the effective diffusion coefficient estimated by the numerical model and that calculated by the theoretical models is given in Figure 6.10.

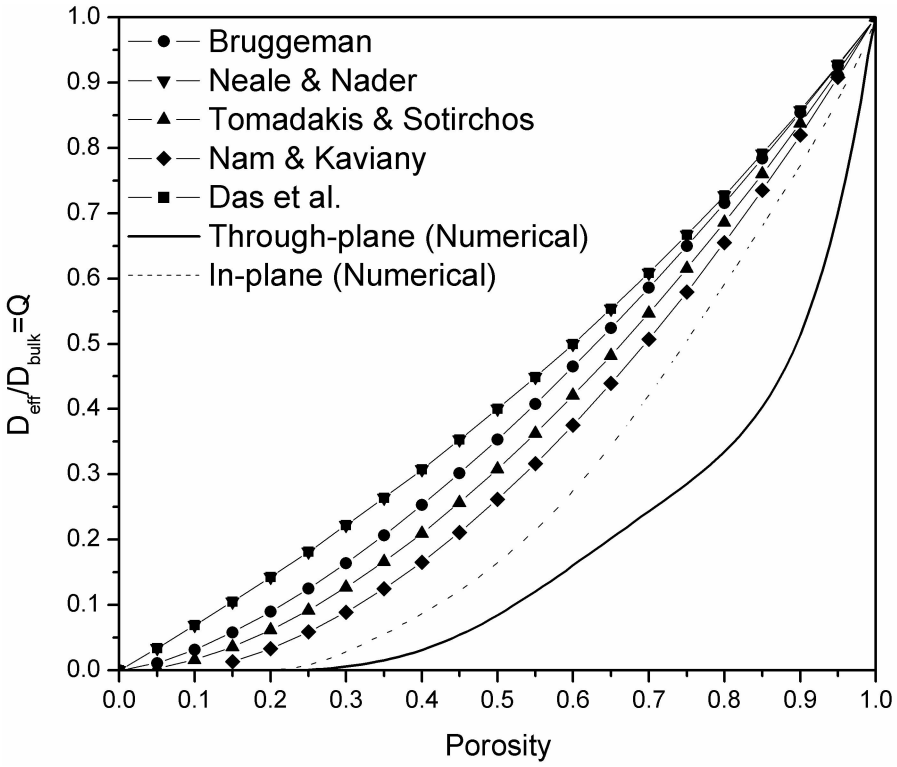

Figure 6.3: Comparison of the diffusibility evaluated numerically and using the models available (see Table 2.1 for these models).

From the comparison, it is immediately obvious that all the available correlations overpredict the diffusibility in the GDL in both, in-plane and through-plane, directions. Overpredicting the mass diffusion through the GDL can result in underestimating the mass transport limitations in the layer, especially at high current densities. Underestimating the limitations also occurs due to ignoring the direction dependency of the diffusibility. It is obvious that the through-plane diffusibility is much lower than the in-plane diffusibility. Equating the two will result in inaccurate simulations of the mass diffusion in the GDL.

It is also interesting to note that there are some obvious differences between the two types of correlations. The percolation theory requires that a percolation threshold $\epsilon_p > 0$

exists. This is, however, not required for the effective medium approximation and in turn it assumes that diffusion in a porous medium can occur until the porosity of that medium reaches zero. Finally, studying the numerical and analytical results, the correlation by Nam and Kaviany [47], Equation (2.20), gives the closest agreement to the numerical results.

6.1.3 Proposed Correlation

The comparison between the numerical results of the effective diffusion coefficient in carbon paper GDL and that calculated by the available theoretical expressions raises the need for a more representative correlation. The available expressions do not just overestimate the diffusibility of gases in the carbon paper, they are also independent of direction. The correlation developed for the diffusibility of gases in this thesis is based on the upper Hashin bound. In order to take the statistical randomness of the geometry as well as the structure of the solid matrix of the carbon paper GDL into account a function $f(\epsilon)$, should be introduced to the expression by Das et al. [48] as follows:

$$\frac{D_{\text{eff}}}{D_{\text{bulk}}} = 1 - f(\epsilon)\frac{3(1-\epsilon)}{3-\epsilon} \tag{6.1}$$

where $f(\epsilon) \geq 0$ and could vary depending on the geometry of the solid matrix. For the purpose of this thesis, the function $f(\epsilon)$, which will be used to fit the data, is expressed in the form of:

$$f(\epsilon) = A\epsilon\cosh(B\epsilon - C) \tag{6.2}$$

where A, B and C are fitting parameters. Thus, curve fit to be used for the in-plane and through-plane diffusibility is:

$$\frac{D_{\text{eff}}}{D_{\text{bulk}}} = 1 - A\epsilon\cosh(B\epsilon - C)\left[\frac{3(1-\epsilon)}{3-\epsilon}\right] \tag{6.3}$$

Using Equation (6.3), the curve fit for the porosity range $0.33 \leq \epsilon \leq 1$ is shown to have good agreement with the numerical results as illustrated in Figure 6.4. A very good agreement between the fitted results and the numerical results is shown. The values for A, B and C for the through-plane and in-plane directions are given in Table 6.1 along with the errors and the values of R^2.

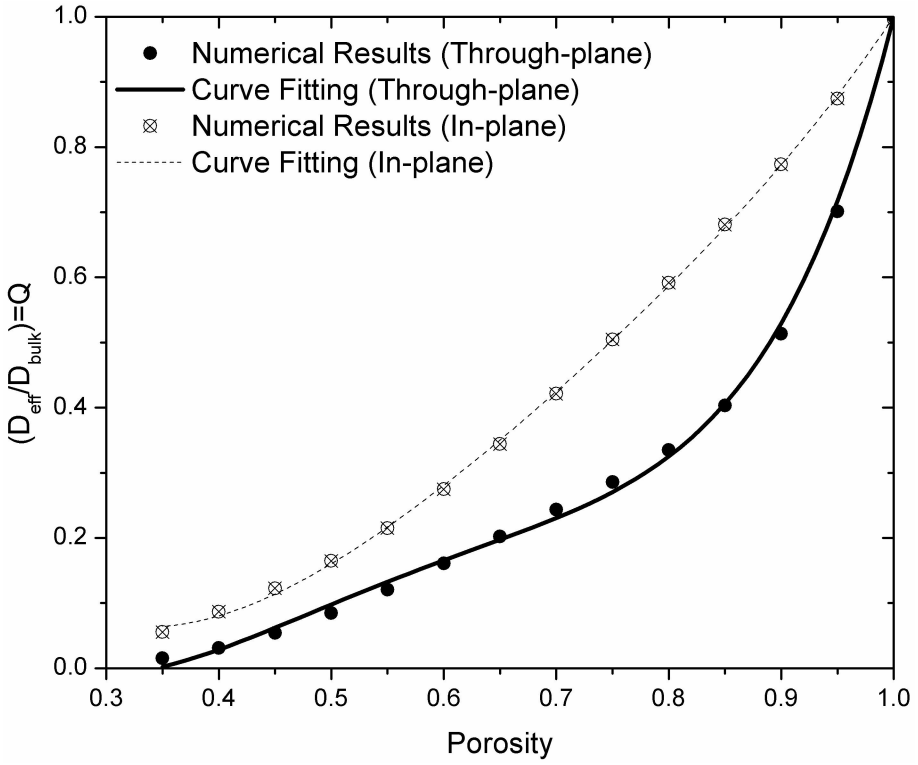

Figure 6.4: Comparison between the present numerical results and the curve fit from Equation (6.3) for the diffusibility in the through-plane and in-plane directions.

Table 6.1: Fitting parameters for Equation (6.3) shown in Figure 6.4

Direction	**A**	**B**	**C**	R^2	**Validity Range**
Through-plane	2.76 ± 0.00	3.00 ± 0.03	1.92 ± 0.01	0.999	$0.33 \leq \epsilon \leq 1$
In-plane	1.72 ± 0.02	2.07 ± 0.02	2.11 ± 0.01	0.999	$0.33 \leq \epsilon \leq 1$

6.2 Thermal Conductivity

6.2.1 Comparison to Experimental Data

Although much effort has been dedicated to measuring the effective thermal conductivity in carbon paper, the porosity range for which this data is available is small. Nonetheless, the effective thermal conductivity of the reconstructed carbon paper GDL for various porosity values was compared against experimental data by Burheim et al. [69] and Karimi et al. [70] as illustrated in Figure 6.5. Burheim et al. [69] measured the effective thermal conductivity of SolviCore carbon paper originally at a porosity of $83 \pm 2\%$ and at room temperature.

The numerical results used for comparison were obtained using a thermal conductivity of 140 $W/K.m$ for the solid fibers. Their data for the compression factor versus compression pressure was used in this thesis to obtain the porosity of the GDL after compression. The porosity of the compressed GDL was found via:

$$\epsilon_f = 1 - (1 - \epsilon_0)\left(\frac{\delta_0}{\delta_f}\right) \tag{6.4}$$

where ϵ_f and ϵ_0 are the porosity of the compressed and uncompressed GDL, respectively and δ_0 and δ_f are the thicknesses of the uncompressed and compressed GDL, respectively.

Karimi et al. [70] also examined the effects of compression on SpectraCarb carbon paper with an uncompressed porosity of 80% and at 70°C. The effect of compression on porosity of the GDL was again calculated using Equation (6.4). A thermal conductivity of 95 $W/K.m$ was used for the solid fibers to obtain the numerical results for this comparison. The thermal conductivity of the solid fibers is effected by temperature and it decreases with the increase in temperature.

The comparison of the numerical results with the experimental data of Burheim et al. [69] and Karimi et al. [70], in Figure 6.5, was made based on the similarities of structures. The numerical model is built for carbon paper, which is composed of straight fibers. As it can be seen, the trend of the experimental and numerical results is very similar. The numerical results agree very well with the experimental findings in [69]. The differences between the results of this thesis and that of reference [70] might be due to slight differences in structure.

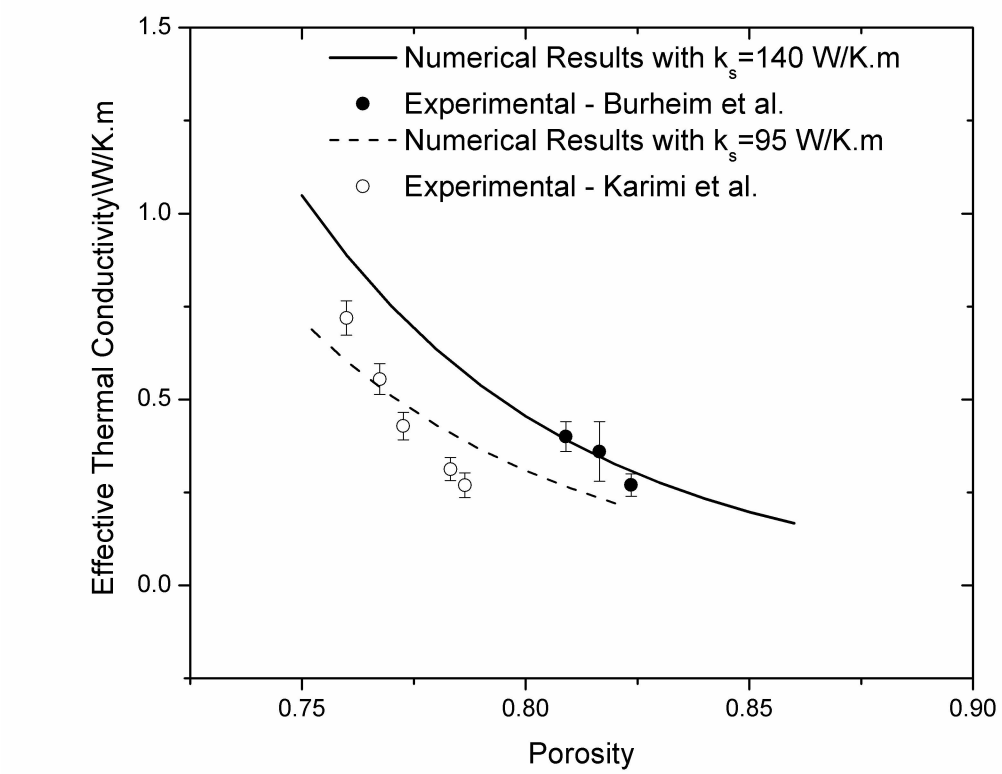

Figure 6.5: Comparison of the through-plane effective thermal conductivity of this thesis and the experimental results by Burheim et al. [69] and Karimi et al. [70].

The numerical results of this thesis were also compared against the experimental results of Khandelwal and Mench [66] and that of this thesis as shown in Figure 6.6. In their study, they measured the effect of temperature on the through-plane effective thermal conductivity of TORAY carbon paper. They showed that the through-plane effective thermal conductivity decreases with the increase of temperature. This decrease is mainly attributed to the decrease of the carbon thermal conductivity with the increase in temperature. The experimental results of this thesis used for the comparison are those measured under high deformation. A further comparison between the numerical and experimental results of this thesis is put forward in the following sections. It is clear that the numerical and experimental results are in very good agreement. The thermal conductivity of the carbon fibers was estimated using the results of the in-plane thermal conductivity presented earlier in this thesis. The thermal conductivity of the carbon fiber for the temperature range used in this comparison

was evaluated using the following expression:

$$\lambda_{\text{solid}} = \frac{(-7.166 \times 10^{-6} T^3 + 2.24 \times 10^{-3} T^2 - 0.237T + 20.1)}{f(\epsilon_0)} \tag{6.5}$$

where $f(\epsilon_0)$ is a function of the porosity of the untreated, uncompressed sample used for the measurements of the in-plane thermal conductivity and is estimated by the numerical model to be 0.10006 for the porosity value of $78\% \pm 2\%$.

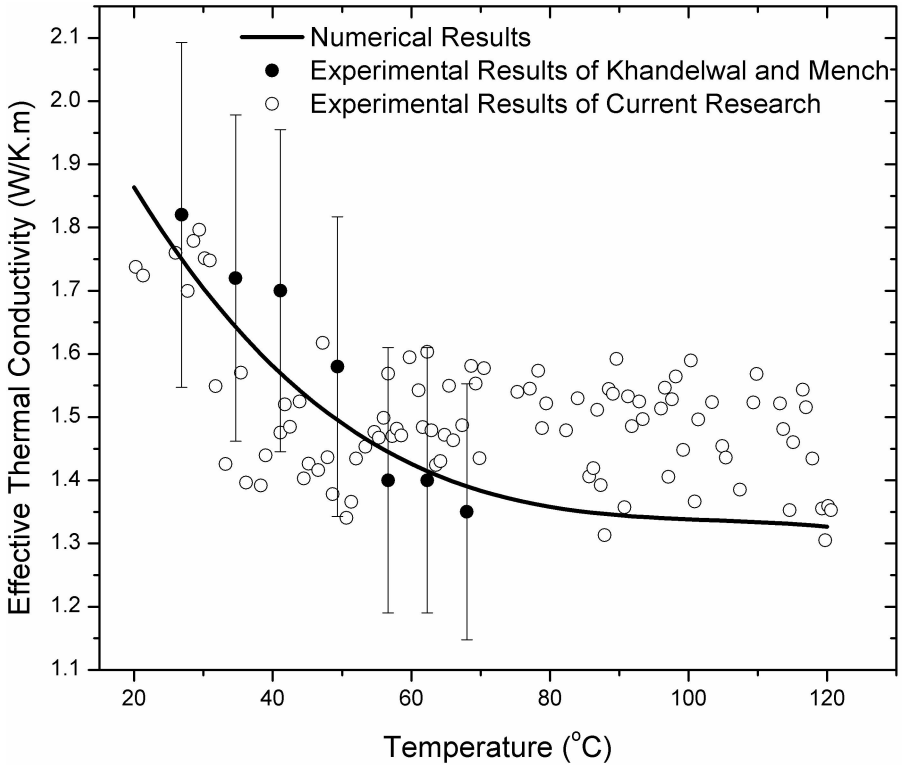

Figure 6.6: Comparison of the through-plane effective thermal conductivity of this thesis and the experimental results by Khandelwal and Mench [66] and this thesis.

6.2.2 Effect of Porosity

Using the reconstructed GDL, the effect of porosity on the effective thermal conductivity of the carbon paper GDL was investigated. As it was shown earlier, the experimental data available in literature for the through-plane effective thermal conductivity covers a very narrow range and scarce. Thus, for the purpose of validating the numerical results of this thesis, the numerical results are compared to the theoretical lower and upper bounds as

suggested by Hashin and Shtrikman [49]. Since the thermal conductivity of carbon paper is much higher than that of air, a thermal conductivity ratio $\left(\frac{k_{\text{eff}}}{k_{\text{s}}}\right)$ is introduced and the upper and lower bounds given earlier in Equation (2.26) can be re-written as:

$$0 < \frac{k_{\text{eff}}}{k_{\text{s}}} \leq 1 - \frac{3\epsilon}{3 - (1 - \epsilon)} \tag{6.6}$$

The in-plane and through-plane effective thermal conductivity of the reconstructed GDL are given in Figure 6.7. In this case, compression effects are not taken into account and the porosity range is due to the addition of carbon fibers. As expected, the effective thermal conductivity increases with the decrease of porosity and its increase is very sensitive to the change in porosity. A low porosity value corresponds to a high percentage of carbon fibers. The thermal conductivity of carbon fibers is much higher than that of air (over 4000 times higher); hence, its contribution to the effective thermal conductivity increases with the decrease in porosity. Further, it is important to point out that due to the fiber orientation, the in-plane effective thermal conductivity is found to be much higher than that in the through-plane direction. It is then expected that the temperature gradient in the in-plane direction will be less than that in the through-direction due to the higher thermal conductivity.

Due to the lack of experimental measurements and theoretical estimations of the effective thermal conductivity of the carbon paper GDL, it has been difficult to obtain a correlation, which can be used to simulate heat transfer in the GDL of PEM fuel cells. Using the numerical results obtained in this thesis, a proper correlation for the through-plane and in-plane ETC in PEM fuel cells GDL is developed. In the study by Das et al. [48], they suggested that the upper Hashin bound can be used to derive proper correlations for the effective properties of the carbon paper GDL. They proposed that a structural function, $f(\epsilon) > 0$, must be introduced to taken into account the effect of the geometrical distribution of the carbon fibers as follows:

$$\frac{k_{\text{eff}}}{k_s} = 1 - f(\epsilon)\frac{3\epsilon}{3 - (1 - \epsilon)} \tag{6.7}$$

where k is the thermal conductivity, s and eff are the solid and effective properties, respectively. In this thesis, the correlation for the in-plane and through-plane ETC is developed by fitting Equation (6.2.3) to the numerical results with the structural function being:

$$f(\epsilon) = A(1 - \epsilon)^B \exp\left[C(1 - \epsilon)\right] \tag{6.8}$$

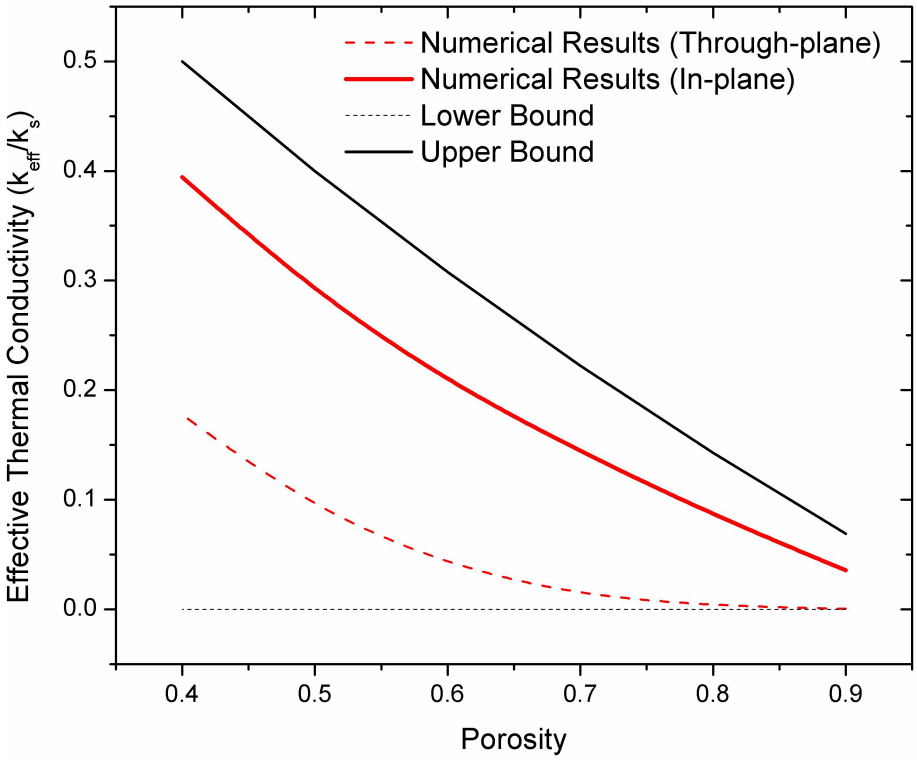

Figure 6.7: Effect of porosity on the effective thermal conductivity of carbon paper - no binder added - lower and upper bounds are also shown in the figure.

where A, B and C are fitting parameters.

It should be pointed out here that the correlations given in Equation (6.9) should be capable of estimating the effective thermal conductivity for a porosity lower than 40%. Examining these correlations, it can be seen that the ratio $\frac{k_{\text{eff}}}{k_{\text{s}}}$ is equal to 1 when the porosity of the GDL decreases to zero. In other words, the effective thermal conductivity is equal to the thermal conductivity of the solid fibers.

6.2.3 Proposed Correlation

Using the numerical results of the thermal conductivity, an expression for the through-plane and in-plane effective thermal conductivity for the porosity range $0.4 \leq \epsilon \leq 0.90$ is developed and the curve fit is illustrated in Figure 6.8. A very good agreement between the fitted results and the numerical results is shown. The values for A, B and C for the through-plane and in-plane directions are given in Table 6.2 along with the errors and the values of R^2.

Table 6.2: Fitting parameters for Equation (6.9) shown in Figure 6.8

Direction	**A**	**B**	**C**	R^2	**Validity Range**
Through-plane	0.963 ± 0.005	-0.008 ± 0.002	0.881 ± 0.008	0.999	$0.4 \leq \epsilon \leq 0.9$
In-plane	0.977 ± 0.002	-0.009 ± 0.00	0.344 ± 0.003	0.999	$0.4 \leq \epsilon \leq 0.9$

Hence, the through-plane and in-plane effective thermal conductivity of an uncompressed, dry carbon paper GDL with no Teflon treatment can be found as a function of its porosity using:

$$\frac{k_{\text{eff}}}{k_{\text{s}}} = \begin{cases} 1 - 0.963\,(1-\epsilon)^{-0.008} \exp\left[0.881\,(1-\epsilon)\right] \left[\dfrac{3\epsilon}{3-(1-\epsilon)}\right] & \text{through-plane direction} \\ 1 - 0.977\,(1-\epsilon)^{-0.009} \exp\left[0.344\,(1-\epsilon)\right] \left[\dfrac{3\epsilon}{3-(1-\epsilon)}\right] & \text{in-plane direction} \end{cases} \tag{6.9}$$

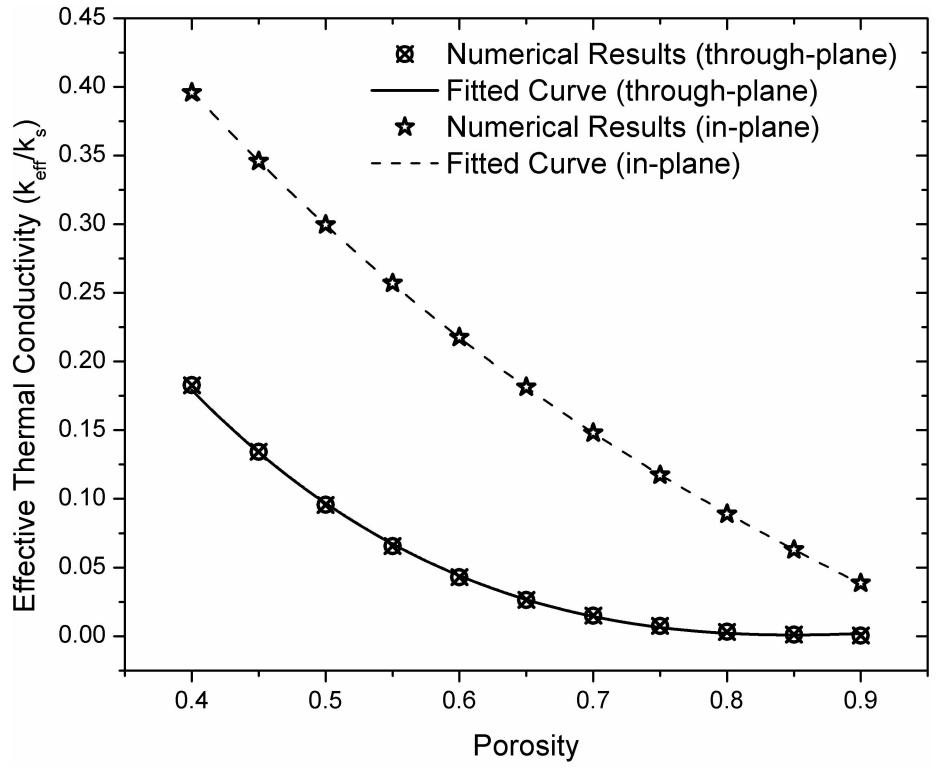

Figure 6.8: Comparison between the present numerical results and the curve fit from Equation (6.9) for the thermal conductivity in the through-plane and in-plane directions.

6.2.4 Estimating the Effect of Temperature and Compression on the Thermal Resistance between Fibers

The computational domain used in this thesis has been reconstructed based on the assumption that the fibers are in perfect contact. In other words, in the through-plane direction there exists no cracks between the fibers and hence the thermal resistance between the fibers is zero. However, in reality, cracks between in the carbon binder can form during manufacturing and will result in thermal contact resistance between the fibers. Hence, theoretically, the thermal conductivity of a porous medium can be represented as an average of the various mechanisms contributing to the heat transfer in the medium. In other words, the thermal conductivity of carbon paper can be written as a function of [174, 175]:

$$k_{\text{eff}} = M k_{\text{solid}} f_1(\epsilon) + k_{\text{gas}} f_2(\epsilon) + k_{\text{rad}} + k_{\text{conv}} \tag{6.10}$$

where M is a complicated function taking into account the heat barrier resistance between fibers in the materials and depends on the geometry of contact area and mismatch between grains and fibers [174, 175], k_{solid} and k_{gas} are the thermal conductivity of fibers and gas, respectively, $f_1(\epsilon)$ and $f_2(\epsilon)$ are functions taking into account the porous structure, porosity, and density of the material, k_{rad} is the heat radiation component of the apparent thermal conductivity, k_{conv} is the convection component of the apparent thermal conductivity. In this thesis, the contribution of the gas, radiation and convection to the overall thermal conductivity is negligible; hence, the thermal conductivity can be written as:

$$k_{\text{eff}} = M k_{\text{solid}} f_1(\epsilon) \tag{6.11}$$

where the value of the heat barrier resistance coefficient, M, is dependent on the resistances of the crack and the contact layer of inter-grain material, the micro crack thickness, the distance between the micro cracks and the effective radii of the contact area and of the grain boundary. The variation in the value of M can be influenced by the micro- and nano- cracks between the fibers. The change of the area between grains could lead to the change during the heating of the carbon paper sample and can explain the decrease and increase in the thermal conductivity of the sample under deformation.

In order to estimate the contact resistance coefficient, M, the function f_1, the solid conductivity and the through-plane effective thermal conductivity are needed. As mentioned earlier, the proposed correlation of this thesis, which is given by Equation (6.9), has been obtained under the assumption of perfect contact. Hence, the function $f_1(\epsilon)$ will take on

the following form:

$$f_1(\epsilon) = 1 - 0.963\,(1-\epsilon)^{-0.008} \exp\left[0.881\,(1-\epsilon)\right] \left[\frac{3\epsilon}{3-(1-\epsilon)}\right] \tag{6.12}$$

The thermal conductivity of the solid fibers can be estimated using the in-plane thermal conductivity measurements of this thesis. Using the experimental measurements presented earlier in this thesis, an empirical correlation for the in-plane thermal conductivity for the untreated carbon paper sample was found and and is written as:

$$k_{\text{eff}}^{\text{in}} = -7.166 \times 10^{-6} T^3 + 2.24 \times 10^{-3} T^2 - 0.237T + 20.1 \tag{6.13}$$

where T is the temperature in degrees Celsius, $k_{\text{eff}}^{\text{in}}$ is the in-plane thermal conductivity in $W/m.K$ and $R^2 = 0.9864$.

In the in-plane direction, the resistance to heat transfer in the in-plane direction is very small; hence, the heat barrier resistance coefficient, M, is equal to 1. Using $M = 1$ and Equation (6.13), the thermal conductivity of the carbon fibers, k_{solid} can be estimated as:

$$k_{\text{solid}} = \frac{(-7.166 \times 10^{-6} T^3 + 2.24 \times 10^{-3} T^2 - 0.237T + 20.1)}{0.10006} \tag{6.14}$$

where 0.10006 is the estimate of the ratio $\dfrac{k_{\text{eff}}^{\text{in}}}{k_{\text{solid}}}$ for the untreated, uncompressed sample used for the measurements of the in-plane thermal conductivity and is $78\% \pm 2.0\%$.

Using Equations (6.12) and (6.14), the heat barrier resistance in the through-plane direction for the untreated sample can be estimated for both deformation levels as given in Figure 6.9.

It is important to note here that the comparison made earlier in Figure 6.6 between the numerical and experimental results of this thesis was for the temperature range of +20 to $+120°C$. This is mainly due to the fact that the heat barrier resistance coefficient in this temperature range is approximately 1. In other words, in this temperature range, there exists strong contact between the fibers and the resistance due to cracks is almost negligible. Further, from Figure 6.9, it is interesting observe that M is smaller under low deformation. This is mainly due to the higher resistance between fibers.

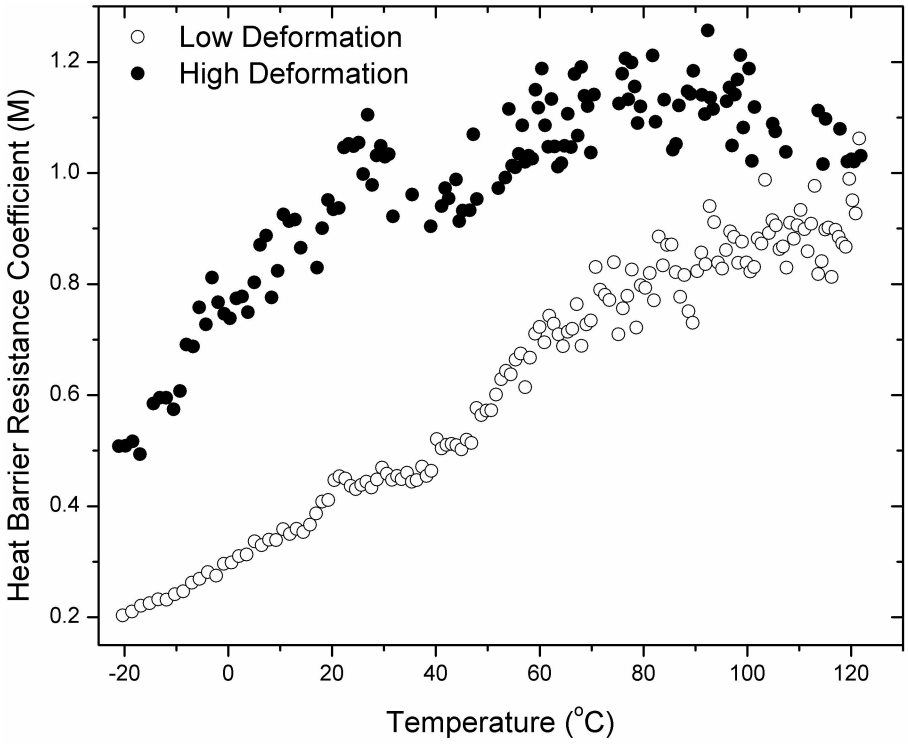

Figure 6.9: Effect of temperature and deformation level on the heat barrier resistance coefficient, M

6.3 Electrical Conductivity

6.3.1 Comparison to Experimental Measurements

Experimental measurements of the effective electrical conductivity of carbon paper is scarce. The most comprehensive set of data to-date is that by Nitta et al. [68]. They measured the in-plane and through-plane effective electrical conductivity of SIGRACET 10-BA manufactured by SGL Carbon Group. Its open porosity is 88% and it was treated with 5 wt.% PTFE for wet proofing and had no microporous layer. Their measurements were made under various compression pressure; hence, they obtained a set of values for a porosity range $0.7 \leq \epsilon \leq 0.88$. Other common measurements found in literature are for TORAY carbon paper and SGL carbon paper with no Teflon treatment and no microporous layer. The open porosity for TORAY carbon paper is 78%, while it is 88% for SGL carbon paper. Due to the limited available experimental data, the numerical results of this thesis were compared to the data set by Nitta et al. [68] and the available measurements for TORAY and SGL carbon paper made available by their manufacturers [91, 92] as shown in Figure 6.10. In order to make

this comparison, the electrical conductivity of solid carbon was taken as 150,000 Sm^{-1}. The electrical resistivity of carbon is in the range $5 \times 10^{-6} \leq \kappa_{\text{solid}} \leq 30 \times 10^{-6}$ [135]. The numerical results of the through-plane electrical conductivity have a good agreement with the experimental data. This is also the case for the in-plane electrical conductivity. However, there is a big difference between the in-plane effective electrical conductivity reported by Nitta et al. [68] and the numerical values. This difference could be attributed to the physical and structural properties between the GDL used by Nitta et al. and that reconstructed in this thesis.

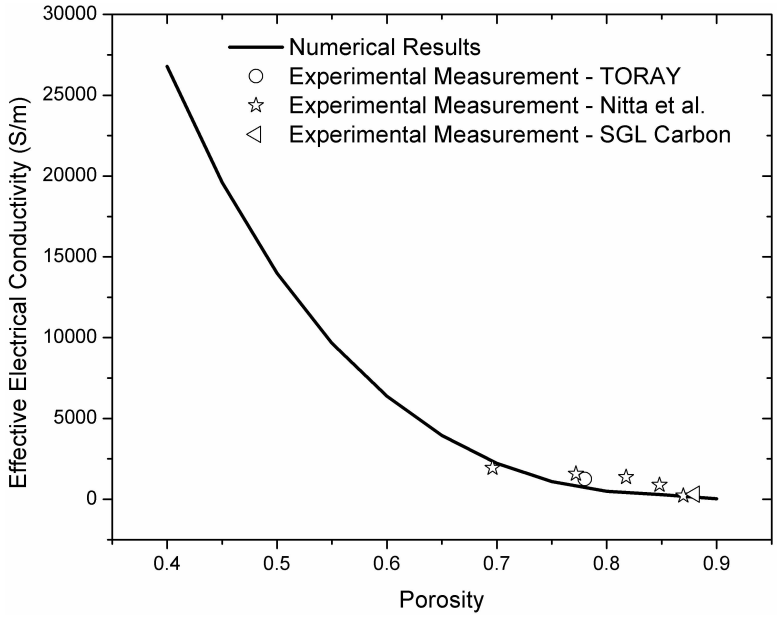

(a)

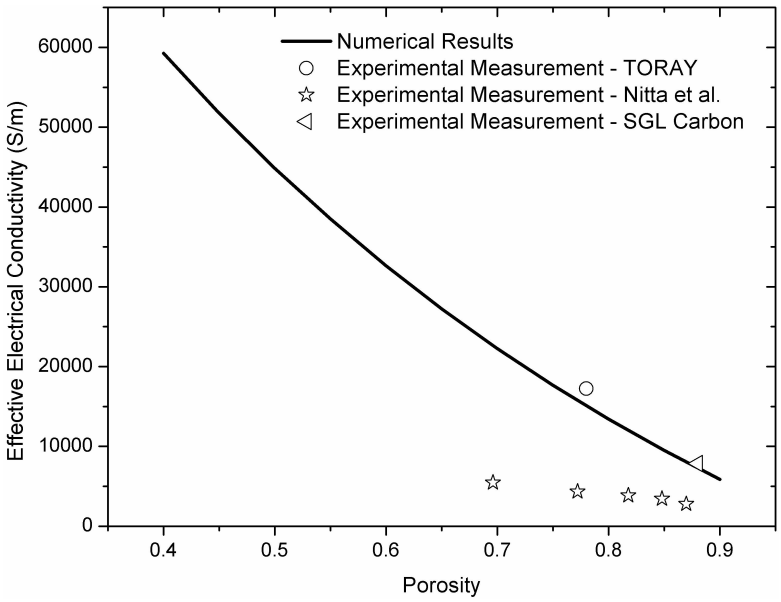

(b)

Figure 6.10: Comparison between numerical results and available experimental data in the (a) through-plane direction; (b) in-plane direction

6.3.2 Comparison to Theoretical Approximations

A comparison between the numerical results of the effective electrical conductivity found in this thesis and that estimated with the theoretical approximations discussed earlier in Equations (2.28), (2.29) and (2.31) was carried out as illustrated in Figure 6.11. It is interesting to note that the Bruggeman Approximation (Equation (2.28)) and the correlation by Das et al. (Equation (2.31)) seem to give an approximation for the in-plane effective electrical conductivity. In fact, the numerical results of this thesis and the results approximated by the Bruggeman Approximation have a very good agreement for high porosity values. In a similar fashion, the approximation given by Looyenga in Equation (2.29) can be used to estimate the through-plane effective electrical conductivity at high porosity values. Studying the correlations in Equations (2.28) and (2.29), it could be argued that the Bruggeman Approximation can be used to estimate the in-plane effective electrical conductivity and the approximation by Looyenga can be used to estimate the through-plane conductivity.

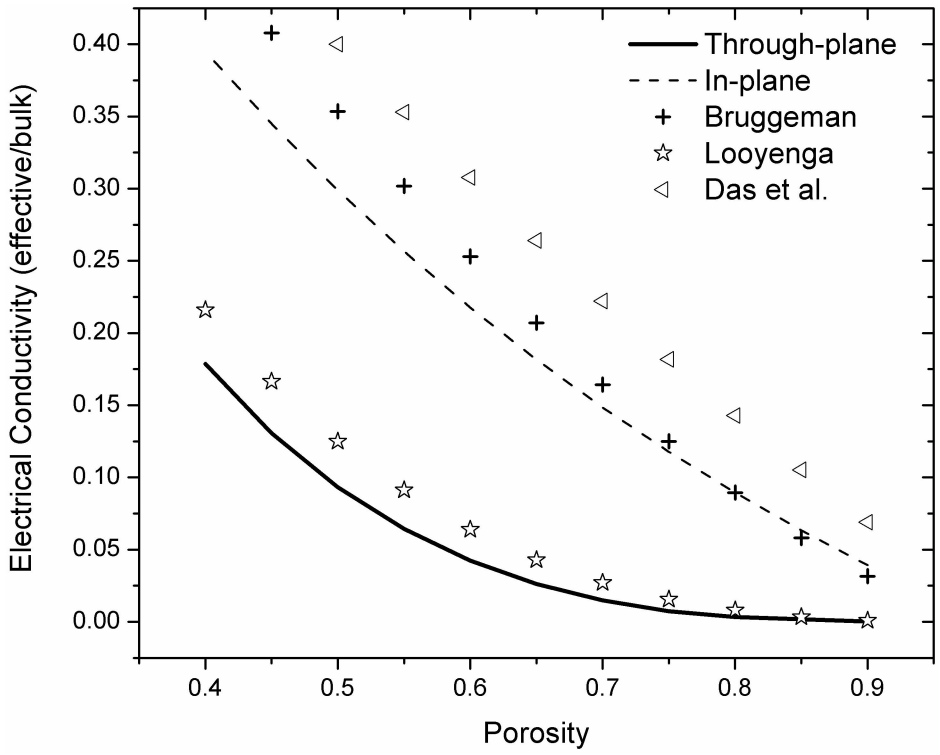

Figure 6.11: Through-plane and in-plane effective electrical conductivity for carbon paper - Numerical results and theoretical estimates using approximations by Bruggeman [36], Looyenga [96] and Das et al. [48]

6.3.3 Proposed Correlation

The comparison made between the numerical values and theoretical values for the effective electrical conductivity in the carbon paper GDL raises the need to find an alternative correlation. The expression found by Das et al. [48] provides the upper bound for the effective electrical conductivity. This upper bound is formulated for porous media with spherical particles without taking into account certain statistical parameters of the random geometry [39]. Hence, Das et al. [48] suggested that the statistical randomness of the geometry as well as the structure of the solid matrix can be taken into account by introducing a structural function $f(\epsilon)$ as follows:

$$\kappa_{\text{eff}} = \kappa_{\text{solid}} - f(\epsilon)\frac{3\epsilon\kappa_{\text{solid}}}{2+\epsilon} \tag{6.15}$$

where $f(\epsilon) \geq 0$ and could vary depending on the geometry of the solid matrix.

Using the upper bound suggested by Das et al. [48], the effective electrical conductivity for the carbon paper GDL is found using the structural function $f(\epsilon)$:

$$f(\epsilon) = A\exp\left[B(1-\epsilon)\right](1-\epsilon)^C \tag{6.16}$$

where A, B and C are fitting parameters. Thus, curve fit to be used for the in-plane and through-plane electrical conductivity is:

$$\frac{\kappa_{\text{eff}}}{\kappa_{\text{solid}}} = 1 - \left[\frac{3\epsilon}{2+\epsilon}\right] A\exp\left[B(1-\epsilon)\right](1-\epsilon)^C \tag{6.17}$$

The numerical results of the through-plane and in-plane effective electrical conductivity were curve fit using Equation (6.17). The curve fit for the porosity range $0.4 \leq \epsilon < 0.9$ is illustrated in Figure 6.12. A very good agreement between the fitted results and the numerical results is shown. The values for A, ϵ_p and β for the through-plane and in-plane directions are given in Table 6.17 along with the errors and the values of R^2.

Table 6.3: Fitting parameters for Equation (6.17) shown in Figure 6.12

Direction	**A**	**B**	**C**	R^2
Through-plane	0.962 ± 0.01	0.889 ± 0.015	-0.00715 ± 0.005	0.999
In-plane	0.962 ± 0.004	0.367 ± 0.005	-0.016 ± 0.002	0.999

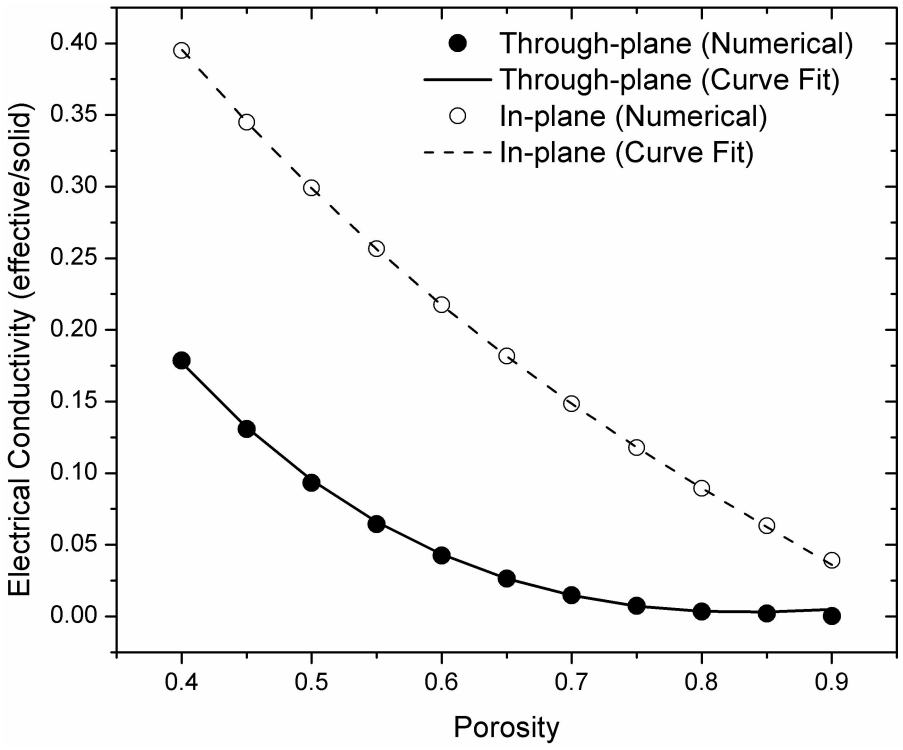

Figure 6.12: Comparison between the present numerical results and the curve fit from equation (6.17) for the electrical conductivity in the through-plane and in-plane directions

6.4 Effect of Structure on Properties

In this section, the effect of the distribution of fibers on the overall effective properties of a porous medium is investigated. The transport properties of the porous structures described earlier in Section 4.1.1 are compared against the transport properties of the carbon paper GDL. Here, the objective is to emphasize the effect of the fiber distribution on the overall transport properties of a porous medium. The diffusibility of gases through the three structures, true, isotropic and fibers is given in Figure 6.13. As it can be seen, the anisotropic nature of the two structures, true and fibers, leads to a difference between their respective in-plane and through-plane diffusibility.

Due to the high thermal conductivity of carbon compared to air, the fiber distribution is expected to play a significant role in determining the effective thermal conductivity of the porous medium. A comparison between the thermal conductivity of the true geometry and the other two geometries is given in Figure 6.14. It is interesting to note that the anisotropy of the carbon paper results in the decrease of its overall thermal conductivity when compared to the isotropic carbon paper. The in-plane and through-plane thermal conductivity of the

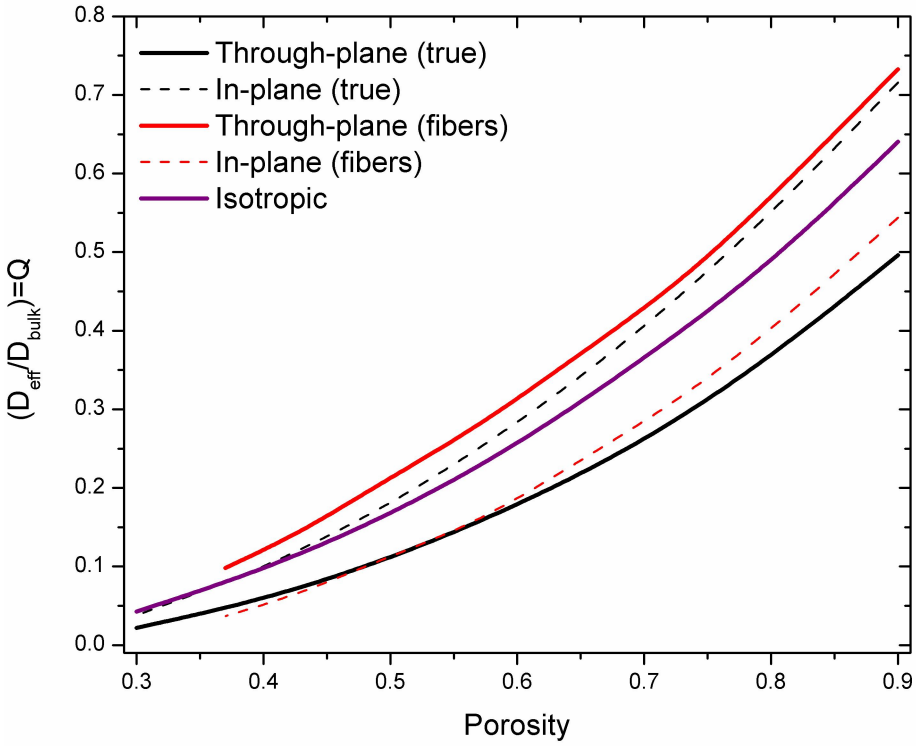

Figure 6.13: Dependence of the diffusibility of gases on the fiber distribution of the porous structure

isotropic material are the same. Thus, it is expected that the temperature distribution in this type of material would be uniform in all directions. In order to increase the overall thermal conductivity of the anisotropic carbon paper, fibers are embedded through the thickness of the paper. These fibers result in the increase of the through-plane thermal conductivity of the structure. It is also obvious that the through-plane thermal conductivity of the "fibers" domain is the highest amongst all three structures since the embedded fibers are perpendicular to the through-plane and provide a direct and easy pathway for the heat to be transferred. In fact, the through-plane thermal conductivity of this structure is higher than its in-plane. However, the difference between the thermal conductivity in both directions is not as high as that for the anisotropic carbon paper. Thus, it can be concluded that the addition of fibers to carbon paper increases the overall thermal conductivity of carbon paper. The same trend is observed for the electrical conductivity as shown in Figure 6.15. This is so since heat is conducted mainly through the fibers.

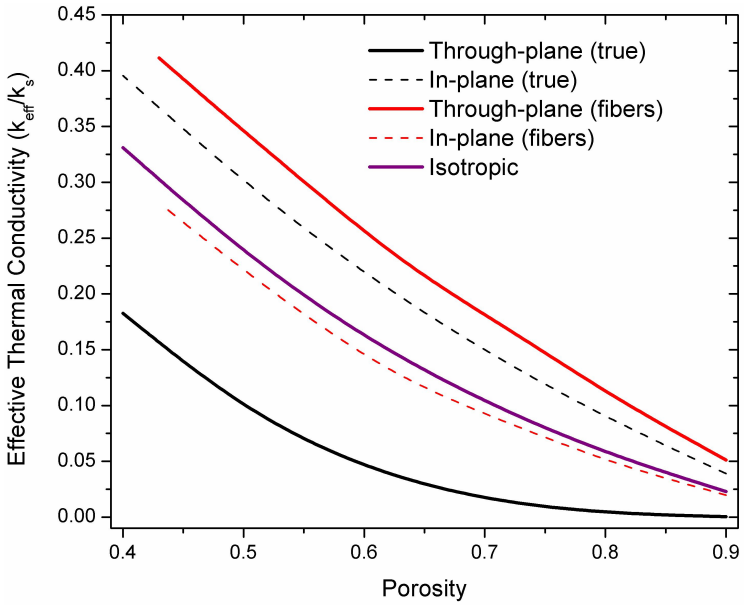

Figure 6.14: Dependence of the thermal conductivity on the fiber distribution of the porous structure

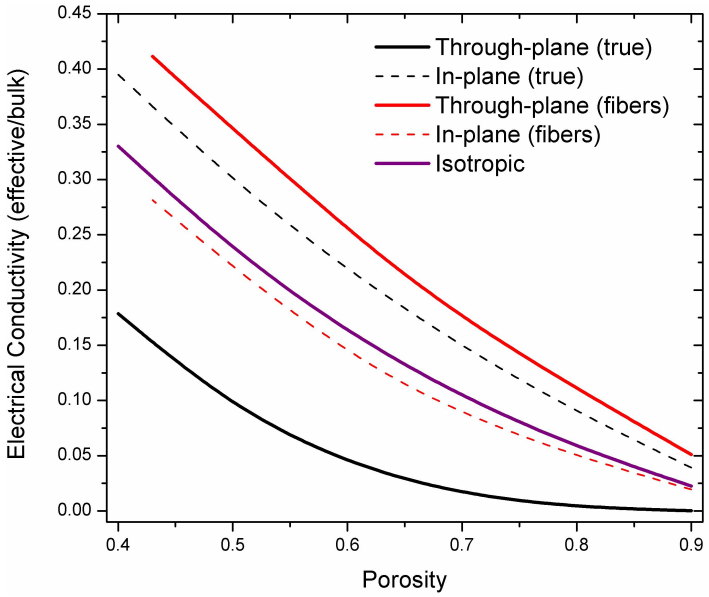

Figure 6.15: Dependence of the electrical conductivity on the fiber distribution of the porous structure

6.5 Chapter Summary

In this chapter, numerical simulation of the diffusion, heat conduction and electrical conduction processes using the real three-dimensional pore morphology of a the gas diffusion layer

of PEM fuel cells were used to estimate the effective properties. The estimation is based on the assumption that the GDL is dry; in other words, the effect of liquid water is not taken into consideration. The effective properties (diffusion coefficient, thermal conductivity and electrical conductivity) in both the in-plane and through-plane directions were determined. In order to establish the validity of the numerical procedure, the numerical results of this thesis are compared against published experimental data and a good agreement was found to exist. Further, the comparison between the numerical results and existing correlations showed that the latter do not accurately predict the effective properties of the carbon paper GDL. This is mainly due to the fact that the existing correlations have not been developed using the porous structure of the carbon paper GDL. Finally, using the numerical results of this thesis, correlations for the in-plane and through-plane effective diffusion coefficient, thermal conductivity and electrical conductivity were proposed.

Chapter 7

Results and Discussion – Numerical – Wet GDL

Multi-phase modeling is of particular importance in the study of polymer electrolyte membrane fuel cells due to the presence of water. Water is usually supplied to the cell through humidification of the fuel and oxidants. Further, it is the product of the electrochemical reaction in the cell. In the membrane, water exists in the dissolved phase; in the catalyst layer it is found in the dissolved, liquid and vapor phases and in the gas diffusion layer (GDL) it takes the form of vapor or liquid. Hydration of the ionomer/membrane is important since water is needed for proton transfer to/from the reaction sites. However, excess liquid water in the GDL can hinder the overall performance of the cell. Hence, understanding the effect of water presence in the liquid form on the transport properties of the GDL is very crucial to simulating transport phenomena.

In the gas diffusion layer, the effects of liquid water on the relative permeability, capillary pressure, diffusion coefficient and thermal conductivity are of particular interest. The permeability is a measure for the amount of convective mass transfer, which occurs in the GDL. Mass transfer through convection becomes very crucial depending on the flow channel design. The effect of permeability on such a phenomenon for serpentine channels was studied in [89, 64]. In the presence of liquid water, the relative permeability is needed to estimate the phase pressures of the gas and liquid phases. The phase pressures are related to the capillary pressure, which is an indicator for the flow of liquid water inside the gas diffusion layer. Diffusion of gases in the GDL is another important transport property since it governs the ability of the reactants to reach the reaction sites; hence, diffusion affects the overall reaction rate of the cell. In the presence of liquid water, this diffusion process could be hindered and so it is necessary to investigate the extent of its impact. Finally, heat

transfer in the GDL could be affected by the presence of liquid water. Liquid water could play a role in connecting the solid fibers; thus, reducing the overall heat barrier resistance and increasing the overall thermal conductivity of the GDL. The results presented in this chapter are presented in the journal article [171].

7.1 Relative Permeability

As mentioned earlier, the permeability is a measure of the mass transport through mass convection. The effect of permeability on this transport phenomenon depends on the design of the gas channels. In serpentine channels, this effect is very much highlighted as shown in [176]. To be able to investigate the relative permeability, the evaluation of the intrinsic permeability is needed. The effect of the porosity of the dry GDL on the in-plane and through-plane intrinsic permeability is given in Figure 7.1. As expected, the permeability decreases with the decrease of porosity and the permeability is higher in the in-plane direction than the through-plane. This implies that the movement of the gas phase in the GDL slows down as the porosity decreases, which is mainly due to the reduced pore area available for transport of gases.

Although the relative permeability is very much dependent on its intrinsic counterpart, it was found that the relative permeability is independent of the direction as shown in Figure 7.2. By definition, the relative permeability is the ratio of the permeability of the phase at a given saturation level to the intrinsic permeability of the GDL at a given porosity ($\kappa_{\text{rk}} = \frac{\kappa_k}{K}$). The phase permeability, κ_k, is a function of the porosity of the GDL and the saturation of phase k and the intrinsic permeability, K, is a function of the porosity. This is due to the fact that the available number of pores for the flow to occur is the same regardless of the direction. The numerical results of this thesis were compared against experimental data by [113, 172, 173]. Experimental data of the liquid phase relative permeability are not yet to be available in literature. Hence, the available experimental data of the gas phase relative permeability are used for comparison reason. As it can be seen, the experimental results of Nguyen et al. [113] and Koido et al. [173] compare very well with the numerical results of this thesis. In the study by Nguyen et al. [113] the relative permeability of the gas phase was obtained for SIGRACET 10BA from SGL Carbon with 5 wt.% Teflon by submerging the carbon paper into liquid water and calculating the capillary head. The liquid water distribution was obtained using neutron imaging. The measurements by Koido et al. [173] were obtained using TORAY-TPG-H-060, which is a carbon paper composed of straight long fibers with no Teflon treatment. The differences between the numerical and

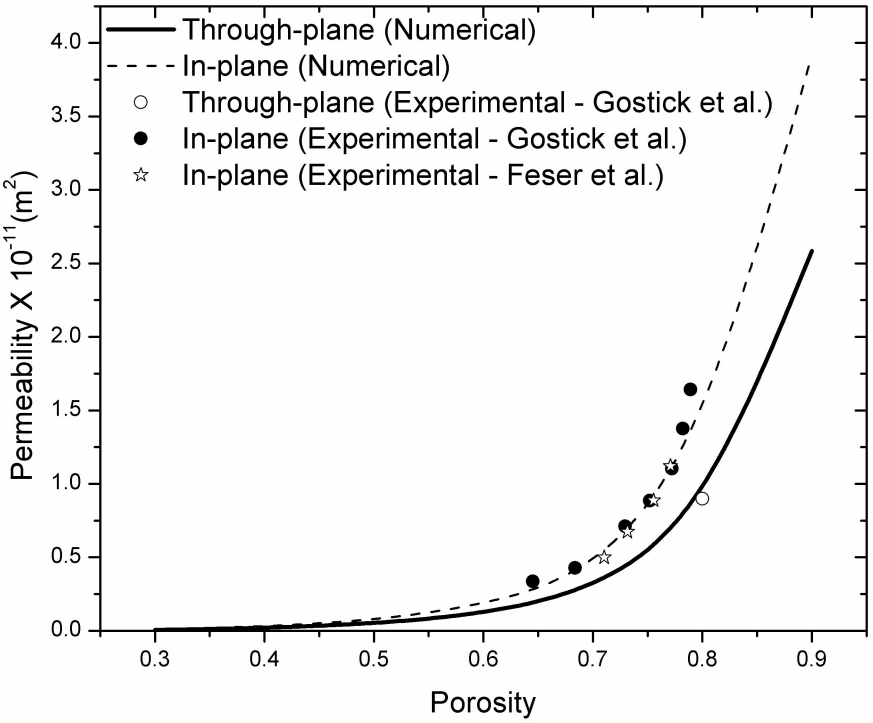

Figure 7.1: In-plane and through-plane permeability of a dry GDL - experimental data obtained from [100, 99].

experimental results may arise from various sources, such as reconstruction of the carbon paper, idealization of the liquid water droplet in the numerical model and uncertainty of the liquid water saturation in the experimental methods. Nonetheless, the numerical results compare well with the measurements from [113, 173]. The numerical results, however, do not compare as well with the experimental data by Owejan et al. [172]. This discrepancy can be mainly due to the method of data collection. The permeability of the cathode gas diffusion layer in [172] was calculated for an operating fuel cell using the flow rate and pressure differential of the cell. The liquid water saturation was obtained using neutron imaging techniques. Hence, many factors, such as non-uniform compression of the gas diffusion layer, could have an effect on both the structure of the GDL and the dispersion of the liquid water in the pores. Although the studies by Nguyen et al. [113] and Owejan et al. [172] both use the neutron imaging technique to obtain the liquid water saturation, the results of both studies deviate from each other. This deviation could be attributed to the difference in data collection and liquid water introduction in both studies. Finally, in their study, Owejan et al. [172] suggested that the gas permeability reaches zero once the cathode GDL void is over 0.5 full of liquid water. This implies that at a saturation of 0.5, the gas is no longer

mobile since water blocks the available pores for gas transport. Visiting the experimental results by Nguyen et al. [113] and Koido et al. [173], the saturation level at which the gas phase is immobile, is higher than 0.5. Extrapolating the data by Koido et al. [173], it can be seen that the relative permeability of the gas phase reaches zero between 0.6-0.7 saturation, which is in agreement with the present numerical data.

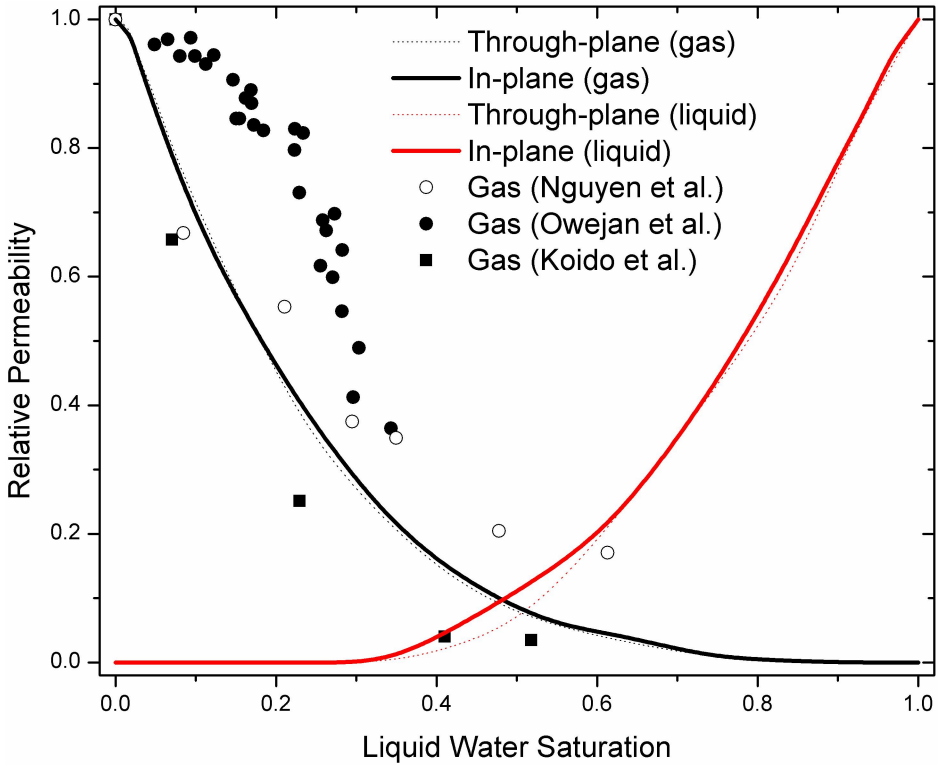

Figure 7.2: Relative permeability of liquid and gas phases in the carbon paper GDL - experimental data obtained from [113, 172, 173]

The numerical results obtained in this thesis for the relative permeability were used to obtain an understanding of the applicability of estimating the relative permeability using the VG model, the BC model and the power law given in Equations (7.1), (7.2) and (7.3), respectively; as given in Figure 7.3. The numerical results are fitted to these three expressions and it can be seen that both the VG model and the power law are in good agreement with the numerical results.

van Genuchten model:

$$\kappa_{\mathrm{rg}} = (1 - s_{\mathrm{l}})^{\eta_g} \left[1 - \left(1 - (1 - s_{\mathrm{l}})^{1/m}\right)^{m}\right]^{2} \qquad \kappa_{\mathrm{rl}} = (s_{\mathrm{l}})^{\eta_l} \left(1 - (1 - s_{\mathrm{l}})^{1/m}\right)^{2m} \tag{7.1}$$

where $m = 0.8$, $\eta_g = 0.5$ and $\eta_l = 2$. It is interesting to note here the difference between η_g and η_l. By definition, these two variables describe the flow path of their respective fluids, gas and liquid. The magnitude of these two variables implies that the resistance to the flow of the gas phase in the porous GDL is smaller than that of the liquid phase. This resistance mainly arises due to the difficulty of liquid water penetration through the pores of the GDL. Brooks-Corey model:

$$\kappa_{\mathrm{rg}} = (1 - s_{\mathrm{l}})^{3+2/\lambda} \qquad \kappa_{\mathrm{rl}} = s_{\mathrm{l}}^2 \left(1 - (1 - s_{\mathrm{l}})^{1+2/\lambda}\right) \tag{7.2}$$

where $\lambda = 3$.

Power law:

$$\kappa_{\mathrm{rl}} = s_{\mathrm{l}}^n \qquad \kappa_{\mathrm{rg}} = (1 - s_{\mathrm{l}})^n \tag{7.3}$$

where $n = 3.5$.

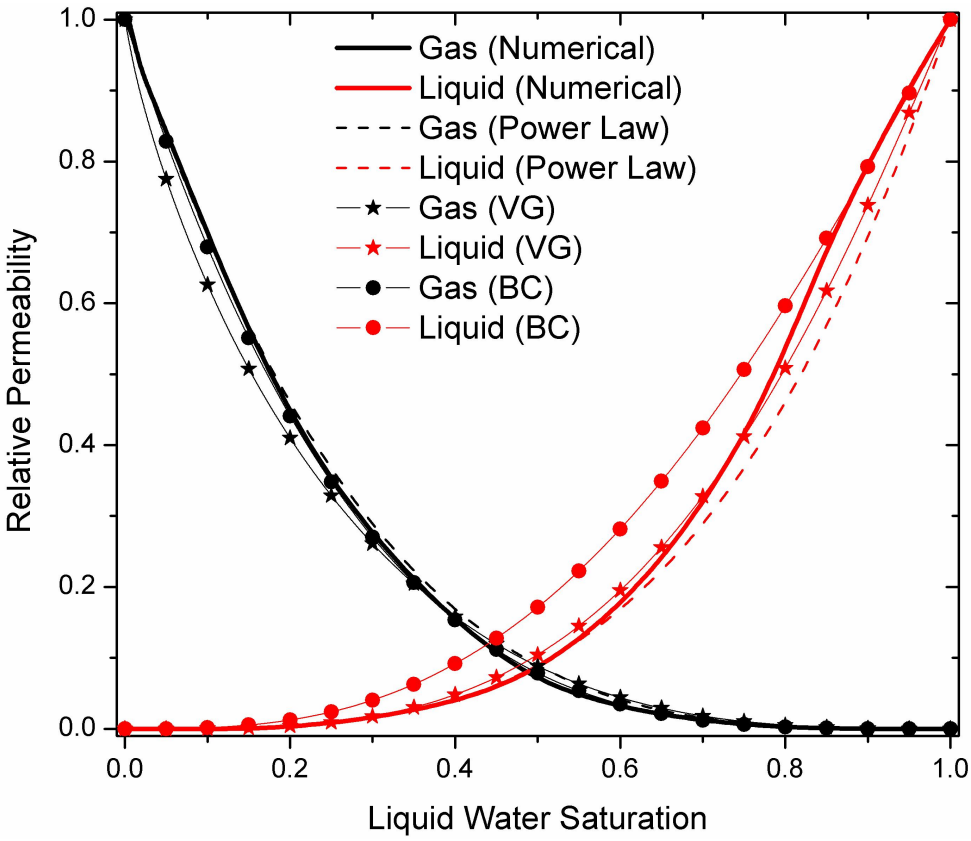

Figure 7.3: Relative permeability of liquid and gas phases in the carbon paper GDL versus the VG and BC models and the power law given in Equations (7.1), (7.2) and (7.3), respectively

Using the relative permeability results, another parameter that can be investigated is the mobility of the phases. The mobility of the phase in the GDL is a measure of its ability to move in the pore space. The mobility of the liquid and gas phases is shown in Figure 7.4. The liquid mobility, λ_l is defined as:

$$\lambda_l = \frac{k_{rl}/\upsilon_l}{k_{rl}/\upsilon_l + k_{rg}/\upsilon_g} \tag{7.4}$$

where υ is the kinematic viscosity. The gas phase mobility, λ_g can be found as:

$$\lambda_g = 1 - \lambda_l \tag{7.5}$$

The liquid phase is found to be immobile for liquid water saturations less than 0.1. This implies that a residual liquid water saturation exists at this saturation level. The gas phase, is found to be immobile once the liquid water saturation reaches 0.7. This implies that the pores available for gas transport become blocked by liquid water. The mobility curves of the liquid and gas phases intersect at a saturation of 0.31. This intersection implies that neither phase is competing for pores at this saturation level.

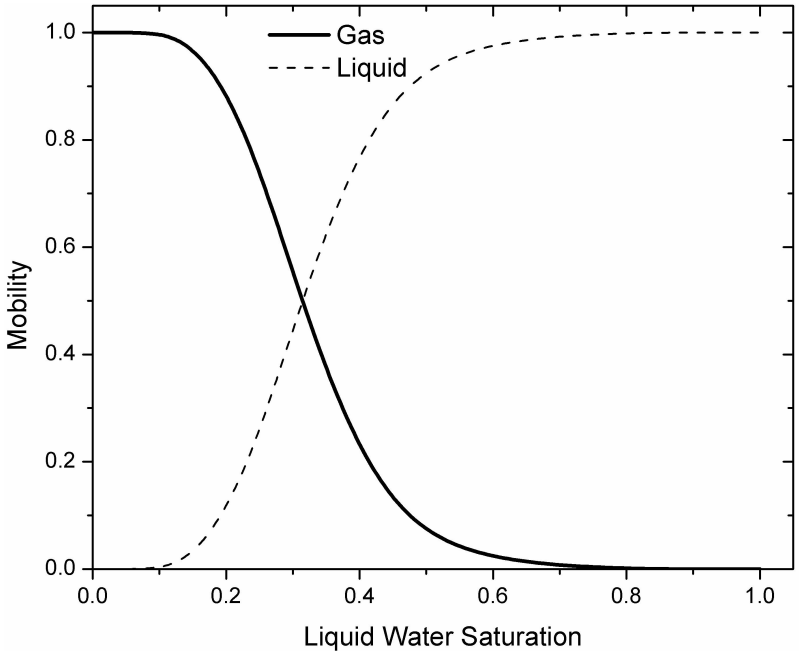

Figure 7.4: Mobility of gas and liquid phases

7.2 Capillary Pressure

Similar to the relative permeability, the capillary pressure is another quantitative measure of the transport of liquid water in the gas diffusion layer. The relative permeability is related to the convective transport of the phases (liquid and gas in this case) and the capillary pressure is related to the diffusive transport of liquid water since the liquid water diffusion coefficient is defined in terms of the capillary pressure. In this thesis, the numerical technique described earlier is used to obtain the capillary pressure as a function of the liquid water saturation and is then compared to experimental data obtained using the MSP as given in Figure 7.5. As it can be seen, a good agreement between the numerical and experimental results exist. It should be pointed out here that the experimental results give the capillary pressure as a function of the total porosity of the carbon paper GDL; i.e. it takes into account the hydrophilic and the hydrophobic pores, since octane fully wets the GDL. Finally, as it can be seen, the Leverett function underestimates the capillary pressure. However, the slope of the curve of this function is very close to the slope of the numerical results. Hence, the Leverett function can be used to characterize the capillary pressure in terms of the liquid water saturation in the gas diffusion layer. However, a correction factor should be used in order to improve its estimate. The van Genuchten (VG) model (Equation (2.45)) and the Brooks-Corey equation (Equation (4.1)) were used to correlate the numerical results of this study. From Figure 7.5, it can be seen that the numerical results of the capillary pressure are better correlated with the VG model than with the BC model. The fitting parameters for the VG model, P_{cb}, n and m, are found to be 0.0856 bar, 5 and 0.8, respectively. Similarly, the fitting parameters for the BC equation, P_{cb} and λ, are found to be 0.075 bar and 3, respectively.

7.3 Diffusion Coefficient

The diffusion coefficient of the carbon paper GDL for different saturation levels has been estimated numerically. According to the theoretical expressions given earlier in Equations (2.12), (2.18) and (2.20), the presence of liquid water in the GDL decreases the diffusion coefficient. This effect can be modeled by the reduction of the pores available for diffusion (i.e. the porosity of the GDL decreases). This assumption stands since the diffusion coefficient of gases in liquid water is very small compared to their respective diffusion coefficient in the pore space. For instance, at $20°C$, the diffusion coefficient of an oxygen in nitrogen and in liquid water is 0.219 and 1.97×10^{-5} cm^2/s, respectively. Using the numerical scheme

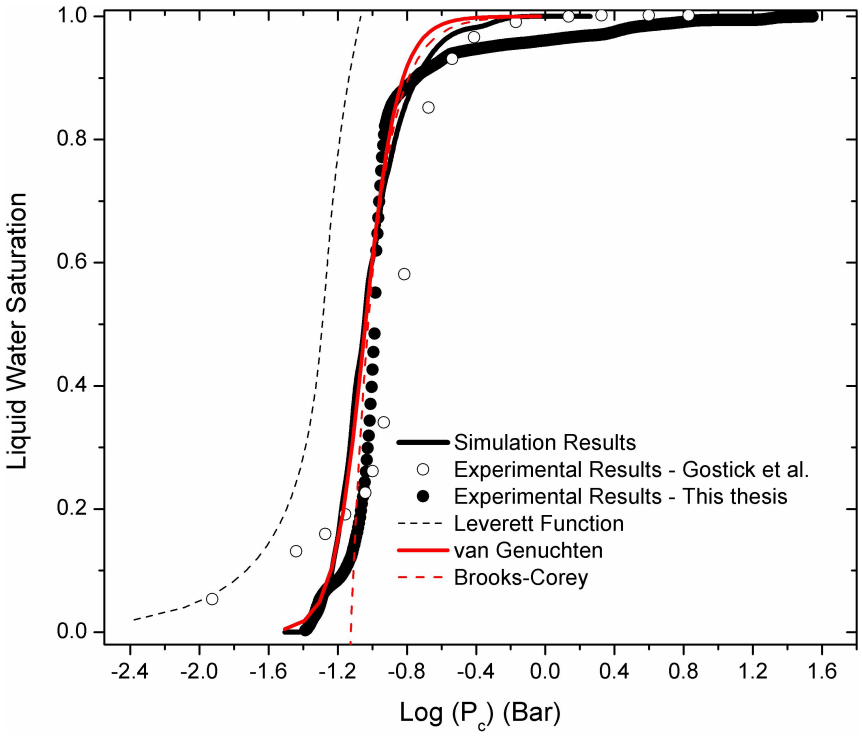

Figure 7.5: Capillary pressure from simulations compared to experimental data of this thesis and the study by Gostick et al. [114], the Leverett Function, the VG Model and the BC Model

described above, this assumption is shown to be valid as seen in Figure 7.6. The porosity in this figure takes into account the presence of liquid water. Due to the presence of liquid water, the available pore volume (in other words the porosity) can be expressed as follows:

$$\epsilon_{\text{wet}} = \epsilon_{\text{dry}} (1 - s) \tag{7.6}$$

7.4 Thermal Conductivity

The thermal conductivity of the carbon paper in the presence of liquid water was also evaluated in this thesis. As it can be seen from Figure 7.7(a), the thermal conductivity of the carbon paper increases as liquid water saturation increases. It is interesting to note that the effect of liquid water on the through-plane thermal conductivity is much more exaggerated. The through-plane thermal conductivity is increased by up to 3 times once the GDL is fully saturated, while a 5% increase is seen in case of the in-plane thermal

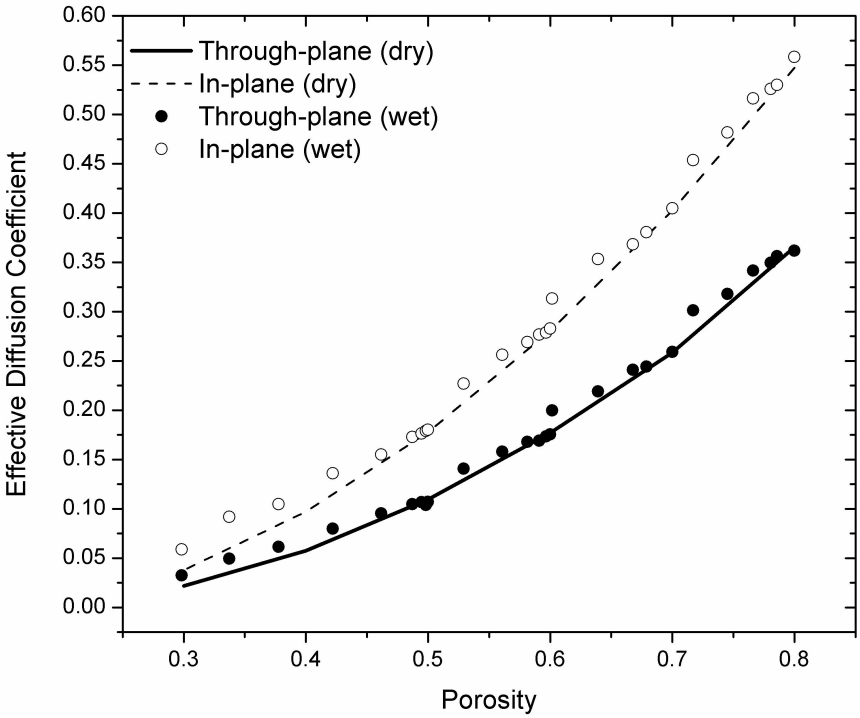

Figure 7.6: Effect of liquid water on the diffusion of gases in the GDL

conductivity. This difference is attributed to the distribution and alignment of the carbon fibers in both directions. The liquid water decreases the thermal resistance between the fibers in the through-plane direction and hence assists with the heat conduction. In the in-plane direction, the heat is easily conducted through the solid fibers. Further, it is important to note that for PEM fuel cell application, once the saturation level of liquid water reaches approximately 40%, the cell would be nearing is limiting current. At this saturation level, the effect of liquid water on the thermal conductivity is minimal.

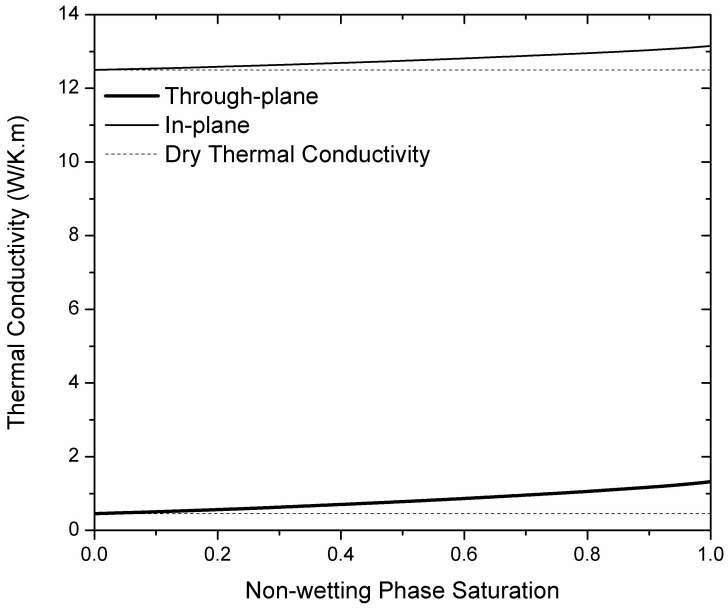

(a)

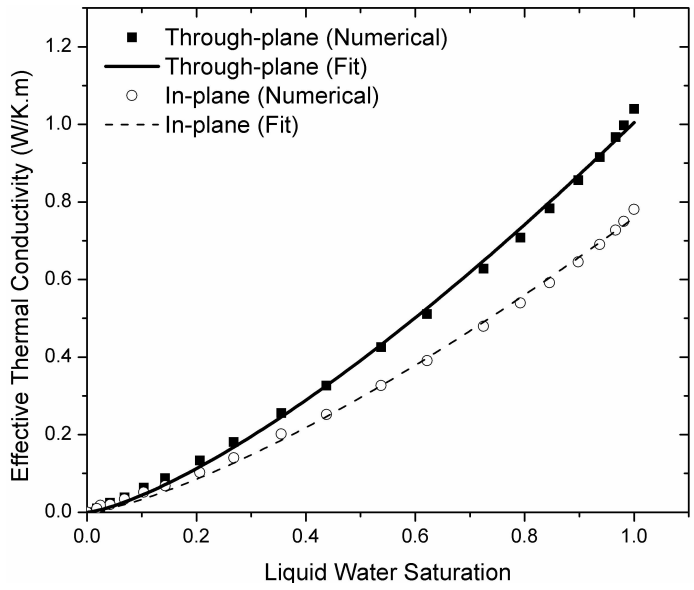

(b)

Figure 7.7: (a) Effect of liquid water on the thermal conductivity of the GDL; (b) Comparison between numerical and fit results

Experimental data of the effect of liquid water on the thermal conductivity is scarce. However, Burheim et al. [69] measured the through-plane thermal conductivity of carbon paper under various degrees of compression and for a liquid water saturation of 0.26. They found that for a porosity of 0.80 and a liquid water saturation level of 0.26, the thermal conductivity is 0.57 ± 0.06 $W/K.m$. This result is in good agreement with the numerical result of 0.601 $W/K.m$.

Using the numerical results of this thesis, the effective thermal conductivity of the GDL in the presence of liquid water can be written as an average as follows:

$$k_{\text{eff}}^{\text{liquid}} = k_{\text{eff}}^{\text{dry}} + k_l \left(As\right)^{\alpha} \tag{7.7}$$

where $k_{\text{eff}}^{\text{dry}}$ is the effective thermal conductivity of the dry carbon paper GDL, A is fitting parameter that takes into account heat resistance due to the presence of liquid water and α is an empirical exponent. A is found to be 1.43 ± 0.008 and 1.19 ± 0.008 for the through-plane and in-plane directions, respectively. α is 1.50 for both directions.

7.5 Summary of Chapter

A full morphology model was used to investigate the effects of liquid water presence on the transport properties of the gas diffusion layer of PEM fuel cells and to examine the capabilities of various approximations for the relative permeability, capillary pressure and diffusion coefficient. It was found that the power law with the third power gives a good estimate for the relative permeability of the liquid and gas phases. The applicability of the Leverett function to estimate the capillary pressure was also examined. It was shown that this function gives the correct slope; however, it underestimates the capillary pressure of the gas diffusion layer. The numerical results of the capillary pressure were compared against experimental data, which were obtained using the method of standard porosimetry. Further, liquid water in the GDL was shown to act as a barrier to the diffusion of gases and its presence directly affects the overall porosity of the layer. While liquid water hinders the diffusion of gases, it was found to reduce the thermal resistance between the solid fibers and hence increases the overall thermal conductivity of the layer. Its effects are more highlighted in the through-plane direction than in the in-plane direction due to the geometry of the layer. Finally, The effects of liquid water on the mobility of the phases was also investigated. Studying the mobility of the phases, which is related to the relative permeability, a residual liquid water saturation of 0.1 and a maximum saturation of 0.7 were found to exist.

Chapter 8

Concluding Remarks

With the complex and anisotropic structure of the carbon paper gas diffusion layer, there exists a need for a comprehensive understanding of its transport properties. In this thesis, various experimental techniques and a numerical model were employed to understand the structure of the GDL and to estimate its transport properties. Using SEM images and the method of standard porosimetry, the effect of Teflon on the overall structure of the carbon paper GDL was investigated. It was shown that the addition of PTFE to the carbon paper resulted in the decrease of the overall pore volume and increased its mechanical stability.

A Loschmidt cell was used to measure the through-plane effective diffusion coefficient in the carbon paper GDL. The effects of temperature and Teflon treatment on the overall diffusibility of the gas were investigated. It was found that the temperature does not affect the overall diffusibility of the gas. The main contributor to the mass resistance through diffusion was found to be the solid structure of the GDL. The addition of Teflon to carbon paper resulted in decreasing the overall porosity of the GDL; hence, decreasing the overall diffusibility of the gases in the layer. A comparison between the measured data and that predicted by the existing effective diffusion coefficient models indicated that these models overpredict the effective diffusion coefficient significantly. This over-prediction can lead to underestimating the mass transport limitations in the gas diffusion layer of PEM fuel cells, especially at high current densities and low porosity values.

The method of monotonous heating was used to measure both the in-plane and through-plane thermal conductivity of the thin carbon paper for a wide temperature range encountered in the practical application of PEM fuel cells. The in-plane thermal conductivity of carbon paper was measured for the temperature range from $-20°C$ to $+120°C$. It was found that the thermal conductivity decreases with an increase in temperature reaching an asymptotic value. The effect of Teflon on the conductivity was shown to dramatically decrease the

thermal conductivity at low temperatures. A phase change was shown to occur around $21°C$ and 35° degrees in samples with high Teflon loading (20 and 50 wt.%). For the three studied PTFE loadings, the in-plane thermal conductivity lies in the range of $10.1 - 14.7$ $(W/m.K)$. Further, the combined effect of temperature, deformation and PTFE loading on the through-plane thermal conductivity was investigated. An increase in the compression pressure was found to drastically increase the thermal conductivity of both treated and untreated carbon paper. This increase is mainly attributed to the decrease in the overall contact resistance between the carbon fibers. The addition of Teflon resulted in the decrease of the overall thermal conductivity. However, at high deformation levels, the thermal conductivity of both treated and untreated carbon paper was found to be approximately the same and to remain constant at temperatures higher than $35°C$. This temperature marks a phase change in the structure of pure PTFE.

Using a three-dimensional reconstruction of the pore morphology of the carbon paper GDL, the effective properties (diffusion coefficient, thermal conductivity, electrical conductivity, intrinsic and relative permeability and capillary pressure) were estimated under the dry condition and in the presence of liquid water. A good agreement between the numerical estimations and experimental data was shown throughout this thesis. The numerical results of the effective properties once again highlighted the inaccuracy of the available theoretical models in predicting the transport coefficients of the GDL. In the presence of liquid water, the relative permeability was shown to be independent of direction. This is mainly attributed to the overall number of available pores in both directions. Further, the numerical results were used to examine the capabilities of various approximations for the relative permeability and capillary pressure. The power law with an exponent of 3.5 was found to give a good estimate of the relative permeability of both phases. The van Genuchten model was also shown to give a good estimate for both the capillary pressure and the relative permeability. Further, the applicability of the Leverett function to estimate the capillary pressure was also examined. It was shown that the Leverett function underestimates the capillary pressure of the gas diffusion layer. The effect of liquid water on the diffusion process was also investigated. The presence of liquid water was shown to act as a barrier to the diffusion of gases and its presence directly affects the overall porosity of the layer. While liquid water hinders the diffusion of gases, it was found to reduce the thermal resistance between the solid fibers and hence increases the overall thermal conductivity of the layer. Its effects are more highlighted in the through-plane direction than in the in-plane direction due to the geometry of the layer. Finally, The effects of liquid water on the mobility of the phases was also investigated. Studying the mobility of the phases, which is related to the relative

permeability, a residual liquid water saturation of 0.1 and a maximum saturation of 0.7 were found to exist.

Finally, the numerical estimation and the experimental results of the through-plane thermal conductivity were used to investigate the thermal resistance due to cracks and gaps between fibers. It was found that both temperature and deformation significantly affect this thermal resistance. The resistance decreased with an increase in temperature, which is mainly attributed to the expansion of the solid carbon fibers and the increase in the thermal conductivity of the air trapped between the fibers. Further, compression was found to decrease this resistance. Once the carbon paper is compressed, the area of contact between the fibers is increased; hence, thermal resistance between fibers is decreased.

Using the experimental and numerical results of this thesis, theoretical and empirical relations for the various transport coefficients of the carbon paper GDL were developed. These relations are summarized in the next section.

8.1 Summary of Developed Theoretical and Empirical Relations

- The in-plane thermal diffusivity of untreated carbon paper can be related to the operating temperature as follows:

$$\alpha_{\text{apparent}} = -4.91 \times 10^{-11} T^3 + 1.42 \times 10^{-8} T^2 - 1.46 \times 10^{-6} T + 8.91 \times 10^{-5} \quad (8.1)$$

  where α_{apparent} is the thermal diffusivity and is given in m^2/s, T is the temperature in degrees Celsius and $R^2 = 0.993$. This relation is valid for a temperature range of -20 to $+120°C$.

- The in-plane thermal conductivity of untreated carbon paper can be related to the operating temperature as follows:

$$k_{\text{eff}}^{\text{in}} = -7.166 \times 10^{-6} T^3 + 2.24 \times 10^{-3} T^2 - 0.237 T + 20.1 \quad (8.2)$$

  where T is the temperature in degrees Celsius, $k_{\text{eff}}^{\text{in}}$ is the in-plane thermal conductivity in $W/m.K$ and $R^2 = 0.9864$. This relation is valid for a temperature range of -20 to $+120°C$.

- The through-plane and in-plane diffusion coefficient for untreated, dry carbon paper

GDL can be written in terms of the porosity as follows:

$$\frac{D_{\text{eff}}}{D_{\text{bulk}}} = \begin{cases} 1 - 2.76\epsilon \cosh\left(3\epsilon - 1.92\right)\left[\dfrac{3\left(1-\epsilon\right)}{3-\epsilon}\right] & \text{through-plane direction} \\ 1 - 1.72\epsilon \cosh\left(2.07\epsilon - 2.11\right)\left[\dfrac{3\left(1-\epsilon\right)}{3-\epsilon}\right] & \text{in-plane direction} \end{cases} \tag{8.3}$$

where this relation is valid for a porosity range $0.33 \leq \epsilon \leq 1$

- The through-plane and in-plane thermal conductivity for untreated, dry carbon paper GDL can be written in terms of the porosity as follows:

$$\frac{k_{\text{eff}}}{k_{\text{s}}} = \begin{cases} 1 - 0.963\left(1-\epsilon\right)^{-0.008} \exp\left[0.881\left(1-\epsilon\right)\right]\left[\dfrac{3\epsilon}{3-\left(1-\epsilon\right)}\right] & \text{through-plane direction} \\ 1 - 0.977\left(1-\epsilon\right)^{-0.009} \exp\left[0.344\left(1-\epsilon\right)\right]\left[\dfrac{3\epsilon}{3-\left(1-\epsilon\right)}\right] & \text{in-plane direction} \end{cases} \tag{8.4}$$

where this relation is valid for a porosity range $0.4 \leq \epsilon \leq 0.9$

- The through-plane and in-plane electrical conductivity of untreated, dry carbon paper GDL can be written in terms of the porosity as follows:

$$\frac{\kappa_{\text{eff}}}{\kappa_{\text{s}}} = \begin{cases} 1 - 0.962\left(1-\epsilon\right)^{-0.007} \exp\left[0.889\left(1-\epsilon\right)\right]\left[\dfrac{3\epsilon}{3-\left(1-\epsilon\right)}\right] & \text{through-plane direction} \\ 1 - 0.962\left(1-\epsilon\right)^{-0.016} \exp\left[0.367\left(1-\epsilon\right)\right]\left[\dfrac{3\epsilon}{3-\left(1-\epsilon\right)}\right] & \text{in-plane direction} \end{cases} \tag{8.5}$$

where this relation is valid for a porosity range $0.4 \leq \epsilon \leq 0.9$

- The relative permeability can be written using the Mualem-VG (MVG) model, the Burdine-BC (BBC) model and the power law in terms of the liquid water saturation as follows:

  - MVG model:

$$\kappa_{\text{rg}} = \left(1 - s_{\text{l}}\right)^{\eta_g}\left[1 - \left(1 - \left(1 - s_{\text{l}}\right)^{1/m}\right)^{m}\right]^2 \qquad \kappa_{\text{rl}} = \left(s_{\text{l}}\right)^{\eta_l}\left(1 - \left(1 - s_{\text{l}}\right)^{1/m}\right)^{2m} \tag{8.6}$$

    where $m = 0.8$, $\eta_g = 0.5$ and $\eta_l = 2$.

  - BBC model:

$$\kappa_{\text{rg}} = \left(1 - s_{\text{l}}\right)^{3+2/\lambda} \qquad \kappa_{\text{rl}} = s_{\text{l}}^2\left(1 - \left(1 - s_{\text{l}}\right)^{1+2/\lambda}\right) \tag{8.7}$$

where $\lambda = 3$.

– Power law:

$$\kappa_{\mathrm{rl}} = s_{\mathrm{l}}^{n} \qquad \kappa_{\mathrm{rg}} = (1 - s_{\mathrm{l}})^{n} \tag{8.8}$$

where $n = 3.5$.

- The capillary pressure can be written using the VG and BC models in terms of the wetting phase saturation as follows:

  – van Genuchten (VG) model:

$$s_{\mathrm{wp}} = \left(1 + \left(\frac{P_c}{0.0856}\right)^{5}\right)^{-0.8} \tag{8.9}$$

  – Brooks-Corey (BC) model:

$$s_{\mathrm{wp}} = \left(\frac{P_c}{0.075}\right)^{-3} \tag{8.10}$$

8.2 Future Work

In this thesis, numerical and experimental techniques were utilized in order to obtain a comprehensive set of theoretical and empirical expressions of the transport coefficients of the carbon paper GDL of PEM fuel cells. The research presented in this thesis can be extended to further understand the transport coefficients of the GDL and to other components of the cell, specifically the catalyst layer. The future work for this research area can be summarized as follows:

- Given the manufacturing method of the carbon paper GDL, the contact angle of the layer can vary throughout its thickness. Hence, it would be interesting to investigate the change of hydrophobicity on liquid water distribution and the effective properties of the wet GDL.

- As seen in this thesis, the compression pressure has a significant effect on the overall thermal resistance between the carbon fibers. It is worth while to further investigate the effect of pressure hysteresis. The thermal resistance due to loading and unloading of the cell can have a significant effect on the overall thermal durability of the GDL.

- Similarly to the pressure hysteresis, the temperature hysteresis should also be investigated. The effect of cooling the cell on the thermal conductivity should be measured.

- Due to the dependence of the effective properties on the manufacturing process, the method of Teflon coating on the transport coefficients should be examined.
- Finally, the methods utilized in this thesis to investigate the properties of the GDL can be extended to estimate the properties of the catalyst layer and the electrolyte membrane. Using the results of this thesis and the recommended future work, a handbook of properties of the components of the cell should be put together.

References

[1] N. Zamel, X. Li. Life cycle analysis of vehicles power by a fuel cell and by internal combustion engine for Canada. *Journal of Power Sources*. 2006; **155**:297-310.

[2] N. Zamel, X. Li. Life cycle comparison of fuel cell vehicles and internal combustion engine vehicles for Canada and the United States. *Journal of Power Sources*. 2006; **162**:1241-1253.

[3] N. Zamel, X. Li. Transient analysis of carbon monoxide poisoning and oxygen bleeding in a PEM fuel cell anode catalyst layer. *International Journal of Hydrogen Energy*. 2008; **33**:1335-1344.

[4] N. Zamel, X. Li. Effects of contaminants on polymer electrolyte membrane fuel cells. *Progress in Energy and Combustion Science*. 2010; doi:10.1016/j.pecs.2010.06.003.

[5] N. Zamel, X. Li. Chapter 7: Anode contamination modeling. In PEM Fuel Cell Contamination, Eds: J. Zhang, H. Li and Z. Shi, Taylor and Francis Group, 2009.

[6] H. Wu. Mathematical modeling of transient transport phenomena in PEM fuel cells. Ph.D. Thesis, University of Waterloo, Waterloo, Ontario, 2010.

[7] A. Damjanovic, V. Brusic. Electrode kinetics of oxygen reduction on oxide free platinum electrodes. *Electrochimica Acta*. 1967; **12**:615-28.

[8] A. Damjanovic, M.A. Genshaw. Dependence of the kinetics of oxygen dissolution at Pt on the conditions for adsorption of reaction. *Electrochimica Acta*. 1970; **15**:1281-1283.

[9] D.B. Sepa, M.V. Vojnovic, L.M¿ Vracar, A. Damjanovic. Different views regarding the kinetics and mechanisms of oxygen reduction at Pt and Pd electrodes. *Electrochimica Acta*. 1987; **32**:129-134.

[10] J.K. Norskøv, J. Rossmeisl, A. Logadottir, L. Lindqvist, J.R. Kitchin, T. Bilgaard, H. Jonsson. Origin of the overpotential for oxygen reduction at a fuel cell cathode. *Journal of Physical Chemistry B*. 2004; **108**:17886-17892.

[11] G.S. Karlberg, J. Rossmeisl, J.K. Norskov. Estimations of electric field effects on the oxygen reduction reaction based on the density functional theory. *Physical Chemistry Chemical Physics*. 2007; **9**:5158-5161.

[12] J. Tafel. Polarization with cathodic hydrogen liberation. *Zeitschrift fur Physikalische Chemie*. 1905; **50**:641-712.

[13] T. Erdey-Grúz, M. Volmer. Theory of hydrogen overpotential. *Zeitschrift fur Physikalische Chemie*. 1930; **150**:203-213.

[14] J. Heyrovsky. *Recl. Trav. Chim. Pays-Bas*. 1927; **46**:582.

[15] K. Jiao, X. Li. Water transport in polymer electrolyte membrane fuel cells. *Progress in Energy and Combustion Science*. 2011; **37**:221-291.

[16] Y. Wang, C.Y. Wang, K.S. Chen, Elucidating differences between carbon paper and carbon cloth in polymer electrolyte fuel cells, *Electrochimica Acta*, 2007; **52**:3965-3975.

[17] M. Mathias, J. Roth, J. Fleming, W. Lehnert. Diffusion media materials and characterization, Handbook of Fuel Cells-Fundamentals, Technology and Applications. *John Wiley and Sons*. 2003; **vol. 3**.

[18] K. Jiao, X. Li. Three-dimensional multiphase modeling of cold start processes in polymer electrolyte membrane fuel cells. *Electrochimica Acta*. 2009; **54**:6876-6891.

[19] D.M. Bernardi and M.W. Verbrugge. Mathematical model of a gas diffusion electrode bonded to a polymer electrolyte. *Journal of the Electrochemical Society*. 1991; **37**.

[20] D.M. Bernardi and M.W. Verbrugge. A mathematical model of the solid-polymer-electrolyte fuel cell. *Journal of the Electrochemical Society*. 1992; **139**.

[21] T.E. Springer, T.A. Zawodinski, S. Gottesfeld. Polymer electrolyte fuel cell model. *Journal of Electrochemical Society*. 1991; **138**.

[22] T.E. Springer, M.S. Wilson, S. Gottesfeld. Modeling and experimental diagnostics in polymer electrolyte fuel cells. *Journal of Electrochemical Society*. 1993; **140**.

[23] J.J. Baschuk, X. Li. A comprehensive, consistent and systematic mathematical model of PEM fuel cells. *Applied Energy*. 2009; **86**:181-193.

[24] H. Wu, X. Li, P. Berg. On the modeling of water transport in polymer electrolyte membrane fuel cells. *Electrochimica Acta*. 2009; **54**:6913-6927.

[25] H. Wu, P. Berg, X. Li. Modeling of PEMFC transients with finite-rate phase-transfer processes. *Electrochemical Society*. 2010; **157**:B1-B12.

[26] K. Jiao, X. Li. A three-dimensional non-isothermal model of high temperature proton exchange membrane fuel cells with phosphoric acid doped polybenzimidazole membranes. *Fuel Cells*. 2010; **10**:351-362.

[27] J.J. Baschuk, X. Li. Modelling carbon monoxide poisoning and oxygen bleeding in a PEM fuel cell anode. *International Journal of Energy Research*. 2003; **27**:1095-1116.

[28] K. Vafai and C. Tien. Boundary and inertia effects on flow and heat transfer in porous media. *Journal of Heat and Mass Transfer*. 1981; **24**.

[29] C. Wang. Multiphase flow and heat transfer in porous media. *Advances in Heat Transfer*. 1997; **196**.

[30] E. Buckingham. Contribution to our knowledge of the aeration of soils. *Bull. Div. Soils US. Dep. Agriculture*. 1904; **25**.

[31] H.L. Penman. Gas and vapor movements in the foil-I. *Journal of Agriculture Science*. 1940; **30**:437-462.

[32] H.L. Penman. Gas and vapor movements in the foil-II. *Journal of Agriculture Science*. 1940; **30**:570-581.

[33] C.H.M. van Bavel. Gaseous diffusion and porosity in porous media. *Soil Science*, 1952; **73**:91-104.

[34] J.A. Currie. Gaseous diffusion in porous media part 1: A non-steady state method. *Journal of Applied Physics*. 1960; **11**:314-317.

[35] J.A. Currie. Gaseous diffusion in porous media part 2: dry granular materials. *Journal of Applied Physics*. 1960; **11**:318-324.

[36] D.A.G. Bruggeman. Calculation of various physics constants in heterogenous substances I Dielectricity constants and conductivity of mixed bodies from isotropic substances. *Annalen der Physik (Leipzig)*. 1935; **24**:636-664.

[37] T.J. Marshall. Permeability and size distribution of pore. *Nature (Lond.)*. 1957; **180**:664-665.

[38] R.J. Millington. Gas diffusion in porous media. *Science (N.Y.)*. 1959; **130**:100-102.

[39] H.L. Weissberg. Effective diffusion coefficient in porous media. *Journal of Applied Physics*. 1963; **34**:2636-2639.

[40] G.H. Neale and W.K. Nader. Prediction of transport processes within porous media: Diffusive flow processes within a homogeneous swarm of spherical particles. *AIChE Journal*. 1973; **19**:112-119.

[41] J. Schwarzbach. Diffusion in porous materials partially wetted with a binary mixture. *Chemical Engineering and Processing*. 1989; **26**:3544.

[42] M.M. Tomadakis and S.V. Sotirchos. Ordinary and transition regime diffusion in random fiber structures. *AIChE Journal*. 1993; **39**:397-412.

[43] M. Aubertin, M. Aachib, K. Authier. Evaluation of diffusive gas flux through covers with a GCL, *Geotextiles and Geomembranes*. 2000; **18**:215-233.

[44] J. Whitcomb, X. Tang. Micromechanics of moisture diffusion in composites with impermeable fibers, *Journal of Composite Materials*. 2002; **36**:1093-1101.

[45] S. Li, L.J. Lee, J. Castro. Effective mass diffusivity in composites. *Journal of Composite Materials*. 2002; **36**:1709-1724.

[46] M.M. Mezedur, M. Kaviany, W. Moore. Effect of pore structure, randomness sand size on effective mass diffusivity. *AIChE Journal*. 2002; **48**:15-24.

[47] J.H. Nam and M. Kaviany. Effective diffusivity and water-saturation distribution in single and two-layer PEMFC diffusion medium. *International Journal of Heat and Mass Transfer*. 2003; **46**:4595-4611.

[48] P.K. Das, X. Li, Z.S. Liu. Effective transport coefficients in PEM fuel cell catalyst and gas diffusion layers: Beyond Bruggeman approximation. *Applied Energy*. doi: 10.1016/j.apenergy.2009.05.006.

[49] Hashin Z., Shtrikman S.A. A variational approach to the theory of the effective magnetic permeability of multi-phase materials. *Journal of Applied Physics*. 1962; **33**:3125-3131.

[50] G.W. Milton. The theory of composites. New York: Cambridge University Press, 2002.

[51] J.T. Gostick, M.A. Ioannidis, M.W. Fowler, M.D. Pritzker. Pore network modeling of fibrous gas diffusion layers for polymer electrolyte membrane fuel cells. *Journal of Power Sources*. 2007; **173**:277-290.

[52] D. Baker, C. Wieser, K.C. Neyerlin, M.W. Murphy. The use of limiting current to determine transport resistance in PEM fuel cells. *ECS Transactions*. 2006; **3**:989-999.

[53] D. Kramer, S.A. Freunberger, R. Flückiger, I.A. Schneider, A. Wokaun, F.N. Büchi, G.G. Scherer. Electrochemical diffusimetry of fuel cell gas diffusion layers. *Journal of Electroanalytical Chemistry*. 2008; **612**:63-77.

[54] R. Flückiger, S.A. Freunberger, D. Kramer, A. Wokaun, G.G. Scherer, F.N. Büchi. Anisotropic, Effective Diffusivity of Porous Gas Diffusion Layer Materials for PEFC. *Electrochimica Acta*. 2008; **54**:551-559.

[55] V.P. Schulz, J. Becker, A. Wiegmann, P.P. Mukherjee, C.Y. Wang. Modeling of two-phase behavior in the gas diffusion medium of PEFCs via full morphology approach. *Journal of the Electrochemical Society*. 2007; **154**:B419-B426.

[56] K. Schladitz, S. Peters, D. Reinel-Bitzer, A. Wiegmann, J. Ohser. Design of acoustic trim based on geometric modeling and flow simulation for non-woven. *Comput Mater Sci*. 2006; **38**:56-66.

[57] P.K. Sinha, P.P. Mukherjee, C.Y. Wang. Impact of GDL structure and wettability on water management in polymer electrolyte fuel cells. *J Mater Chem*. 2007; **17**:3089-3103.

[58] V.P. Schulz, P.P. Mukherjee, J. Becker, A. Wiegmann, C.Y. Wang. Numerical evaluation of effective gas diffusivity saturation dependence of uncompressed and compressed gas diffusion media in PEFCs. *ECS Trans*. 2006; **3**:1069-1075.

[59] P.P. Mukherjee, C.Y. Wang. Polymer electrolyte fuel cell modeling - a Pore scale perspective. In: Progress in Green Energy, X. Li (eds), New York:Springer, 2009:185-228.

[60] S.G. Kandlikar, Z. Lu. Thermal management issues in PEMFC stack - A brief review of current status. *Applied Thermal Engineering*. 2009; **29**:1276-1280.

[61] N. Djilali, D.M. Lu. Influence of heat transfer on gas and water transport in fuel cells. *International Journal of Thermal Science*. 2002; **41**:29-40.

[62] Y. Shan, S.Y. Choe. A high dynamic PEM fuel cell model with temperature effects. *Journal of Power Sources*. 2005; **145**:30-39.

[63] J.J. Hwang. Thermal-electrochemical modeling of a proton exchange membrane fuel cell. *Journal of the Electrochemical Society*. 2006; **153**:A216-A224.

[64] N. Zamel, X. Li. Non-isothermal, multi-phase modeling of PEM fuel cell cathode. *International Journal of Energy Research*. 2009; DOI: 10.1002/er.1572.

[65] J. Ramousse, S. Didierjean, O. Lottin, D. Maillet. Estimation of the effective thermal conductivity of carbon felts used as PEMFC gas diffusion layers. *International Journal of Thermal Sciences*. 2008; **47**:1-6.

[66] M. Khandelwal, M.M. Mench. Direct measurement of through-plane thermal conductivity and contact resistance in fuel cell materials. *Journal of Power Sources*. 2006; **161**:1106-1115.

[67] P.J.S. Vie, S. Kjelstrup. Thermal conductivities from temperature profiles in the polymer electrolyte fuel cell. *Electrochimica Acta*. 2004; **49**:1069-1077.

[68] I. Nitta, O. Himanen, M. Mikkola. Thermal conductivity and contact resistance of compressed gas diffusion layer of PEM fuel cell. *Fuel Cells*. 2008; **2**:111-119.

[69] O. Burheim, P.J.S. Vie, J.G. Pharoah, S. Kjelstrup. Ex situ measurements of through-plane thermal conductivities in a polymer electrolyte fuel cell. *Journal of Power Sources*. 2010; **195**:249-256.

[70] G. Karimi, X. Li, P. Teerstra. Measurement of through-plane effective thermal conductivity and contact resistance in PEM fuel cell diffusion media. *Electrochimica Acta*. Submitted in August 2009.

[71] E. Sadeghi, N. Djilali, M. Bahrami. Effective thermal conductivity and thermal contact resistance of gas diffusion layers in proton exchange membrane fuel cells. Part 1: Effect of compressive load. *Journal of Power Sources*. 2010; doi:10.1016/j.jpowsour.2010.06.039

[72] E. Sadeghi, N. Djilali, M. Bahrami. Effective thermal conductivity and thermal contact resistance of gas diffusion layers in proton exchange membrane fuel cells. Part 2: Hysteresis effect under cyclic compressive load. *Journal of Power Sources*. 2010; In Press.

[73] P. Teerstra, G. Karimi, X. Li. Measurement of in-plane effective thermal conductivity in PEM fuel cell diffusion media. *Electrochimica Acta*. 2010; doi:10.1016/j.electacta.2010.06.043.

[74] E. Sadeghi, M. Bahrami, N. Djilali. Analytic determination of the effective thermal conductivity of PEM fuel cell gas diffusion layers. *Journal of Power Sources*. 2008; **179**:200-208.

[75] D. Veyret, G. Tsotridis. Numerical determination of the effective thermal conductivity of fibrous materials: Application to proton exchange membrane fuel cell gas diffusion layers. *Journal of Power Sources*. 2010; **195**:1302-1307.

[76] G. Maggio, V. Recupero, C. Mantegazza. Modelling of temperature distribution in a solid polymer electrode cell stack. *Journal of Power Sources*. 1996; **62**:167-174.

[77] M. Wohr, K. Bolwin, W. Schnurnberger, M. Fischer, W. Neubrand, G. Eigenberger. Dynamic modelling and simulation of a plymer membrane fuel cell including mass transport limitations. *International Journal of Hydrogen Energy*. 1998; **23**:213-218.

[78] P. Argyropoulos, K. Scott, W.M. Taama. One-dimensional thermal model for direct methanol fuel cell stacks: Part I. Model development. *Journal of Power Sources*. 1999; **79**:169-183.

[79] J.J. Baschuk, X. Li. A general formulation for a mathematical PEM fuel cell model. *Journal of Power Sources*. 2005; **142**:134-153.

[80] H. Wu, P. Berg, X. Li. Non-isothermal transient modeling of water transport in PEM fuel cells. *Journal of Power Sources*. 2007; **165**:232-243.

[81] J.G. Pharoah, K. Karan, W. Sun. On effective transport coefficients in PEM fuel cell electrodes: anisotropy of the porous transport layer. *Journal of Power Sources*. 2006; **161**:214-224.

[82] H.T. Aichlmayr, F.A. Kulacki. The effective thermal conductivity of saturated porous media. In: Greene G., editor. Advances in heat transfer. *New York: Academic Press*. 2006; **39**:377-460.

[83] W. Woodside, J. Messmer. Thermal conductivity of porous media. I. Unconsolidated sands. *Journal of Applied Physics*. 1961; **32**:1688-1699.

[84] W. Woodside, J. Messmer. Thermal conductivity of porous media. II. Consolidated rocks. *Journal of Applied Physics*. 1961; **32**:1699-1706.

[85] O. Wiener. Die theorie des mischkörpers fr das feld der stationren strömung. *Abh. Math. Phys. Kl. Sächs. Akad. Wiss. (Leipzig)*. 1912; **32**:507-604.

[86] D.E. Aspnes. Local-field effects and effective-medium theory - A microscopic perspective. *American Journal of Physics*. 1982; **50**:704-709.

[87] M. Kaviany. Principles of Heat Transfer in Porous Media, second edition. *Springer, New York*. 1995.

[88] Z. Abdulagatova, I.M. Abdulagatov, V.N. Emirov. Effect of temperature and pressure on the thermal conductivity of sandstone. *International Journal of Rock Mechanics and Mining Sciences*. 2009; **46**:1055-1071.

[89] M.V. Williams, E. Begg, L. Bonville, R. Hunz, J.M. Fentona. Characterization of gas diffusion layers for PEMFC. *Journal of the Electrochemical Society*. 2004; **151**:A1173-A1180.

[90] I. Nitta, T. Hottinen, O. Himanena, M. Mikkola. Inhomogeneous compression of PEMFC gas diffusion layer: Part I. Experimental. *Journal of Power Sources*. 2007; **172**:26-36.

[91] Material specifications of TORAY carbon fiber - http://www.fuelcell.com/techsheets/TORAY-TGP-H.pdf

[92] Manufacturers Data Sheet for SIGRACET GDL 10 series by SGL Carbon - http://www.servovision.com/fuel_cell_components/gdl_10.pdf

[93] T. Tomimura, S. Nakamura, H. Nonami, H. Saito. Resistivity of elastic separator used in PEFC and evaluation of contact resistance between separator and electrode sheet. *Proceedings for: 2001 IEEE 7th International Conference on Solid Dielectrics*. June 25-29, 2001; 101-104.

[94] D. Natarajan, T.V. Nguyen. Effect of electrode configuration and electronic conductivity on current density distribution measurements in PEM fuel cells. *Journal of Power Sources*. 2004; **135**:95-109.

[95] C. Lee, W. Mérida. Gas diffusion layer durability under steady-state and freezing conditions. *Journal of Power Sources*. 2007; **164**:141-153.

[96] H. Looyenga. Dielectric constants of heterogeneous mixtures. *Physica*. 1965; **31**:401406.

[97] C.J.F Böttcher, Theory of Electric Polarization, Elsevier, Amsterdam, 1952.

[98] Y. Shi, J. Xiao, M. Pana, R. Yuan. A fractal permeability model for the gas diffusion layer of PEM fuel cells. *Journal of Power Sources*. 2006; **160**:277-283.

[99] J.P. Feser, A.K. Prasad, S.G. Advani. Exeperimental characterization of in-plane permeability of gas diffusion layers. *Journal of Power Sources*. 2006; **162**:1226-1231.

[100] J.T. Gostick, M.W. Fowler, M.D. Pritzker, M.A. Ioannidis, L.M. Behra. In-plane and through-plane gas permeability of carbon fiber electrode backing layers. *Journal of Power Sources*. 2006; **162**:228-238.

[101] M.M. Tomadakis, T.J. Robertson. Viscous permeability of random fiber structures: Comparison of electrical and diffusional estimates with experimental and analytical results. *Journal of Composite Materials*. 2005; **39**:163-188.

[102] L. Hao, P. Cheng. Lattice boltzmann simulations of anisotropic permeabilities in carbon paper gas diffusion layers. *Journal of Power Sources*. 2009; **186**:104-114.

[103] B. Yu, J. Li. Some fractal characters of porous media. *Fractals*. 2001; **9**:365-372.

[104] J. Chen, J. Hopmans, M. Grismer. Parameter estimation of two-fluid capillary pressure saturation and permeability functions. *Advances in Water Resources*. 1999; **22**:479-493.

[105] N.T. Burdine. Relative permeability calculations from pore size distribution data. *Petroleum Trans. Am. Inst. Mining Eng.* 1953; **198**:71-77.

[106] Y. Mualem. A new model for predicting the hydraulic conductivity of unsaturated porous media. *Water Resources Research* 1976; **12**:513-522.

[107] M.T. van Genuchten. Closed-form equation for predicting the hydraulic conductivity of unsaturated soils. *American Journal of Soil Science Society*. 1980; **44**:892-898.

[108] J. Bear. Dynamics of Fluids in Porous Media. *Dover Publications*, New York. 1972.

[109] A. Adamson. Physical chemistry of surfaces. *Wiley, New York*, 5th edition. 1990.

[110] M. C. Leverett. Capillary behavior in porous solids. *Transactions of AIME*. 1941; **142**:152-169.

[111] K. S. Udell. Heat transfer in porous media considering phase change and capillarity: The heat pipe effect. *International Journal of Heat and Mass Transfer*. 1985; **28**:485-495.

[112] M.A. Ioannidis, I. Chatzis. Network modelling of pore structure and transport properties of porous media. *Chemical Engineering Science*. 1993; **48**:951-972.

[113] T.V. Nguyen, G. Lin, H. Ohn, X. Wang. Measurements of two-phase flow properties of the porous media used in PEM fuel cells. *ECS Transactions*. 2006; **3**:415-423.

[114] J.T. Gostick, M.W. Fowler, M.A. Ioannidis, M.D. Pritzker, Y.M. Volfkovich, A. Sakars. Capillary pressure and hydrophilic porosity in gas diffusion layers of polymer electrolyte fuel cells. *Journal of Power Sources*. 2006; **156**:375-387.

[115] E.C. Kumbur, K.V. Sharp, M.M. Mench. Validated Leverett approach for multiphase flow in PEFC diffusion media. I. Hydrophobicity effect. *Journal of the Electrochemical Society*. 2007; **154**:B1295-B1304.

[116] E.C. Kumbur, K.V. Sharp, M.M. Mench. Validated Leverett approach for multiphase flow in PEFC diffusion media. II. Compression effect. *Journal of the Electrochemical Society*. 2007; **154**:B1305-B1314.

[117] E.C. Kumbur, K.V. Sharp, M.M. Mench. Validated Leverett approach for multiphase flow in PEFC diffusion media. III. Temperature effect and unified approach. *Journal of the Electrochemical Society*. 2007; **154**:B1315-B1324.

[118] J.T. Gostick, M.A. Ioannidis, M.W. Fowler, M.D. Pritzker. Wettability and capillary behavior of fibrous gas diffusion media for polymer electrolyte membrane fuel cells. *Journal of Power Sources*. 2009; **194**:433-444.

[119] J.D. Fairweather, P. Cheung, D.T. Shwartz. The effects of wetproofing on the capillary properties of proton exchange membrane fuel cell gas diffusion layers. *Journal of Power Sources*. 2010; **195**:787-793.

[120] Q. Ye, T.V. Nguyen. Three-dimensional simulation of liquid water distribution in a PEMFC with experimentally measured capillary pressure. *Journal of The Electrochemical Society*. 2007; **154**:B1242-B1251.

[121] D. Natarajan and T. V. Nguyen. A two-dimensional, two-phase, multicomponent, transient model for the cathode of a proton exchange membrane fuel cell using conventional gas distributors. *Journal of the Electrochemical Society*. 2001; **148**:A1324-A1335.

[122] H. Wu, X. Li, P. Berg. On the modeling of water transport in polymer electrolyte membrane fuel cells. *Electrochimica Acta*. 2009; **54**:6913-6927.

[123] Y.M. Volfkovich, V.S. Bagotzky VS. The method of standard porosimetry. 1: Principles and possibilities. *Journal of Power Sources*. 1994; **48**:327-338.

[124] Y.M. Volfkovich, V.S. Bagotzky. The method of standard porosimetry. 2: Investigation of the formation of porous structures. *Journal of Power Sources*. 1994; **48**:339-348.

[125] Y.M. Volfkovich, V.S. Bagotzky, V.E. Sosenkin, I.A. Blinov. The standard contact porosimetry. *Colloids and Surfaces A: Physicochemical and Engineering Aspects*. 2001; **187-188**:349-365.

[126] J.H. Rohling, J. Shen, J. Zhou, C.E. Gu. Application of the diffraction theory for photothermal deflection to the measurement of the temperature coefficient of the refractive index of a binary gas mixture. *Journal of Applied Physics*. 2006; **99**:103-107.

[127] J.H. Rohling, J. Shen, C. Wang, J. Zhou, C.E. Gu. Determination of binary diffusion coefficients of gases using photothermal deflection technique. *Applied Physics B*. 2007; **87**:355-362.

[128] J. Crank. The Mathematics of Diffusion, 2nd edition. *Oxford University Press, New York*. 1975.

[129] L. Mao, C.-Y. Wang, Y. Tabuchi. A multiphase model for cold start of polymer electrolyte fuel cells. *Journal of the Electrochemical Society*. 2007; **154**:B341-B351.

[130] F. Jiang, W. Fang, C.-Y. Wang. Non-isothermal cold start of polymer electrolyte fuel cells. *Electrochimica Acta*. 2007; 53:610-621.

[131] K. Jiao, X. Li. Effects of various operating and initial conditions on cold start performance of polymer electrolyte membrane fuel cells. *International Journal of Hydrogen Energy*. 2009; **34**:8171-8184.

[132] K. Jiao, X. Li. Cold start analysis of polymer electrolyte membrane fuel cells. *International Journal of Hydrogen Energy*. 2010; **35**:5077-5094.

[133] G. M. Volohov and A.S. Kasperovich. Monotonic heating regime methods for the measuremnt of thermal diffusivity, in: Compendum of thermophysical property measurement methods: Recommended measurement techniques and practices, (Eds) K.D. Maglic, A. Cezairliyan, V.E. Peletsky. *New York and London: Plenum Press*. 1989; **Volume 1**:429-454.

[134] E. S. Platunov. Instruments for measuring thermal conductivity, thermal diffusivity, and specific heat under monotonic heating, in: Compendum of thermophysical property measurement methods: Recommended measurement techniques and practices, (Eds) K.D. Maglic, A. Cezairliyan, V.E. Peletsky. *New York and London: Plenum Press*. 1989; **Volume 2**:347-374.

[135] E. Litovsky, N. Puchkelevitch. Thermophysical Properties of Refractory Materials. *Reference Book, Metallurgy, Moscow*. 1982.

[136] J. Blumm, A. Lindemann, M. Meyer, C. Strauser. Characterization of PTFE using advanced thermal analyses technique. http://www.netzsch-thermal-analysis.com/download/P-022_315.pdf. NETZCH. 2010.

[137] ITL-070606-6243 Report. Thermal physical properties of compressed fiber insulation in the temeprature range 200-950 deg C. December 2006.

[138] E. Litovsky, V. Issoupov, J. Kleiman, R. Latham, A. Kotrba, K. Olivier. Thermal conductivity of mechanically compressed fiber insulation materials in a wide temperature range: New test method and experimental results. *International Thermal Conductivity Conference*. 2007; ITCC 29/ITES 17 conferences, Alabama, June 24-27.

[139] E. Litovsky, T. Litovsky, M. Shapiro, A. Shavit. Thermal conductivity dependence of MgO heat insulations on porosity in temperature range 500-2000K. *Third Symposium on Insulation Materials: Testing and Applications, ASTM, STP 13-20*. 1997; May 15-17, Quebec, Canada, 292-306.

[140] Committee E37 on Thermal Measurements, Subcommittee E37.05 on Thermophysical Properties. NIST USA Research Report, Interlaboratory Study to Establish Precision Statements for ASTM E2584, June, 2009.

[141] E. Litovsky, J. Kleiman, N. Menn N. Measurement and analysis by different methods of apparent, radiative and conductive thermophysical properties of materials. *Journal of the High Temperatures-High Pressures*. 2003/200; **35-36**:101-108.

[142] E. Litovsky, J. Kleiman, N. Menn. Measurement of thermal physical and optical properties of semitransparent materials in the temperature range 20-1800 deg C. *26th International Thermal Conductivity Conference*. 2005; MA, USA, DESTECH PUBL, INC., 167-179.

[143] E. Litovsky, J. Kleiman, R. Simmat, J. Pötschke. Thermal physical properties of ceramics, glasses and insulation materials in the range 200-1800 deg C: Problems and experimental results. *Proceeding of the 1st International Congress on Ceramics: A Global Roadmap*. 2005; Editor Stephen Freiman, WILEY, The American Ceramic Society, Toronto, ON, 25-29 June.

[144] J. Pötschke, R. Simmat, E. Litovsky, J. Kleiman. A method to determine the thermal conductivity in the range of 200-1600 deg C. *49th International Colloquium on Refractories*. 2006; Aachen:14-20.

[145] J.R. Taylor. An Introduction to Error Analysis: The Study of Uncertainties in Physical Measurements, Second Edition. *University Science Books, Sausalito, US*. 1997, Chapter 3.

[146] E. Litovsky, J. Kleiman, N. Menn. Thermal physical and optical properties of the fiber insulation materials in the temperature range 200-1800 deg C: Insulation Materials: Testing and Applications fourth Volume ASTM STP 1426, Eds: A.O. Desjarlais, R.R. Zarr. *American Society for Testing Materials, ASTM International, West Conshohocken, PA*. 2002; pp. 257-269.

[147] ASTM - Designation: E2584-07. Standard practice for thermal conductivity of materials using a thermal capacitance (Slug) Calorimeter. This practice is under the jurisdiction of ASTM Committee E37.

[148] E.N. Fuller, P.D. Schettler, J.C. Giddings. New method for prediction of binary gas phase diffusion coefficients. *Industrial and Engineering Chemistry*. 1996; **58**:19-27.

[149] J. Stumper, H. Haas, A. Granados. In situ determination of MEA resistance and electrode diffusivity of a fuel cell. *Journal of the Electrochemical Society*. 2005; **152**:A837-A844.

[150] N.G.C. Astrath, J. Shen, D. Song, J.H. Rohling, F.B.G. Astrath, J. Zhou, T. Navessin, Z.S. Liu, C.E. Gu, X. Zhao. The effect of relative humidity on the binary gas diffusion. *Journal of Physical Chemistry B*. 2009; **A113**:8369-8374.

[151] W.G. Pollard, R.D. Present. On gaseous self-diffusion in long capillary tubes. *Physical Review*. 1948; **73**:762-774.

[152] S. Jaganathan, H.V. Tafreshi, B. Pourdeyhimi. A case study of realistic two-scale modeling of water permeability in fibrous media. *Separation Science and Technology*. 2008; **43**:1901-1916.

[153] Fraunhofer ITWM, Department Flow and Complex Structures. Geodict. Available from: http://www.geodict.com, 2005.

[154] J. Bear. Dynamics of fluids in porous media. *Dover, New York*. 1988.

[155] P. Corbett, S. Anggraeni, D. Bowen. The use of the probe permeameter in carbonates - addressing the problems of permeability support and stationarity. *The Log Analyst*. 1999; **40**:316-326.

[156] J.L. Jensen, L.W. Lake, P.W.M. Corbett, D.J. Goggin. Statistics for petroleum engineers and geoscientists, 2nd edn. *Elsevier, Amsterdam*. 2000.

[157] K. Nordahl, P.S. Ringrose. Identifying the representative elementary volume for permeability in heterolithic deposits using numerical rock models. *Math Geoscience*. 2008; **40**:753-771.

[158] P.W.M. Corbette, J.L. Jensen. Estimating the mean permeability: how many measurements do we need? *First Break*. 1992; **10**:89-94.

[159] J. Benziger, J. Nehlsen, D. Blackwell, T. Brennan, J. Itescu. Water flow in the gas diffusion layer of PEM fuel cells. *Journal of Membrane Science*. 2005; **261**:98-106.

[160] U. Hornung. Homogenization and porous media. *Springer*, New York. 1997.

[161] A. Wiegmann and A. Zemitis. EJ-HEAT: A Fast Explicit Jump harmonic averaging solver for the effective heat conductivity of composite materials. Technical Report 94, Fraunhofer ITWM Kaiserslautern. 2006.

[162] A. Wiegmann and A. Zemitis. EJ-DIFFUSION: A Fast Explicit Jump harmonic averaging solver for the effective diffusivity of porous materials. Fraunhofer ITWM Kaiserslautern. 2007.

[163] N. Zamel, E. Litovsky, S. Shakhshir, X. Li, J. Kleiman. Measurment of in-plane thermal conductivity of carbon paper diffusion media in the temperature range of -20 to +120 deg C. *Applied Energy*. 2011:doi:10.1016/j.apenergy.2011.02.037

[164] N. Zamel, N.G.C. Astrath, X. Li, J. Shen, J. Zhou, F.B.G. Astrath, H. Wang and Z.-S. Liu. Experimental determination of effective diffusion coefficient of Oxygen-Nitrogen mixture in carbon paper. *Chemical Engineering Science*. 2010; **65**:931-937.

[165] R.A. Buerschaper. Thermal and electrical conductivity of graphite and carbon at low temperatures. *Journal of Applied Physics*. 1944; **15**:452-454.

[166] R.W. Powell, F.H. Schofield. The thermal and electrical conductivities of carbon and graphite to high temperatures. *Proceedings of the Physical Society*. 1939; **51**:153-172.

[167] http://www.carbonandgraphite.org/pdf/the_element_c.pdf

[168] V. Villani. A Study on the Thermal Behavior and Structual Characteristics of Polytetrafluoraethylene. *Thermochim. Acta*. 1990; **162**:189-193.

[169] N. Zamel, X. Li, J. Shen, J. Becker and A. Wiegmann. Estimating effective thermal conductivity in carbon paper diffusion media. *Chemical Engineering Science*. 2010; **65**:3994-4006.

[170] N. Zamel, X. Li and J. Shen. Correlation for the effective gas diffusion coefficient in carbon paper. *Energy and Fuels*. 2009; **23**:6070-6078.

[171] N. Zamel, X. Li, J. Becker, A. Wiegmann. Effect of liquid water on transport properties of the gas diffusion layer of polymer electrolyte membrane fuel cells. *International Journal of Hydrogen Energy*. 2011:doi:10.1016/j.ijhydene.2011.01.146

[172] J.P. Owejan, T.A. Trabold, D.L. Jacobson, D.R. Baker, D.S. Hussey, M. Arif. In situ investigation of water transport in an operating PEM fuel cell using neutron radiography: Part 2 - Transient water accumulation in an interdigitated cathode flow field. *International Journal of Heat and Mass Transfer*. 2006; **49**:4721-4731.

[173] T. Koido, T. Furusawa, K. Moriyama. An approach to modeling two-phase transport in the gas diffusion layer of a proton exchange membrane fuel cell. *Journal of Power Sources*. 2008; **175**:127-136.

[174] E. Litovsky, M. Shapiro, A. Shavit. Gas pressure and temperature dependences of thermal conductivity of porous ceramic materials: Part 1, Refractories and Ceramics with Porosity below 30%. *Journal of the American Ceramic Society*. 1992; **75**:3425-3439.

[175] E. Litovsky, T. Gambaryan-Roisman, M. Shapiro, A. Shavit. Heat Transfer Mechanisms Governing Thermal Conductivity of Porous Ceramic Materials. *Trends in Heat, Mass & Momentum Transfer, Research Trends*. 1997; **3**:147-167.

[176] N. Zamel, X. Li. A parametric study of multi-phase and multi-species transport in the cathode of PEM fuel cells. *International Journal of Energy Research*. 2007; **32**:698-721.